THE EFFECT OF FIBRE LENGTH ON PASSAGE THROUGH NARROW APERTURES

By

James Allen Olson

B. Sc. (Physics) University of British Columbia, 1989

B. A. Sc. (Engineering Physics) University of British Columbia, 1991

A THESIS SUBMITTED IN PARTIAL FULFILLMENT OF

THE REQUIREMENTS FOR THE DEGREE OF

DOCTOR OF PHILOSOPHY

in

THE FACULTY OF GRADUATE STUDIES

CHEMICAL ENGINEERING

We accept this thesis as conforming

to the required standard

THE UNIVERSITY OF BRITISH COLUMBIA

August 1996

In presenting this thesis in partial fulfilment of the requirements for an advanced degree at the University of British Columbia, I agree that the Library shall make it freely available for reference and study. I further agree that permission for extensive copying of this thesis for scholarly purposes may be granted by the head of my department or by his or her representatives. It is understood that copying or publication of this thesis for financial gain shall not be allowed without my written permission.

James Allen Olson
Chemical Engineering
The University of British Columbia
2216 Main Mall
Vancouver, Canada
V6T 1Z4

Date: Aug. 20/1996

ABSTRACT

This thesis has examined the factors affecting the passage of fibres through narrow apertures under conditions similar to pulp pressure screening. This was accomplished by developing a theoretical model of fibre passage and verifying the predictions of this model experimentally.

The theoretical model was based on earlier observations of a "wall effect" and a "turning effect". These factors were represented in the model as a fibre concentration profile upstream of the aperture, and as the probability of a fibre at a given position entering the aperture. The near-wall, fibre concentration profile was experimentally determined for 1mm, 2mm and 3mm stiff fibres. Fibre concentration was found to increase linearly from zero at the wall to the average suspension concentration at a distance approximately 0.3 of a fibre length. It remained constant beyond this point.

For a given initial position and orientation of a fibre upstream of the slot, the probability of passage was modeled by theoretically determining the trajectories of individual fibres at the entry flow of the aperture, including impacts with the aperture wall. To a first order approximation, fibres passed through the aperture when their centres originated within the fluid layer that was drawn into the aperture. Using these theoretically calculated probabilities of passage with the experimentally measured fibre concentration profiles upstream of the aperture, passage ratios of fibres of different sizes were predicted. The predictions were compared to experimental measurements of passage ratio. The theoretical model was found to give good predictions of average passage ratio.

Table of Contents

ABSTRACT ii

List of Tables vii

List of Figures viii

Acknowledgment xiii

1 INTRODUCTION 1

2 LITERATURE REVIEW 4

2.1 Industrial Practice 4

2.2 Screening Studies 5

2.3 Hydrodynamic Studies of Suspended Particles 10

2.3.1 Low Reynolds Number Particle Hydrodynamics 10

2.3.2 Turbulent Particle Motion 13

2.3.3 Turbulent Particle Motion Near Walls 16

2.3.4 Turbulent Fibre Motion 17

2.4 Nomenclature 20

3 PROBLEM DEFINITION 21

3.1 Nomenclature 24

4 FIBRE MOTION IN TURBULENT FLOW 25

4.1 Introduction 25

4.2 Equations of Motion 26
4.2.1 The Equations of Mean Motion 28
4.2.2 The Equations of Turbulent Motion 29
4.3 Discussion 36
4.3.1 Mean Motion 36
4.3.2 Turbulent Motion 37
4.4 Summary 45
4.5 Nomenclature 46

5 THEORETICAL PREDICTIONS OF FIBRE PASSAGE 48

5.1 Introduction 48
5.2 Equations of Fibre Motion 49
5.2.1 Fibre Motion in a Free Flow 51
5.2.2 Fibre Motion During Contact With the Wall 52
5.3 Application of the Equations of Motion 57
5.3.1 Impact Types and Impact Switching 57
5.3.2 Stapling 58
5.3.3 Fluid Velocity Field 59
5.4 Results 63
5.4.1 $L/W = 0$ 64
5.4.2 $L/W = 0.5$ 64
5.4.3 $L/W = 1$ 66
5.4.4 $L/W = 2$ 68
5.4.5 $L/W = 3, 4$ 70
5.5 Discussion 75
5.6 Summary 77

5.7 Nomenclature 78

6 EXPERIMENTAL MEASUREMENT OF FIBRE CONCENTRATION 80

6.1 Introduction 80

6.2 Experimental Apparatus and Procedure 81

6.3 Results 84

6.3.1 Concentration Distribution of Fibres 85

6.3.2 Orientation Distribution of Fibres 86

6.3.3 Projected Fibre Length Distribution 87

6.4 Discussion 89

6.5 Summary 92

6.6 Nomenclature 94

7 PASSAGE RATIO: COMPARISON WITH EXPERIMENT 95

7.1 Introduction 95

7.2 Analysis 97

7.3 Comparison with Data in the Literature 99

7.3.1 Comparison with Kumar (1991) 99

7.3.2 Comparison with Gooding (1986) 102

7.3.3 Comparison with Tangsaghasaksri (1994) 105

7.4 Summary 106

7.5 Nomenclature 108

8 Summary and Conclusions 109

8.1 General 109

8.2 Specific Findings 110

8.2.1 Fibre Motion in Turbulent Flow 110
8.2.2 Theoretical Predictions of Fibre Passage 110
8.2.3 Experimental Measurement of Fibre Concentration 111
8.2.4 Passage Ratio: Prediction and Measurement 112
8.3 Conclusion 112

Bibliography **113**

A Jeffery's Equation of Fibre Motion **124**
A.1 Introduction 124
A.2 Equation of Motion 124
A.2.1 3-Dimensions 124
A.2.2 2-Dimensions 126
A.3 Analytical example 127

List of Tables

2.1 The following nomenclature was used in this section. 20

3.2 The following Nomenclature was used in this section. 24

4.3 The following nomenclature was used in this section. 46

5.4 The symbols used by the "fate plots" to represent the possible outcomes of the simulation. 64

5.5 The following nomenclature was used in this section. 79

6.6 The following nomenclature was used in this section. 94

7.7 The following nomenclature was used in this section. 108

List of Figures

1.1 Schematic of a typical industrial pulp screen. 2

2.2 A schematic of a single slot in a cross flow, a model pressure screen used to study fibre passage through narrow apertures. 6

2.3 Definition of passage ratio, $P = C_s/C_u$ 8

2.4 Passage ratio for several fibre length, L, to slot width, W, ratios as a function of slot velocity, V_s normalized by channel velocity, V_u (Kumar, 1991). The symbols are : L=1.0mm and W=1.0mm ($\diamond$), L=1.0mm and W=0.5mm (*), L=3.0mm and W=1.5mm ($\square$), L=3.0mm and W=1.0mm ($\triangle$), L=3.0mm and W=0.5mm ($\bullet$) 9

3.5 A fibre approaching a single slot in a cross flow 22

4.6 Schematic of a rigid straight fibre of length, L, moving with an average velocity, $\vec{V}$, in a turbulent flow field, $\vec{U}$. The fibre is pointing in the direction of the unit vector $\vec{\mathbf{p}}$. 27

4.7 The dimensionless dispersion, $\frac{\overline{x^2}}{u^2\mathcal{T}^2}$, plotted against dimensionless time, $t/\mathcal{T}$, for several values of dimensionless fibre length, L/Λ equal to 0, 1.0, 2.0, 3.0 and 4.0. 43

4.8 The dimensionless dispersion coefficients, $D_x(L)/D_x(0)$, as a function of fibre length normalized by the integral length scale, L/Λ. 44

5.9 A fibre in two dimensions. Initial conditions indicated by x_0, y_0 and θ_0 . 52

5.10 Schematic diagram depicting the two types of impacts: a type one impact (a) and a type two impact (b) 53

5.11 Computed trajectory of a fibre with $L/W = 3$, demonstrating how several types of impacts occur during a single trajectory ($V_s = 3.04$m/s). The figure shows the fibre at equal time steps along its trajectory. Initially the fibre is free floating (A), then impacts the downstream edge of the slot on one end (B), then rotates onto the side of the fibre (C) and is subsequently pulled out of the slot to become free floating again (D). 58

5.12 An example of a vertically trapped fibre ($L/W = 2$, $V_s = 4.11$m/s). . . . 60

5.13 An example of a horizontally trapped fibre ($L/W = 3$, $V_s = 3.04$m/s). . 60

5.14 An example of a fibre wedged into the slot. ($L/W = 3$, $V_s = 3.04$m/s). . 61

5.15 stream lines calculated from the CFD solutions of the mean flow field in the neighborhood of a single aperture. The slot width is 0.5mm, average channel velocity 7.5m/s. 62

5.16 A "fate plot" showing the results of a fibre trajectory as a function of initial position and orientation. Each point represents the initial height and orientation of a fibre. The symbol represents the results of the fibre's trajectory. Four trajectories are shown demonstrating different possible outcomes. The horizontal line marks the exit layer height of the fluid (L/W=3, $V_s = 3.04$m/s). 65

5.17 The effect of initial height and orientation on passage for fibre with $L/W =$ 0.5 and V_s/V_u of 0.2, 0.41, 0.55, 0.76, 0.93 67

5.18 The probability of passage as a function of height above the wall normalized by exit layer height for $L/W = 0.5$ and all slot velocities. 68

5.19 The effect of initial height and orientation on passage for fibre with L/W=1.0 and V_s/V_u of 0.2, 0.41, 0.55, 0.76, 0.93 69

5.20 The probability of passage as a function of height above the wall normalized by exit layer height for L/W=1.0 and all slot velocities. 70
5.21 The effect of initial height and orientation on passage for fibre with L/W=2.0 and V_s/V_u of 0.2, 0.41, 0.55, 0.76, 0.93 71
5.22 The probability of passage as a function of height above the wall normalized by exit layer height for L/W=2.0 and all slot velocities. 72
5.23 The effect of initial height and orientation on passage for fibre with $L/W =$ 3.0 and V_s/V_u of 0.2, 0.41, 0.55, 0.76, 0.93 73
5.24 The effect of initial height and orientation on passage for fibre with $L/W =$ 4.0 and V_s/V_u of 0.2, 0.41, 0.55, 0.76, 0.93 74
5.25 The probability of passage as a function of height above the wall normalized by exit layer height for $L/W = 3.0$ and all slot velocities. 75
5.26 The probability of passage as a function of height above the wall normalized by exit layer height for $L/W = 4.0$ and all slot velocities. 76

6.27 A schematic of the experimental apparatus, including the camera, square transparent channel, and halogen illumination. 82
6.28 A typical image of the blue dyed, 2mm long nylon fibres, flowing near the plexiglass channel wall. 83
6.29 A schematic diagram of a fibre near the wall, depicting the variables measured for each fibre. 84
6.30 Fibre concentration normalized by the mean channel concentration as a function of height above the wall normalized by the fibre length for 2mm nylon fibres. 85

6.31 Fibre Concentration normalized by the mean channel concentration as a function of height above the wall normalized fibre length for 1mm ($\diamond$), 2mm (+), and 3mm ($\square$) nylon fibres. 86

6.32 Probability density contours for height, y/L, and orientation, θ, for 3mm fibres. 87

6.33 Probability density contours for height, y/L, and orientation, θ, for 2mm fibres. 88

6.34 Probability density contours for height, y/L, and orientation, θ, for 1mm fibres. 88

6.35 The average projected fibre length as a function of height away from the wall, y/L, for 1mm, 2mm and 3mm fibres. 89

6.36 A schematic of a fibre rotating near the wall ($y < L/2$), impacting the wall (A) and being transported away (B). The fibre then rotates more slowly resulting in a preferred positive orientation (C). 91

6.37 High speed video images of a single fibre rotating near the wall. Each frame is time indexed in milliseconds, starting at 544 ms. 93

7.38 Schematic diagram of the fibre concentration profile, channel, exit layer and slot. 97

7.39 The calculated and experimentally determined passage ratios for fibres with a L/W ratio of 1 (L=1mm, W=1mm: Solid Line, $\diamond$) and 2 (L=1mm, W=0.5mm: Dotted Line, +, and L=3mm, W=1.5mm: Dashed Line, $\square$). 100

7.40 The calculated and experimentally determined passage ratios for fibres with a L/W ratio of 3 (L=3mm, W=1mm: Solid Line, $\diamond$) and 6 (L=3mm, W=0.5mm: Dashed Line, $\square$). 101

7.41 The calculated and experimentally determined passage ratios for stiff fibres with a L/W ratio of 6, passing through a contoured (*) and uncontoured (□) aperture. 102

7.42 The calculated and experimentally determined passage ratios for a distribution of stiff nylon fibres as determined by Gooding (1986), for three slot velocities. The channel velocity is 6.4m/s and the slot width is 0.5mm. (Solid Line V_s=3.2m/s, Dotted Line V_s=1.9m/s, Dashed Line V_s=0.9m/s) 103

7.43 The calculated and experimentally determined passage ratios for a distribution of kraft fibres as determined by Gooding (1986), for three slot velocities. The channel velocity is 6.4m/s and the slot width is 0.5mm. (Solid Line V_s=2.0m/s, Dotted Line V_s=1.9m/s, Dashed Line V_s=0.9m/s) 104

7.44 The calculated and experimentally determined passage ratios for a distribution of CTMP fibres as determined by Gooding (1986), for three slot velocities. The channel velocity is 6.4m/s and the slot width is 0.5mm. (Dotted Line V_s=1.9m/s, Dashed Line V_s=0.9m/s) 104

7.45 The calculated and experimentally determined passage ratios for synthetic fibres with a high L/W ratio and two different flexibilities. Tangsaghasaksri (1994) 106

A.46 An ellipsoidal particle in a uniform flow field. 127

A.47 Coordinates and dimension of the tapered, rectangular duct. 128

To Gayle,

For all her love and support.

And

To the memory of my father, Norman.

It is to his standards I strive. I hope he would be proud.

I would never have had this opportunity without the love and encouragement of my family: MaryEnn, Christina, Gordon, Jane and Tracy. Thank You! And thank you Michael, your love and laughter was my greatest inspiration.

There are many other people who deserve acknowledgment: Dick Kerekes, for his support and guidance of this work. Mark Martinez, Robert Gooding, Gordon Robertson, Lisa Brandley and Reid Turner for their help, friendship and inspiration. Darcy Kerr, Peter Magnuson, and Mike Yachiw, who are, and always have been, my friends.

A hundred times every day I remind myself that my inner and outer life are based on the labors of others.

-Albert Einstein

Chapter 1

INTRODUCTION

Wood is converted into paper products through the process of pulping and papermaking. Wood is a composite of hollow cellulose fibres bound together by lignin, a thermal-plastic polymer. Fibres are typically 2 mm in length and about 30 μm in diameter. These fibres are separated from the wood by one of two types of pulping: mechanical pulping, in which fibres are removed mechanically from the wood matrix, or chemical pulping, in which the lignin holding the fibres is dissolved chemically. As a consequence of the pulping process, chemical pulp fibres are long and flexible, whereas, mechanical pulp fibres are short and stiff. The fibres are made into paper by a filtration process in which a fibre mat is formed from a pulp slurry. The resulting fibre mat is dried, and possibly coated, to form high quality paper.

The production of market pulps and various paper grades is Canada's largest net export industry. These products compete in an increasingly competitive global market. Process optimization is essential to meeting new cost, quality and environmental demands.

Screening is an important operation in both chemical and mechanical pulping. Both of these pulping processes leave bundles of unpulped wood. Mechanical pulping is particularly inefficient in this manner. Accordingly, the fibre bundles, called "shives", are contaminants in the pulp that need to be removed. This is accomplished using pressure screens (Fig. 1.1). In this device, a pulp suspension (feed) enters a cylindrical vessel and is accelerated, by a rotor, to a high tangential velocity, parallel to a perforated screen

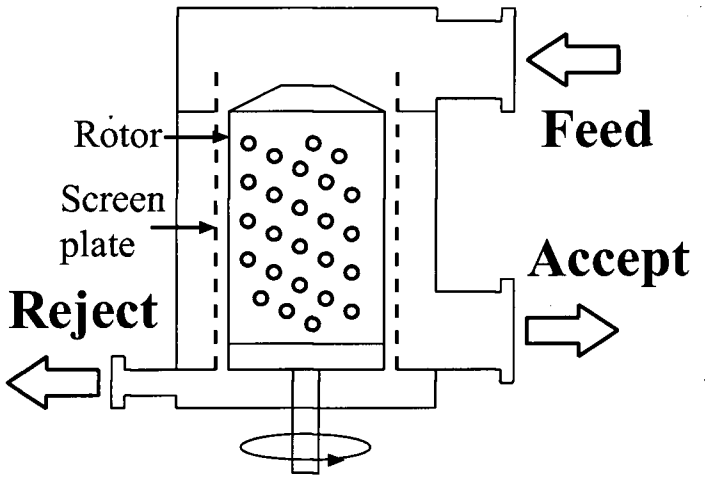

Figure 1.1: Schematic of a typical industrial pulp screen.

plate with either slots or holes. The rotor also produces positive and negative pressure pulses to remove fibres plugging the apertures and to force water and fibres through the apertures. The portion of the suspension that does not pass through the apertures (reject) is rich in contaminant particles. The suspension that passes through the apertures (accept) is rich in fibres.

Apart from contaminant removal, pressure screens can segregate pulp fibres on the basis of length and flexibility. This type of separation is called "fractionation". Fibre fractionation and selective processing of individual fractions leads to higher quality and more uniform pulp that can meet the increasing demand for higher quality paper products. Fractionation is currently practiced to a limited degree in industry [1, 2, 3]. Pressure screens are the most industrially efficient method of fibre fractionation [4].

Enhanced fractionation technology provides Canadian pulp producers an advantage. The Canadian climate produces some of the highest quality fibres in the world, however,

the extreme variability in the climate, and the age distribution of first-growth forests, produces a heterogeneous mixture of coarse and fine fibres, lowering quality. Significant quality improvements could be achieved by the efficient removal of the small percentage of coarse fibres. In contrast, plantation forests in more temperate climates produce coarser fibres, but with greater uniformity.

Efficient separation of fibres by length and coarseness by screening is a formidable challenge. To obtain industrially acceptable throughput, the size of the apertures used in screening must be larger than the fibre diameter, giving every fibre some probability of passage through the aperture. Such separation is known as probability screening. In contrast, barrier screening entails separation of contaminants larger in all dimensions than the aperture, from material that is smaller than the aperture. Probability screening in the pulp and paper industry has been used for years to remove shives from pulp. The technology and practice has advanced largely empirically. The relatively small amount of scientific understanding of this type of screening is discussed in the next section.

Chapter 2

LITERATURE REVIEW

Previous studies relevant to fibre fractionation fall into three broad categories:

- Industrial tests
- Fibre screening studies
- Hydrodynamic studies of suspended particles.

2.1 Industrial Practice

The aim of industrial pulp screening is to operate at a high contaminant removal efficiency with a minimum reject flow. Because there is always some reject flow ($\approx$ 20% in typical pulp screens), industrial screening is carried out in stages. For example, the reject of the "primary" screen becomes the "feed" for the secondary screen, etc. In addition to this staging, screens are operated to minimize reject thickening (increased fibre concentration in the reject flow), which leads to blinding and plugging. Efficiency and reject thickening are linked by the pulp passage ratio [5, 6, 7, 8]. As probability screening efficiency increases, so does the degree of reject thickening.

The mechanisms controlling fibre passage through apertures in an industrial pressure screen are not well understood. Good reviews of current screening equipment, operation and postulated screening mechanisms are given in [9, 10, 11]. One postulate states that a pulp mat forms on the feed side of the screen basket, selectively preventing long fibres reaching the aperture. Another states that the high tangential velocity decreases

the effective open area of the aperture, decreasing the probability of long fibre passage through an aperture. These theories are general in nature, with no experimental evidence to support them.

Separation efficiency of screens depends on three design considerations: (1) operation of the pressure screen, which includes the rotor speed, pulp consistency and reject ratios. [12, 13, 14]; (2) equipment design, for example rotor type, screen plate aperture dimension and style [15, 16, 17, 18, 19, 20]; and (3) system design, that is, how industrial screens are combined together in stages [21, 22].

Previous studies have for the most part been oriented towards the screening of contaminants (*e.g.* shives) from pulp. Fractionation is a more specialized separation. Very little has been published on this subject. Some studies have examined the use of hydrocyclones for fractionation by coarseness [23, 24] and by length [25]. Others, such as that of Scott [4], reviewed industrial fractionation practice using pressure screens and hydrocyclones for recycled pulp. While these studies have examined industrial practice, there have also been other scientific studies of screening that are relevant to both contaminant removal and fibre fractionation.

2.2 Screening Studies

In reviewing the studies of screening, it is useful to establish a picture of fibre behavior near a single aperture in a pulp screen and to define terms for this fibre behavior. These are given in Figure 2.2 below.

As a result of rotor rotation, the velocity parallel to the screen plate, V_u, is sizeable in comparison with the slot velocity, V_s, *i.e.* typically $V_u/V_s > 1$. Also, as stated earlier, fibre diameter, d, is less than slot size, W, *i.e.* $d < W$. Therefore, separation takes place by probability screening. To understand the factors which affect screening under these

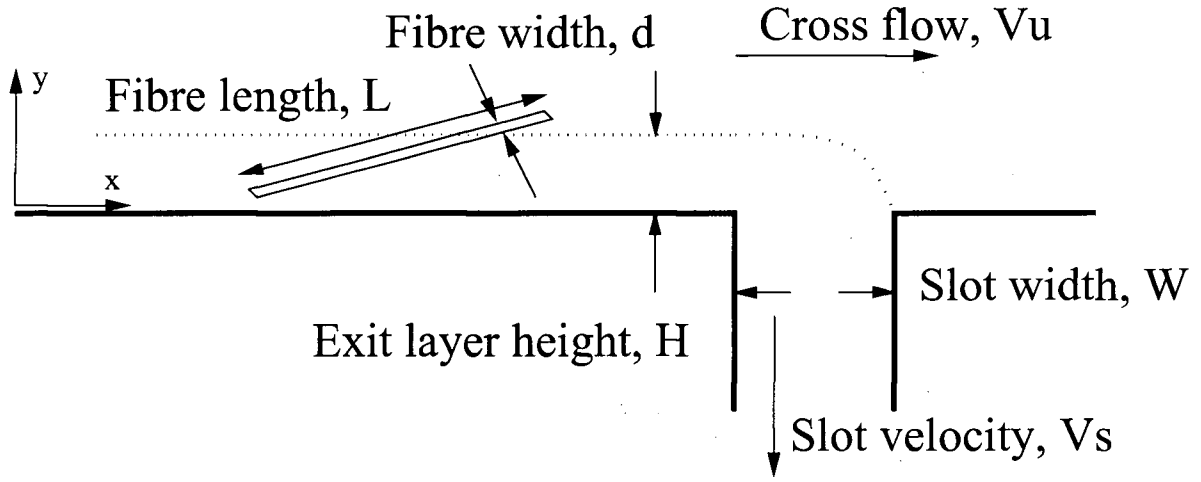

Figure 2.2: A schematic of a single slot in a cross flow, a model pressure screen used to study fibre passage through narrow apertures.

conditions, a simple case of fibres in a very dilute suspension can be examined.

Early investigations of pulp fibre screening [26, 27, 28] analyzed the probability of a particle passing through a model screening system without consideration of the mechanism of fibre passage. Still others, [29] looked at the effect of fibre length and recirculation, on the passage of fibres through a Bauer-McNett classifier.

Tirado [30] showed how the relative size of the fibre with respect to the screen hole diameter affects the probability of passage through a grid consisting of a series of perforations. Here, fibre orientation was simplified to be constant and uniformly distributed in three orthogonal directions. In another study, Estridge [31] studied the initial retention of fibres approaching a grid at normal incidence, and derived a simple probabilistic model based on position and orientation of a fibre just before impacting the grid. A few highly simplified cases were examined. The derived retention rates agreed with the

experimental retention rates. Abrams [32] extended Estridge's model to include the entire retention curve as fibres accumulated on the grid. Experimentally measured values of retention were less than those predicted. This was partially attributed to a possible alignment of fibres, induced by the fluid accelerating through the fibre mat. Riese *et al.* [33] numerically calculated the trajectory and orientation of fibres approaching a grid by considering an ideal flow around the wires of the grid, and used these trajectories to make better estimates of the retention curves found by Estridge and Abrams.

Others have investigated the separation of particles suspended in fluids at tee junctions. Nasr-El-Din and Shook [34] modeled separation of particles in a gas flow at a tee junction. These and other similar studies in the literature have focused on particles with little asymmetry and with dimensions less than or approximately equal to the dimension of the aperture, that is, $W \geq L$, where L is particle length and W is aperture width. In contrast, pulp fibres have both high asymmetry, for example $40 \leq L/d \leq 100$, where d is fibre diameter. In all practical cases, $L > W$ but $d < W$.

Other studies have directly focused on fibre screening as it occurs in pulp pressure screens. Tangsaghasaksri *et al.* [35, 36, 37, 38, 39] experimentally determined the effect of slot velocity, aperture contours, and fibre flexibilities on the passage of model nylon fibres through a single slot in a cross flow. In an effort to quantify and understand their passage ratio results, a semi-empirical model was developed based on fibre trajectories near the slot, fibre impacts, and rotations on the slot edge. A single slot screen has also been used by Yu and DeFoe [40, 41, 42] to investigate the fundamental mechanisms of fibre mat formation on the feed surface of a contoured screen plate. They also studied the motion of individual fibres during passage through highly contoured apertures. They showed that fibre passage depended on the orientation and position of the fibre upstream from the aperture, and that fibres are primarily aligned with the streamlines in the region close to the screen plate. However, these works only provided a qualitative description

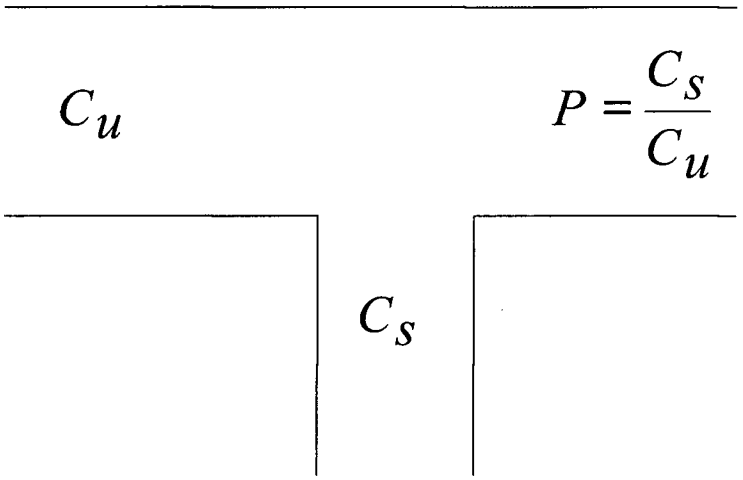

Figure 2.3: Definition of passage ratio, $P = C_s/C_u$

of the observed fibre passage.

Throughout these investigations several mechanisms of fibre passage were proposed and used to describe the observed passage qualitatively. However, quantitative estimates of the principal mechanisms of separation by a single aperture have remained elusive.

The most comprehensive studies of fibre screening in the literature are those produced since 1985 at the University of British Columbia. In the first work from this group, Gooding and Kerekes [7, 5] showed how fibre separation at a single aperture is related to the performance of the entire screen basket. Fibre separation at each aperture is characterized by a "passage ratio", defined as the ratio of the concentration of particles in the flow through the aperture to the concentration upstream of the aperture. The "passage ratio" is illustrated in Figure 2.3. By treating the screen basket as a system of apertures and assuming passage ratio is constant along the screen plate, and further assuming that either a plug or mixed flow existed within the screen, contaminant separation efficiency was related to reject ratio, giving "performance equations" for pulp screens.

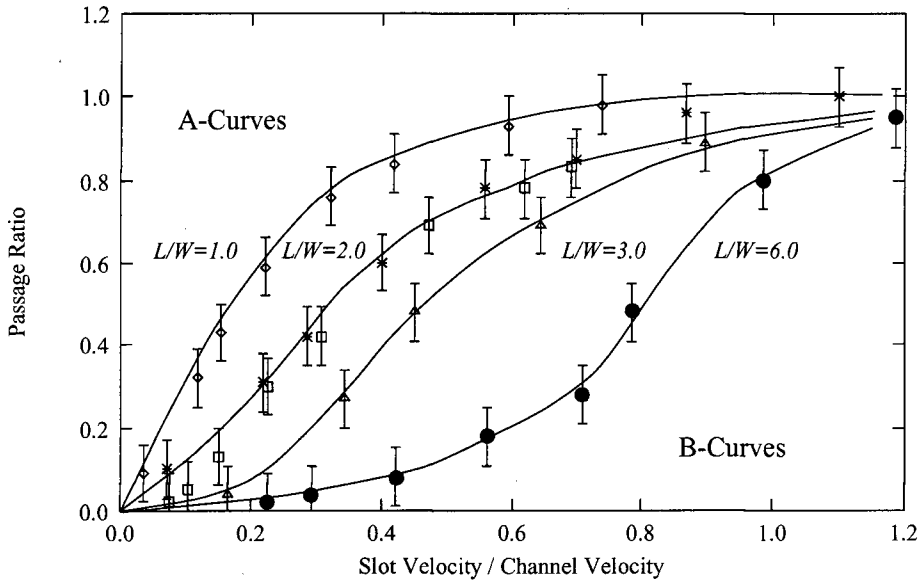

Figure 2.4: Passage ratio for several fibre length, L, to slot width, W, ratios as a function of slot velocity, V_s normalized by channel velocity, V_u (Kumar, 1991). The symbols are : L=1.0mm and W=1.0mm ($\diamond$), L=1.0mm and W=0.5mm (*), L=3.0mm and W=1.5mm ($\square$), L=3.0mm and W=1.0mm ($\triangle$), L=3.0mm and W=0.5mm ($\bullet$)

.

In another study, fibre passage through a single aperture was also studied using a single slot screen (SSS) [7, 43]. The SSS is an experimental flow loop with a single slot perpendicular to the flow. The flow through the channel gives a velocity parallel to the plane containing the aperture, V_u, and a velocity through the slot, V_s, as illustrated earlier in Figure 2.2. Using high speed cinematography, the trajectories of fibres approaching the aperture were observed. Based on these observations, fibre passage was postulated to be governed by two effects: a "wall effect" and a "turning effect". The wall effect was due to the concentration gradient of fibres perpendicular to the wall upstream of the slot. As a consequence of this gradient, the thin fluid layer near the channel wall entering the slot had less fibres than the average. This alone created a screening effect. The "turning effect" referred to the effect of aperture entry flow on fibre passage, for example, whether the fibre enters the slot, or rotates into the slot but is swept back into the channel.

Kumar [44] experimentally demonstrated how fibre length, slot width and fluid velocities near a single slot affected the probability of fibre passage. He observed two distinct types of passage ratio curves as a function of V_s/V_u: a concave "A" curve when $L/W \leq 2$ and an S-shaped "B" curve when $L/W \geq 2$ (see Figure 2.4). Kumar characterized this behavior by dimensionless penetration, bending, and rotation parameters. He also observed similar findings in a laboratory screen simulating a commercial pulp screen.

2.3 Hydrodynamic Studies of Suspended Particles

As shown above, the published scientific studies of fibre screening are relatively few in number. However, there is a large body of work in the scientific literature on flow behavior of suspended particles. In this section, we review the portion of this previous work that is relevant to pulp screening. The review is in three parts:

- low Reynolds number particle hydrodynamics
- particle motion in turbulent flow
- particle motion near a solid wall

2.3.1 Low Reynolds Number Particle Hydrodynamics

The equations of motion for a fibre flowing in a viscous fluid are derived from the forces acting on a fibre as it moves through a flow field. The first investigation into the motion of non-spherical particles in a fluid was that of Jeffery [45]. This pivotal paper calculated the forces and moments on an inertialess ellipsoidal particle moving in a homogeneous, Stokes flow. (Homogeneous flow assumes that the fluid velocity varies linearly in the neighborhood of the particle.) The analysis was experimentally verified for fibres, discs and spheres in various flows by several investigators [46, 47, 48, 49]. Recently, Jeffery's

analysis has been shown to accurately predict the orientation of fibres in semi-dilute suspensions [50]. Jeffery's equations have also been solved numerically in a computationally derived flow field. They accurately predicted the orientation distribution of fibres in fibre reinforced composite materials [51, 52].

Jeffery's analysis shows that an ellipsoid rotates in a simple shear flow having velocity gradients $\frac{\partial U}{\partial x}$, $\frac{\partial U}{\partial y}$, $\frac{\partial V}{\partial x}$, $\frac{\partial V}{\partial y}$, at the following rotational velocity:

$$\frac{d\theta}{dt} = \frac{\frac{1}{2}(\alpha^2 - 1)\sin(2\theta)(\frac{\partial V}{\partial y} - \frac{\partial U}{\partial x}) + (\sin^2(\theta) + \alpha^2\cos^2(\theta))\frac{\partial V}{\partial x} - (\cos^2(\theta) + \alpha^2\sin^2(\theta))\frac{\partial U}{\partial y}}{\alpha^2 + 1} \tag{2.1}$$

where $\alpha = L/d$ is the aspect ratio of the two-dimensional ellipse, U and V are the x and y components of fluid velocity and θ is the angle the major axis of the ellipse makes with the x-axis. Also, the equation of translation shows that the centre of the particle follows the fluid streamlines in a homogeneous flow field. See Appendix A for the derivation of Equation 2.1.

Others [53, 54, 55, 56, 57, 58] have generalized the work of Jeffrey to particles of arbitrary shapes. Burgers [59], using slender body theory, approximated the force per unit length by a fourth-order polynomial of position along the slender body (fibre). Stokes' equation was solved for the special case of slender bodies, using a line of "Stokelets" which represent the distribution of forces [60]. Again, this method was only used in a homogeneous flow field. Cox [61] solved Stokes' equation for slender bodies but generalized the theory to an arbitrary, nonhomogeneous flow field with a nearly arbitrary fibre shape. He showed that the drag tensor was, to a first-order approximation, independent of the flow field and fibre position, but to a second-order approximation is dependent on the entire flow field surrounding the particle and position along the fibre.

Cox's equation for the force per unit length, $\vec{F}$, on a slender body is given by

$$\frac{\vec{F}}{2\pi\mu} = \left[\frac{\vec{u}_f - \vec{u}_p}{\ln\alpha} + \frac{\vec{J} + (\vec{u}_f - \vec{u}_p)\ln(2\epsilon/\lambda)}{(\ln\alpha)^2}\right]\cdot\left[\frac{d\vec{R}}{ds}\frac{d\vec{R}}{ds} - 2I\right] + \frac{\vec{u}_f - \vec{u}_p}{2(\ln\alpha)^2}\cdot\left[3\frac{d\vec{R}}{ds}\frac{d\vec{R}}{ds} - 2I\right] + O(\frac{1}{(\ln\alpha)^3}) \tag{2.2}$$

where $\vec{J}$ is given by

$$J_i = \frac{1}{2}\left[\int_{-1}^{s-\epsilon} + \int_{s+\epsilon}^{1}\right]\left\{\frac{\delta_{ij}}{|\vec{R} - \hat{\vec{R}}|} + \frac{(R_i - \hat{R}_i)(R_j - \hat{R}_j)}{|\vec{R} - \hat{\vec{R}}|^3}\right\}\left\{\delta_{jk} - \frac{1}{2}\frac{d\hat{R}_j}{d\hat{s}}\frac{d\hat{R}_k}{d\hat{s}}\right\}(u_{f_k}(\hat{\vec{R}}) - u_{p_k}(\hat{s}))d\hat{s} \tag{2.3}$$

and

$$\begin{aligned}
\vec{u}_f &= \text{fluid velocity vector} \\
\vec{u}_p &= \text{particle velocity vector} \\
\alpha &= \text{aspect ratio of fibre } (L/d) \\
s &= \text{dimensionless parameterization of fiber length} \\
\vec{R} &= \text{position vector along fibre, parameterized by s} \\
\hat{\vec{R}} &= \text{position vector along fibre, evaluated at } s = \hat{s} \\
\epsilon &= \text{arbitrary constant, taken as the limit as } \epsilon \to 0 \\
\lambda &= \text{dimensionless cross sectional area of the fibre} \\
\mu &= \text{fluid viscosity} \\
I &= \text{identity matrix} \\
\delta &= \text{Kronecker delta function}
\end{aligned} \tag{2.4}$$

Johnson [62] derived a similar relation assuming that the ends of the slender body were ellipsoidal. Cox's work was later extended to the case of Oseen's flow to estimate inertial effects on the force distribution [63].

Others [64, 65, 66], assuming the force distribution along the length of the fibre to

be constant (ignoring any end effects of the fibres), modeled slender body motion in nonhomogeneous flow fields. Unbeknownst to them, similar assumptions and equations had been used two decades earlier [33] to predict fibre orientation and position. A similar model based on an approximate drag coefficient was also used by Zhou [67] to estimate fibre orientation.

Recently, the same equations have also been used to study the motion of pulp fibres as they approach a single contoured slot in a cross flow [35], the case of interest in this investigation. This study showed how fibres impact with the aperture's contour and the aperture's downstream edge for different flow conditions. Trajectories were only calculated up to the point at which the fibre impacted the slot. From the orientation and position of the fibre at the point of impact, the probability of a fibre passing through the aperture was qualitatively discussed.

2.3.2 Turbulent Particle Motion

The fluctuating component of velocity in turbulent flow gives rise to the dispersion of both suspended particles and dissolved material in a manner similar to random molecular motion in molecular diffusion. In gases, molecules randomly collide and scatter. This scattering is called diffusion. In fluids, the random motion of fluid elements (eddies) imparts a continuous random motion on suspended particles. Repeated eddy interactions cause the particles to be dispersed over time.

Taylor (1921) [68] provided the first investigation into turbulent dispersion. This classical paper relates the mean square displacement of a diffusible property, originating from a point source, to the Lagrangian[1] velocity correlation of the fluid. In this work the diffusible property is assumed to follow the fluid exactly, that is, the particle's Lagrangian

[1]Lagrangian refers to a frame of reference moving with a single particle, as opposed to the more familiar Eulerian or laboratory frame of reference used to describe fluid properties.

velocity correlation is assumed to be the same as the fluid's. Although this assumption makes it easier to relate the dispersion of the particles to the turbulence of the fluid, the Lagrangian velocity correlation of the fluid is usually unknown.

Much of the theoretical work following Taylor's analysis focused on methods of relating the statistical properties of turbulent flow in an Eulerian frame of reference to a Lagrangian one. Saffman [69] calculated the Lagrangian velocity correlation using a model of turbulence similar to that proposed by Corrsin [70], Kraichnan [71] and Batchelor [72]. From the Lagrangian velocity correlation of the model turbulence, Saffman numerically calculated the Lagrangian time scale as

$$T_L = \frac{0.4 L_p}{(\overline{u^2})^{\frac{1}{2}}} \tag{2.5}$$

where L_p is the Eulerian longitudinal length scale and $(\overline{u^2})^{\frac{1}{2}}$ is the root mean square of the turbulent velocity component. From this, an approximation of the relative magnitude of the two time scales is given by

$$\frac{T_L}{T_E} = 0.4 \tag{2.6}$$

This value is partially supported by the experimental evidence of Snyder and Lumley [73], but a range from 0.2 to 1.0 is reported. A good discussion of how this theory has evolved can be found in Hinze [74].

Kraichnan's direct interaction approximation of turbulence [75, 76] showed that the Lagrangian time scales are less than the corresponding Eulerian time scales. Kraichnan [77] showed good agreement between the direct interaction approximation and exact computer simulations for his turbulence model. Pythian [78] used a series of successive approximations to relate the Lagrangian fluid velocity correlation to the Eulerian correlation. Truncation of this series after the first two terms showed good agreement with the exact solutions of Kraichnan's [77] turbulence model. Lundgren and Pointin [79] used

Corrsin's analysis to calculate the Lagrangian velocity correlation function and obtained good agreement with those calculated using Kraichnan's turbulence model.

A recent model of turbulence simulated by a series of unsteady Fourier modes, proposed by Fung *et al.* [80], reproduced more of the turbulent phenomena found in real turbulence. In general, the closed form approximation methods used to relate the Eulerian statistics to the Lagrangian statistics of the turbulent fluid give similar results. With the great increase in computer power in recent years, direct numerical computations of turbulence from the Navier-Stokes equations are now possible. This technique may definitively show the relation between Eulerian and Lagrangian fluid statistics. A summary of the recent theoretical and experimental comparisons of Eulerian and Lagrangian scales is given in [81]. The turbulence models used to relate the fluid's Eulerian and Lagrangian statistics yield similar results. They show that the Lagrangian fluid velocity correlation function has the same form as the Eulerian correlation function but has a smaller magnitude.

The particle Lagrangian velocity correlation, *i.e.* the fluid's velocity correlation averaged over the path of the particle, is not the same as the fluid's Lagrangian velocity correlations (the fluid's velocity correlation taken along the path of a fluid element). The fluid and particle Lagrangian velocity correlations differ because the particle does not follow the fluid exactly. The difference in path is attributed to particle inertia, particle size, or external body forces. To calculate these correlations, recent work on particle motion in turbulent flow has focused on integrating the equation of motion of particles through some model turbulence field. Unfortunately, the problem of finding an adequate representation of a turbulent flow field, with appropriate Lagrangian statistics, remains. However, these techniques have been useful for theoretical studies of the effect of inertia on particle motion.

One of the first computer simulations of particle motion through a turbulent fluid was

by Patterson and Corrsin [82]. Also, Reeks [83], using a linear Stokes drag relation and Phythian's [78] turbulence model looked at inertia and the effect of gravity on dispersion. He showed that, for particles of greater density than the fluid, the particle velocity correlation approached the fluid's Eulerian correlation, and the resulting long time particle diffusivity was greater than the fluid's. Pismen and Nir [84] examined the effect of particle inertia using a linear drag function and Kraichnan's turbulence model [77]. Their results indicate that particle inertia affects dispersion in two ways: the Lagrangian time scale increases towards the Eulerian time scale as particle inertia increases, and at the same time, the particle's energy $((\overline{u^2})^{\frac{1}{2}})$ decreases. Since dispersion is proportional to the product of these two terms, the effect of inertia on dispersion is less than expected.

A similar computational approach for determining real particle dispersion, models particle motion as a series of discontinuous steps forming a random walk. Each random step represents a particle-eddy interaction, in which the particle is assumed to move in a single direction during an interaction with a single eddy. This approach seems to reproduce some of the experimental observations of particle dispersion. For example, a random walk simulation of dispersion from a single point [85, 86] showed good agreement with the experiments of Snyder and Lumley [73] over a wide range of particle densities. This technique can be readily extended to the case of non-homogeneous, non-isotropic turbulent flow fields. A comparison of particle dispersion calculation methods is given in [81].

2.3.3 Turbulent Particle Motion Near Walls

The theoretical techniques outlined above have also been used to study the interactions of particles in turbulent flow near a solid boundary. These theoretical techniques typically involve integrating the equation of motion of a particle, assuming a Stokes drag force, through some type of model turbulence. A number of recent investigations are outlined

in terms of the force model and turbulence model.

Kallio and Reeks [87] used a linear Stokes drag relation and Saffman lift forces for rotating spheres in a linear velocity gradient. The size of the particles is assumed to be less than the smallest scales of turbulence. The turbulent flow field was modeled as a Gaussian random velocity with mean and r.m.s. that correspond with the classical experimentally measured log-law and buffer layers near the wall. They showed that the concentration of suspended particles was greater than the mean concentration in the region $y^+ < 10$ (y^+ is the inner wall variable). A similar approach of using Saffman lift forces has been used by several people including Sommerfeld [88, 89], where the particle's rotation and resulting lift force depend on the impact between the spherical particle and the duct wall. Here the calculated particle concentration was substantially less near the duct wall. Pedinotti [90] used a direct numerical simulation method to model the inhomogeneous, turbulent fluid velocity field near a duct wall, and a linear drag relation to calculate particle trajectories. He showed a marked increase in particle concentration near the duct wall. Underwood [91] used a random walk method to calculate particle trajectories near the wall and showed that particle concentration increases near the duct wall. He hypothesized that particles gather where the fluid fluctuations are lower. However, there is some question as to whether these findings are an artifact of the computation.

2.3.4 Turbulent Fibre Motion

Although there is a large body of scientific literature on particle motion in turbulent flow, there are relatively few studies directly relevant to highly elongated, orientable, particles (fibres) in turbulent flow.

One of the first studies of fibre motion in turbulent flow was by Cho *et al.* [92] who investigated the effect of atmospheric turbulent fluctuations on the preferred settling

orientation of high aspect ratio ice crystals (fibres), in cumulonimbus clouds. After estimating the time for a fibre to become oriented, and the time between eddy interactions, they concluded that atmospheric turbulence will not greatly affect the mean particle orientation.

Kagermann and Köhler [93] modeled turbulent translational and orientational dispersion assuming a linear, Stokes drag relation, Jeffery's rotation equation and Kraichnan's turbulence model. Inherent in these simplifications is the assumption that the particle is smaller than the smallest scales of turbulence. The orientation distribution function of small fibres in turbulent flow has also been theoretically calculated by Krushkal and Gallily [94] using the Fokker-Planck equation. A key parameter in this equation is the rotational Peclet number, $\mathcal{P}_e$, which is the ratio of a typical velocity gradient, dU/dx, to the rotational dispersion coefficient, D_p, that is, the ratio of orienting to randomizing effects, *i.e.*,

$$\mathcal{P}_e = \frac{dU/dx}{D_p} \tag{2.7}$$

Here the dispersion coefficient was estimated by dimensional analysis and the Kolmogorov local isotropy hypothesis for small eddies to be

$$D_p = (\epsilon/\nu)^{1/2} \tag{2.8}$$

This ratio is related to the fluctuating component of the fluid velocity, u_i, through the following relationship

$$\epsilon/\nu = \sum_{ij} \overline{\left(\frac{du_i}{dx_j}\right)^2} \tag{2.9}$$

Sanders and Meyer [95] computed the concentration profile across a pipe using a two-fluid model in which the water and fibres are each considered a continuum. They compared their results to an experimentally-determined concentration profile and showed

a power law consistency distribution across the pipe. The velocity profile of a fibre suspension has been studied using NMR techniques [96]. These works showed the existence of a low consistency, fibre depleted annulus close to the pipe wall. There have been other studies of fibre motion, including a study of glass fibre deposition onto human lung trachea [97, 98].

Recently, the axial and lateral orientations of glass fibres in turbulent and laminar pipe flow have been directly measured by automated image analysis [99]. The flow was characterized by its Reynolds number and its rotational Peclet number defined above. It was found that near the pipe centre, for low Reynolds number laminar flow, the axial fibre orientation distribution is broad, with no real preferred orientation. As Reynolds number increased within the laminar regime, consequently increasing the Peclet number, the axial orientation distribution became sharper. At high Reynolds number and low Peclet number turbulent flow, the randomizing component of the turbulence created an almost uniform fibre orientation distribution.

2.4 Nomenclature

Table 2.1: The following nomenclature was used in this section.

α	Aspect ratio of particle.
C_s	Average fibre concentration in fluid passing through the slot.
C_u	Average fibre concentration in fluid upstream of the slot.
D_p	Rotational dispersion coefficient.
ϵ	Turbulent kinetic energy dissipation.
H	Exit layer height.
L	Fibre length.
L_p	Eulerian integral length scale.
ν	Kinematic viscosity.
P	Passage ratio, $P = \frac{C_s}{C_u}$.
$\mathcal{P}_e$	Rotational Peclet number.
θ	Angle of the particles major axis with respect to the x-axis.
t	Time.
T_L	Lagrangian integral time scale.
T_E	Eulerian integral time scale.
U, V	x, y components of fluid velocity.
u	Fluctuating component of fluid velocity; turbulent velocity.
V_s	Average slot fluid velocity.
V_u	Average upstream channel fluid velocity.
W	Slot width.
x, x_i, y	Cartesian coordinates.
y^+	Inner wall variable.

Chapter 3

PROBLEM DEFINITION

As discussed earlier, Gooding [7] and Kumar [44] studied the passage of fibres through slots under conditions similar to pulp pressure screening, that is, flow approaching a slot at a high velocity parallel to the plane in which the slot was located. In pulp screens, this large parallel velocity is induced by the tangential velocity of the rotor. Both works showed that this upstream velocity was an important factor in determining fibre passage, and that a component of the screening effect resulted from the fibre concentration gradient near the wall caused by this flow. However, they did not investigate in detail the effect of these conditions and of hydrodynamic forces on passage.

The previous literature on fibre flow near a wall is of limited use in understanding the case appropriate for screens. Most of the past studies have focused on fibre motion in laminar flow. Only a few theoretical investigations of fibre orientation in turbulent flow have been reported, and only for the case of fibre length being less than the smallest scales of turbulence. In pulp screens this is not the case.

In the final analysis, the essence of screening is whether a fibre does or does not pass through an aperture. Building upon past work, the overall objective of this thesis is to establish the influence of upstream and entry flow conditions on fibre passage into slots under conditions found in pulp pressure screens.

The appropriate starting point is the work of Gooding [7] and Kumar [44], specifically their "passage ratio", defined as

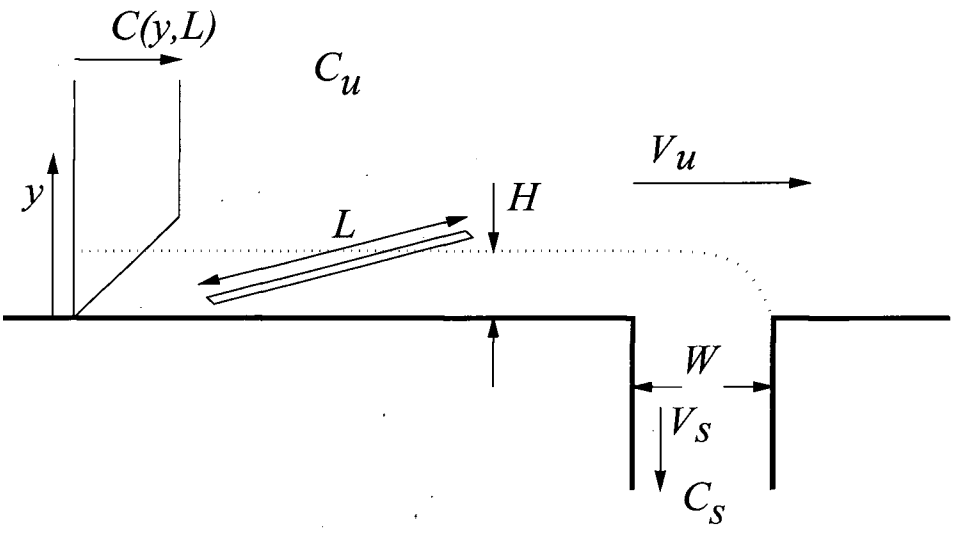

Figure 3.5: A fibre approaching a single slot in a cross flow

$$P = \frac{C_s}{C_u} \tag{3.10}$$

where C_u is the mean fibre concentration in the upstream flow and C_s is the mean fibre concentration in the flow passing through the aperture. These concentrations and average velocities, V_u and V_s, are shown in Figure 3.5.

In the previous studies of passage ratio only the mean variables were considered in the analysis. In addition to the mean variables, we consider local variables $v(y)$, $C(y)$ and $p(y)$, defined as:

- $v(y)$, particle velocity at height y above the wall. In the calculation of passage ratio the particle velocity is approximated as the local fluid velocity.
- $C(y)$, concentration of fibres at height y.
- $p(y)$, probability of fibre passage at height y.

From a simple mass balance, we can express passage ratio, P, as

$$P = \frac{1}{P_e} \int_0^\infty \frac{v(y)}{V_u} \frac{C(y)}{C_u} p(y) \frac{dy}{L} \tag{3.11}$$

where P_e is the penetration parameter defined by Kumar as

$$P_e = \frac{V_s W}{V_u L} \tag{3.12}$$

The local variables play a significant role in determining fibre passage. For example, $C(y)$ reflects the "wall effect", in which a screening effect takes place simply because there are fewer fibres in the flow passing into the aperture than in the main flow. More importantly if different types of fibres have different concentration profiles, $C(y)$, this alone will induce fractionation. Similarly, $p(y)$ reflects the "turning effect" described in earlier work. Differing values of $p(y)$ also contribute to the separation of one fibre type from another. In this analysis, we make the simplifying assumption that particle velocity profile is approximately the same as the local fluid velocity profile.

The specific objective of this thesis is to determine the factors that affect C(y) and p(y) for fibres of different lengths. The approach to accomplish this is:

1. Theoretically investigate the behavior of fibres in turbulent flow.

2. Incorporate this theory into a numerical simulation of fibre trajectories in the vicinity of an aperture.

3. Theoretically estimate the probability of passage function based solely on the simulated fibre trajectories.

4. Experimentally determine the upstream fibre concentration profile as a function of fibre length.

5. Estimate passage ratios from the probability of passage function and the concentration profile and compare them with experimentally measured passage ratios in the literature.

3.1 Nomenclature

Table 3.2: The following Nomenclature was used in this section.

C_s	Average fibre concentration in fluid passing through the slot.
C_u	Average fibre concentration in fluid upstream of the slot.
$C(y)$	Fibre concentration profile in fluid upstream of the aperture.
H	Exit layer height.
L	Fibre length.
P	Passage ratio, $P = \frac{C_s}{C_u}$.
$p(y)$	Probability of passage function.
P_e	Penetration number, $P_e = \frac{V_s W}{V_u L}$.
V_s	Average slot fluid velocity.
V_u	Average upstream channel fluid velocity.
$v(y)$	Particle velocity profile upstream of the aperture, approximated as the fluid velocity profile.
W	Slot width.
y	Distance from the channel wall; Cartesian co-ordinate.

Chapter 4

FIBRE MOTION IN TURBULENT FLOW

4.1 Introduction

The first step towards an understanding of fibre passage through narrow wall apertures is to develop a mathematical description of fibre motion in a turbulent shear flow. Fibre particles suspended in a turbulent flow experience a mean velocity associated with the mean flow field and a random velocity due to the fluctuating component of the turbulent flow. For fibres, motion is a combination of translation and rotation. The orientation of fibres depends on the combination of orienting effects of the mean velocity gradients and the randomizing effects of turbulence. As well, the translation of fibres depends on the mean and turbulent fluid velocities. As described earlier, most of the past studies are for particles smaller than the smallest scales of turbulence. Here we examine larger fibres in turbulent flow near walls.

To analyze this problem, simplifying assumptions must be made. We assume fibres to be rigid, straight, and having a diameter that approaches zero. The equations of fibre motion are derived based on these assumptions. Fibre motion is then decomposed into mean and fluctuating components. The equations for mean fibre motion are later used for a numerical simulation of fibre trajectories through the highly non-linear, bifurcating flow field surrounding an aperture in the wall (Chapter 5).

The equations of motion for the turbulent component of fibre velocity in rotational and translational dispersion are derived assuming a homogeneous, isotropic turbulent

flow field. Assuming a known Lagrangian particle correlation function, the effects of fibre length on dispersion are investigated.

4.2 Equations of Motion

The earliest investigation into the motion of non-spherical particles in a carrier fluid is that of Jeffery [45]. He calculated the total force and moment exerted by the surrounding fluid on an ellipsoidal particle moving in a Stokes flow, and assuming an inertialess particle and constant fluid velocity gradient, gave the classical expressions for the orbital motion of particles within a simple shear flow. Cox [61] developed an insightful analytical series approximation for the force distribution along the length of a fiber in Stokes flow. As Reynolds number, based on fibre diameter, approaches zero (*i.e.*, $\lim Re \rightarrow 0$) the force per unit length along the fibre, $\vec{f}$, is approximated by a linear Stokes drag relation

$$\vec{f}(l) = D[\vec{U}(l) - \vec{\mathbf{V}}(l)] \tag{4.13}$$

where D is a constant drag tensor, independent of the position along the fibre. $\vec{\mathbf{V}}$ is the velocity of any point on the fibre along its length and $\vec{U}$ is the velocity of the fluid, as a function of position along the length of the fibre, l. A linear Stokes force has been used to successfully predict and model particle motion in turbulent flow by several investigators [87, 84]. For spherical particles a modified Stokes equation has also been used that takes into account particle oscillations [100, 74].

If the fiber is assumed to be straight and rigid then the velocity at any point along the fibre will be the sum of the fibre's translational velocity, $\vec{V}$, and rotational velocity, $l\dot{\vec{\mathbf{p}}}$, where $\dot{\vec{\mathbf{p}}}$ is the time derivative of a unit vector parallel to the fibre's major axis, and l is the distance from the fibre centre (see Figure 4.6). The net external force on the particle is obtained by integrating Equation 4.13 along the length of the fibre

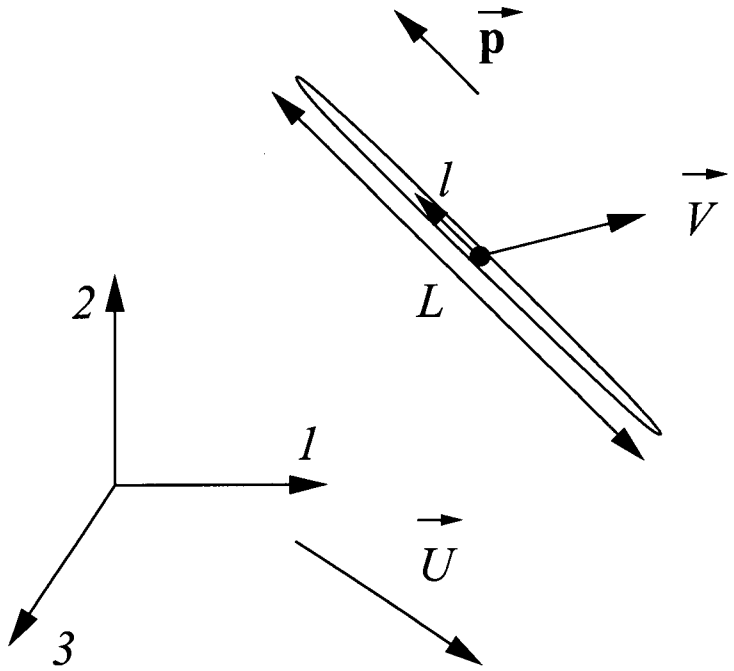

Figure 4.6: Schematic of a rigid straight fibre of length, L, moving with an average velocity, $\vec{V}$, in a turbulent flow field, $\vec{U}$. The fibre is pointing in the direction of the unit vector $\vec{\mathbf{p}}$.

$$\vec{F} = \int_{-L/2}^{L/2} D[\vec{U}(l) - (\vec{V} + l\dot{\vec{\mathbf{p}}})]dl \tag{4.14}$$

The net external moment acting on the fibre is similarly given by

$$\vec{M} = \int_{-L/2}^{L/2} l\vec{\mathbf{p}} \times D[\vec{U}(l) - (\vec{V} + l\dot{\vec{\mathbf{p}}})]dl \tag{4.15}$$

Assuming the inertial forces are negligible in generating relative velocities between the particle and fluid, results in $\vec{F} = 0$ and $\vec{M} = 0$. For this condition,

$$\vec{V} = \frac{1}{L}\int_{-L/2}^{L/2} \vec{U}(l)dl \tag{4.16}$$

and similarly for orientation

$$\dot{\vec{\mathbf{p}}} = \frac{12}{L^3}\int_{-L/2}^{L/2} l\vec{U}(l)dl \tag{4.17}$$

The assumption of an inertialess particle, and a linear Stokes drag has been used in almost all investigations of fibre motion in laminar flow. The time averaged equations have been used by Reise *et al.* [33] to predict fibre passage through circular apertures at perpendicular incidence, and by Tangsaghasaksri [35] in the study of fibre passage through screen apertures. In the study of reinforced composites, these equations have been used by several investigators [66, 65, 64] to predict rheological and end-product strength characteristics. As well, these equations of motion are identical to those given by Jeffery [45], assuming a constant fluid velocity gradient tensor and a large fibre aspect ratio. In this application, the approximation of an inertialess fibre is consistent with the estimate of the fluid forces on a fibre in turbulent flow.

4.2.1 The Equations of Mean Motion

In a turbulent flow field the fluid velocity consists of a time averaged or mean component, $\vec{U}$, and a fluctuating component, $\vec{u}$. The total fluid velocity is given by

$$\vec{U} = \bar{\vec{U}} + \vec{u} \tag{4.18}$$

The mean motion of the fibres is obtained by substituting Equation 4.18 into Equations 4.16 and 4.17 and averaging. The equations of mean fibre motion are then given by

$$\dot{\bar{\vec{V}}} = \frac{1}{L}\int_{-L/2}^{L/2} \bar{\vec{U}}(l)dl \tag{4.19}$$

and

$$\dot{\vec{p}} = \frac{12}{L^3}\int_{-L/2}^{L/2} l\bar{\vec{U}}(l)dl \tag{4.20}$$

The mean fibre velocity is the average of the mean fluid velocity field, averaged over the length of the fibre. The fibre's mean rotational velocity is the first moment of the mean fluid velocity, taken over the length of the fibre. These equation have been derived for laminar flow by several investigators [33, 35, 64, 65, 66].

4.2.2 The Equations of Turbulent Motion

The turbulent motion of the fluid causes fibre velocity and orientation to fluctuate in a random manner, leading to dispersion. Fibre translational and orientational dispersion, based on the equations of motion, are derived below.

Translational dispersion

Substituting Equation 4.18 into the equation of translational fibre motion (Equation 4.16), and changing the limits of integration, the fluctuating component of the fibre's translational velocity, $\vec{v}$, is given by

$$v_i = \frac{1}{L}\int_0^L u_i(l)dl \tag{4.21}$$

Following a single particle as it moves through the carrier fluid (*ie.* using a Lagrangian particle frame of reference) the position, x_i, of the particle as a function of time is given by

$$x_i = \int_0^t v_i dt = \frac{1}{L}\int_0^t \int_0^L u_i(l,t')dldt' \tag{4.22}$$

The magnitude of the particle's mean square displacement is calculated from Equation 4.22 as

$$\overline{x_i x_j} = \overline{\frac{1}{L}\int_0^t \int_0^L u_i(l,t')dldt' \frac{1}{L}\int_0^t \int_0^L u_j(l',t'')dl'dt''} \tag{4.23}$$

The above equation is related to the turbulent velocity correlation following the analysis of Taylor [68] for a tracer particle or fluid element, but extended to account for fibres with lengths that extend through the fluid. Simplifying the above yields

$$\overline{x_i x_j} = \frac{1}{L^2}\int_0^t \int_0^t \int_0^L \int_0^L \overline{u_i(l,t')u_j(l',t'')}dldl'dt'dt'' \tag{4.24}$$

This equation is further simplified by first considering the spatial integrals and realizing that for the same random function (*i.e.* i=j) the integrand is symmetric over the area of integration defined by the square [0,L] and [0,L]. Therefore, integration over the square is equivalent to twice the integration over a triangular region, depicted by

$$\int_0^L \int_0^L dldl' = 2\int_0^L \int_0^l dl'dl \tag{4.25}$$

Doing this for both time and space results in

$$\overline{x_i x_i} = \frac{4}{L^2}\int_0^t \int_0^{t'} \int_0^L \int_0^l \overline{u_i(l,t')u_i(l',t'')}dl'dldt''dt' \tag{4.26}$$

Here the summation notation for repeated indices is not used. Introducing a change of variables $l' = l + \delta$ and $t'' = t' + \tau$ the above becomes

$$\overline{x_i x_i} = \frac{4}{L^2}\int_0^t \int_{-t'}^0 \int_0^L \int_{-l}^0 \overline{u_i(l,t')u_i(l+\delta,t'+\tau)}d\delta dld\tau dt' \tag{4.27}$$

The integrand equals the particle's Lagrangian velocity correlation function, $\mathcal{R}$, multiplied by the square of the fluctuating component of the fluid. When averaged over l and t' for steady, homogeneous turbulence, $\mathcal{R}$ is a function of τ and δ and it is independent of l and t', that is

$$\frac{\overline{u_i(l,t')u_i(l+\delta,t'+\tau)}}{\overline{u_iu_i}} = \mathcal{R}_{ii}(\delta,\tau) \tag{4.28}$$

In general, the spatial $\mathcal{R}_{ii}$ is a function of the spatial vector separating the points of velocity measurement, that is $\mathcal{R} = \mathcal{R}_{ii}(l\vec{p})$. Assuming the fibre is randomly oriented, a simplifying assumption is introduced that the fluid's velocity correlation in the direction of the fibre axis (longitudinal) and perpendicular to the fibre axis (transverse) is identical. This is not strictly true, with classic theoretical relationships existing between the two correlations [74].

Noting that $\mathcal{R}_{ii}(\delta,\tau)$ is symmetric about the origin, Equation 4.27 becomes

$$\overline{x_ix_i} = \overline{u_iu_i}\frac{4}{L^2}\int_0^t\int_0^{t'}\int_0^L\int_0^l \mathcal{R}_{ii}(\delta,\tau)d\delta dl d\tau dt' \tag{4.29}$$

The spatial and temporal integrals, in the above equation, can be further simplified by integrating each pair by parts. First the spatial integrals are simplified.

$$\overline{x_ix_i} = \overline{u_iu_i}\frac{4}{L^2}\int_0^t\int_0^{t'}\left[l\int_0^l \mathcal{R}_{ii}(\delta,\tau)d\delta\Big|_0^L - \int_0^L l\mathcal{R}_{ii}(l,\tau)dl\right]d\tau dt' \tag{4.30}$$

Changing variables in the second part of the integration, from l to δ, the equation becomes

$$\overline{x_ix_i} = \overline{u_iu_i}\frac{4}{L^2}\int_0^t\int_0^{t'}\left[L\int_0^L \mathcal{R}_{ii}(\delta,\tau)d\delta - \int_0^L \delta\mathcal{R}_{ii}(\delta,\tau)d\delta\right]d\tau dt' \tag{4.31}$$

and rearranging slightly yields

$$\overline{x_ix_i} = \overline{u_iu_i}\frac{4}{L^2}\int_0^t\int_0^{t'}\int_0^L (L-\delta)\mathcal{R}_{ii}(\delta,\tau)d\delta d\tau dt' \tag{4.32}$$

The last three steps are repeated for the temporal integrals to arrive at our final result of

$$\overline{x_ix_i} = \overline{u_iu_i}\frac{4t}{L}\int_0^t\int_0^L (1-\tau/t)(1-\delta/L)\mathcal{R}_{ii}(\delta,\tau)d\delta d\tau \tag{4.33}$$

Following the above procedure, it is relatively straightforward to show that the magnitude of the velocity fluctuations of the fibre is given by

$$\overline{v_i v_i} = \overline{u_i u_i} \frac{2}{L} \int_0^L (1 - \delta/L) \mathcal{R}_{ii}(\delta) d\delta \tag{4.34}$$

This equation shows that the magnitude of the fluctuations of the fibre will be less than the fluid fluctuations, by an amount dependent on the spatial velocity correlation.

Rotational Dispersion

The rotational dispersion of the fibre is calculated following the same procedure as the translational dispersion. From Equation 4.20 the fluctuating component of the rotational velocity is given by

$$\dot{p}_i = \frac{12}{L^3} \int_{-L/2}^{L/2} l u_i(l) dl \tag{4.35}$$

The mean square of the rotational velocity is

$$\overline{\dot{p}_i \dot{p}_j} = \overline{\frac{12}{L^3} \int_{-L/2}^{L/2} l u_i(l) dl \frac{12}{L^3} \int_{-L/2}^{L/2} l u_j(l) dl} \tag{4.36}$$

or

$$\overline{\dot{p}_i \dot{p}_j} = \frac{144}{L^6} \int_{-L/2}^{L/2} \int_{-L/2}^{L/2} l l' \overline{u_i(l) u_j(l')} dl' dl \tag{4.37}$$

As before, the integrand is symmetric over the area of integration defined by the square $[-L/2, L/2]$ and $[-L/2, L/2]$. Therefore, the integration over the square is equivalent to twice the integration over a triangle, *i.e.*

$$\overline{\dot{p}_i \dot{p}_i} = \frac{288}{L^6} \int_{-L/2}^{L/2} \int_{-L/2}^{l} l l' \overline{u_i(l) u_i(l')} dl' dl \tag{4.38}$$

The same change of variables, $l' = l + \delta$, is introduced and

$$\overline{\dot{p}_i\dot{p}_i} = \frac{288}{L^6}\int_{-L/2}^{L/2}\int_{-(l+L/2)}^{0} l(l+\delta)\overline{u_i(l)u_i(l+\delta)}d\delta dl \tag{4.39}$$

The velocity correlation, $\mathcal{R}$, is again defined as

$$\frac{\overline{u_i(l)u_i(l+\delta)}}{\overline{u_iu_i}} = \mathcal{R}_{ii}(\delta) \tag{4.40}$$

substituting for the the correlation function results in

$$\overline{\dot{p}_i\dot{p}_i} = \overline{u_iu_i}\frac{288}{L^6}\int_{-L/2}^{L/2}\int_{-(l+L/2)}^{0} l(l+\delta)\mathcal{R}_{ii}(\delta)d\delta dl \tag{4.41}$$

Integrating by parts,

$$\begin{aligned}\overline{\dot{p}_i\dot{p}_i} &= \overline{u_iu_i}\frac{288}{L^6}\left\{\frac{l^3}{3}\int_{-(l+L/2)}^{0}\mathcal{R}_{ii}(\delta)d\delta\Big|_{-L/2}^{L/2} - \int_{-L/2}^{L/2}\frac{l^3}{3}\mathcal{R}_{ii}(-(l+L/2))dl\right.\\ &\left. + \frac{l^2}{2}\int_{-(l+L/2)}^{0}\delta\mathcal{R}_{ii}(\delta)d\delta\Big|_{-L/2}^{L/2} - \int_{-L/2}^{L/2}\frac{l^2}{2}(-(l+L/2))\mathcal{R}_{ii}(-(l+L/2))dl\right\}\end{aligned} \tag{4.42}$$

Simplifying,

$$\begin{aligned}\overline{\dot{p}_i\dot{p}_i} &= \overline{u_iu_i}\frac{288}{L^6}\left\{\frac{(L/2)^3}{3}\int_{-L}^{0}\mathcal{R}_{ii}(\delta)d\delta - \int_{-L/2}^{L/2}\frac{l^3}{3}\mathcal{R}_{ii}(-(l+L/2))dl\right.\\ &\left. + \frac{(L/2)^2}{2}\int_{-L}^{0}\delta\mathcal{R}_{ii}(\delta)d\delta + \int_{-L/2}^{L/2}\frac{l^2}{2}(l+L/2)\mathcal{R}_{ii}(-(l+L/2))dl\right\}\end{aligned} \tag{4.43}$$

Using a change of variables again, $\gamma = -(l+L/2)$, and simplifying some of the above terms yields

$$\begin{aligned}\overline{\dot{p}_i\dot{p}_i} &= \frac{288}{L^6}\left\{\frac{L^3}{24}\int_{-L}^{0}\mathcal{R}_{ii}(\delta)d\delta - \int_{0}^{-L}\frac{(-\gamma-L/2)^3}{3}\mathcal{R}_{ii}(\gamma)d\gamma\right.\\ &\left. + \frac{L^2}{8}\int_{-L}^{0}\delta\mathcal{R}_{ii}(\delta)d\delta + \int_{0}^{-L}\frac{(-\gamma-L/2)^2}{2}\gamma\mathcal{R}_{ii}(\gamma)d\gamma\right\}\end{aligned} \tag{4.44}$$

Simplifying further results in

$$\overline{\dot{p}_i\dot{p}_i} = \overline{u_iu_i}\frac{288}{L^6}\int_{0}^{-L}\left(-\frac{L^3}{24} + \frac{(-\delta-L/2)^3}{3} - \frac{L^2}{8}\delta + \frac{(-\delta-L/2)^2}{2}\delta\right)\mathcal{R}_{ii}(\delta)d\delta \tag{4.45}$$

and simplifying again, gives the following result for the mean square fluctuating angular velocity:

$$\overline{\dot{p}_i\dot{p}_i} = \overline{u_iu_i}\frac{24}{L^3}\int_0^L \left(1 - 3\frac{\delta}{L} + 2\left(\frac{\delta}{L}\right)^3\right)\mathcal{R}_{ii}(\delta)d\delta \tag{4.46}$$

carrying out the time integrals as before the orientation dispersion is

$$\overline{p_ip_i} = \overline{u_iu_i}\frac{24}{L^3}\int_0^t\int_0^L 2(t-\tau)\left(1 - 3\frac{\delta}{L} + 2\left(\frac{\delta}{L}\right)^3\right)\mathcal{R}_{ii}(\delta,\tau)d\delta d\tau \tag{4.47}$$

Dispersion coefficient

Particle transport by turbulent dispersion is often approximated as a gradient driven process with the mean flux of a fluctuating quantity related to the gradient of the mean quantity by a dispersion coefficient. The dispersion coefficient for both fibre translation and orientation is related to the mean square displacements, derived in the previous section, following the analysis of Hinze [74].

Here we show the derivation of the translational dispersion coefficient. Assuming the concentration of fibres, C, has a mean, $\bar{C}$ and fluctuating component, c, that is, $C = \bar{C} + c$, and the particles have a fluctuating velocity, v, the concentration flux, $\mathcal{F}$, due to the turbulent fluctuations is given by

$$\mathcal{F} = \overline{vc} \tag{4.48}$$

The fluctuating component of concentration is approximately related to the mean gradient of the concentration by

$$c = -x\frac{d\bar{C}}{dx} \tag{4.49}$$

where x is the displacement of the particles during a fluctuation. The velocity of the particle is then the time derivative of the displacement, *i.e.*,

$$v = \frac{dx}{dt} \tag{4.50}$$

Therefore, the average particle flux, $\mathcal{F}$, is given as

$$\mathcal{F} = -\overline{x\frac{d\bar{C}}{dx}\frac{dx}{dt}} \tag{4.51}$$

which is equal to

$$\mathcal{F} = -\frac{1}{2}\frac{d\overline{x^2}}{dt}\frac{d\bar{C}}{dx} \tag{4.52}$$

By definition, the flux is proportional to the concentration gradient multiplied by the dispersion coefficient, *i.e.*,

$$\mathcal{F} = -D_t\frac{d\bar{C}}{dx} \tag{4.53}$$

Thus,

$$D_t = \frac{1}{2}\frac{d\overline{x^2}}{dt} \tag{4.54}$$

Although the dispersion coefficient, D_t, is properly defined as a tensor, here isotropy is assumed and it is defined as a scalar property. Substituting Equation 4.33 into Equation 4.54, results in

$$D_t = \frac{1}{2}\frac{d}{dt}\left(\overline{u^2}\frac{4}{L^2}\int_0^t\int_0^L (t-\tau)(L-\delta)\mathcal{R}(\delta,\tau)d\delta d\tau\right) \tag{4.55}$$

By replacing concentration with the orientation distribution function, and the velocity of the fibre with the rotational velocity, the orientation dispersion coefficient, D_p, is derived in exactly the same fashion, and is given given by

$$D_p = \frac{1}{2}\frac{d\overline{p^2}}{dt} \tag{4.56}$$

Substituting Equation 4.47 into the above yields

$$D_p = \frac{1}{2}\frac{d}{dt}\left(\overline{u^2}\frac{24}{L^3}\int_0^t\int_0^L 2(t-\tau)\left(1-3\frac{\delta}{L}+2\left(\frac{\delta}{L}\right)^3\right)\mathcal{R}(\delta,\tau)d\delta d\tau\right) \tag{4.57}$$

4.3 Discussion

The mean and fluctuating equations of turbulent fibre motion are examined separately and compared with previous work.

4.3.1 Mean Motion

In the limit as fibre length decreases to zero ($L \to 0$), the equation of fibre translation (Equation 4.19) is identical to the fluid's, i.e.,

$$\bar{V} = \bar{U} \tag{4.58}$$

Thus, short fibres act as tracer particles and follow the streamlines. Also, fibre centres of any length will follow the fluid's streamlines in a linear shear field.

In linear shear, the equation of rotation, given by Equation 4.20, is identical to Jeffery's equation of rotation in the limit as aspect ratio goes to infinity. This can be easily shown in two dimensions. A general flow field with linear velocity gradients is given by

$$U_i = U_i|_0 + \left.\frac{\partial U_i}{\partial \xi_j}\right|_0 \xi_j \tag{4.59}$$

In a plane, $\xi_1 = l\cos\theta$ and $\xi_2 = l\sin\theta$, where θ is the angle of the fibre with respect to the ξ_1 axis. Substituting this into Equation 4.20 and integrating yields

$$\dot{\theta} = \frac{1}{2}\sin(2\theta)\left(\frac{\partial U_2}{\partial \xi_2} - \frac{\partial U_1}{\partial \xi_1}\right) + \cos^2(\theta)\frac{\partial U_2}{\partial \xi_1} - \sin^2(\theta)\frac{\partial U_1}{\partial \xi_2} \tag{4.60}$$

By inspection we see that this equation is identical to Jeffery's equation of rotation, given by Equation 2.1, in the limit as $\alpha \to \infty$.

The difference between the two theoretical expressions for rotational velocity (Equations 2.1 and 4.60) for a finite value of α is that Cox's [61] first order approximation neglects the moment over the fibre width. Cox states that third order terms in his expansion are required before any moment from the fibre width is retained; however, these

third order terms are not given in his analysis. The result of using Cox's first order approximation is that fibres no longer rotate in classical orbits, but rotate until the fibre is parallel to the fluid streamlines, at which point the rotational velocity becomes zero. The advantage of Equation 4.20, over the corresponding equation of Jeffery's is that the former is generalized to velocity fields that are nonlinear over the length of the fibre.

The equations derived here are for straight fibres, but the derivation could be easily extended to include fibres with a curved shape. Pulp fibres are never straight, having a broad range of shapes [101]. These equations are also valid only for rigid fibres that do not bend, where stiff is defined by a fibre bending number less than ten [102].

4.3.2 Turbulent Motion

To illustrate the theoretically-predicted effect of length on fibre dispersion in Equations 4.33 and 4.47, the particle's Lagrangian correlation function must be known. This is discussed below, followed by a discussion of dispersion in the limit of short fibres and the effect of fibre length when it is comparable to the length scale of turbulence.

Lagrangian particle velocity correlation

As with the problem of Taylor's [68] closure assumptions, our derivation is in terms of the unknown Lagrangian particle velocity correlation. In the following discussion the turbulent fluid velocity field is described by a number of correlations. The Lagrangian fluid velocity correlation refers to the correlation of the fluid velocity fluctuations following the path of a fluid element. The Lagrangian particle velocity correlation refers to the correlation of the fluid's velocity fluctuations following the path of a particle. It is well known, experimentally [73] and theoretically [83], that particle inertia and external forces affect the Lagrangian particle velocity correlation function.

The Lagrangian particle velocity correlation will be a function of fibre length. In the limit as fibre length approaches zero, the fibre follows the fluid exactly. Here the equation of translational dispersion is identical to that proposed by Taylor [68], and the Lagrangian particle velocity correlation is identical to the Lagrangian fluid velocity correlation. As fibre length increases, the fibre extends further through the fluid and the fluctuations along the length of the fibre begin to cancel each other. This results in the fibre's fluctuations becoming increasingly damped. In the limit of an infinitely long fibre, all the fibre fluctuations are damped out and fibre motion is governed by the mean fluid motion. If the particle follows the mean fluid velocity exactly, the Lagrangian particle velocity correlation is the same as the fluid's Eulerian velocity correlation. For the intermediate case, the Lagrangian particle correlation will be between the Lagrangian and Eulerian correlation of the fluid. This is similar to the transition from Lagrangian to Eulerian correlations for particles as a function of increasing particle inertia [87, 84].

In this work, we want to relate fibre dispersion to the time and spatial scales of turbulence. To do so, we refer to the Lagrangian particle integral time scale, $\mathcal{T}$, realizing it is bracketed between the Lagrangian fluid integral time scale for short fibres, and the Eulerian integral time scale in the limit of very long fibres. If the turbulence is ergodic and the fibres are randomly oriented and positioned in the fluid, then averaging the velocity along the length of a fibre, over an ensemble of fibres, results in the fluid's spatial Eulerian velocity correlation. Therefore, the velocity correlation along the length of the fibre is approximated as the fluid Eulerian spatial velocity correlation, with the corresponding Eulerian integral length scale.

Short fibre dispersion

The Lagrangian particle correlation function is approximated assuming that the spatial correlation function and the temporal correlation function are statistically independent

functions. This simplification enables the combined spatial and temporal correlation to be expressed as

$$\mathcal{R}(\delta,\tau) = \mathcal{R}_\delta(\delta)\mathcal{R}_\tau(\tau) \tag{4.61}$$

where $\mathcal{R}_\delta(\delta)$ is approximately the same as the fluid's Eulerian velocity correlation and $\mathcal{R}_\tau(\tau)$ is the particle's Lagrangian temporal velocity correlation. Using this simplification we estimate the translational and orientational dispersion of fibres with lengths less than the scale of turbulence. Taking the limit as $L \to 0$, Equation 4.33 yields

$$\overline{x^2} = 2\overline{u^2}\int_0^t (t-\tau)\mathcal{R}(\tau)d\tau \tag{4.62}$$

which is identical to the expression given by Taylor for dispersion of a passive scalar. For infinitely small particles, it is also assumed that the particle's temporal Lagrangian velocity correlation is the same as the fluid's. At long times, as t gets large with respect to the Lagrangian time scale (*i.e.* $t \to \infty$), the above expression becomes

$$\overline{x^2} = 2\overline{u^2}\mathcal{T}t \tag{4.63}$$

where $\mathcal{T}$ is the integral time scale. Substituting the above into the equation for the translational dispersion coefficient, Equation 4.54, results in the classical Taylor dispersion coefficient

$$D_t = \overline{u^2}\mathcal{T} \tag{4.64}$$

The orientation dispersion in the limit as L goes to zero is calculated by first taking a Taylor series expansion of the correlation coefficient, with respect to its spatial variable, *i.e.*,

$$\mathcal{R}(\delta) = 1 + \frac{1}{2}\frac{d^2\mathcal{R}(\delta)}{d^2\delta}\bigg|_{\delta=0}\delta^2 + \ldots \tag{4.65}$$

where

$$-\frac{1}{2}\frac{d^2\mathcal{R}(\delta)}{d^2\delta} = \frac{1}{\lambda^2} \tag{4.66}$$

and λ is the Taylor micro-length scale, or dissipation scale, of the turbulence, which represents the average dimension of the smallest eddies [74]. This series expansion is then substituted into Equation 4.47, and taking the limit as $L \to 0$ results in the following expression for the dispersion of small fibres as a function of time:

$$\overline{p^2} = 2\frac{\overline{u^2}}{\lambda^2}\int_0^t 2(t-\tau)\mathcal{R}(\tau)d\tau \tag{4.67}$$

The long time dispersion ($t \to \infty$) is then

$$\overline{p^2} = 4\frac{\overline{u^2}}{\lambda^2}\mathcal{T}t \tag{4.68}$$

Substituting the above into the equation for the orientation dispersion coefficient, Equation 4.56, results in the following expression

$$D_p = 2\frac{\overline{u^2}}{\lambda^2}\mathcal{T} \tag{4.69}$$

It is interesting to note that the same relation for the orientation dispersion coefficient of a zero length fibre can be derived in a simpler fashion, which may provide more insight into the mechanisms of orientation dispersion of a small fibre than the previous derivation. The orientation dispersion is assumed to be equal to the mean square rotational velocity fluctuation multiplied by the integral time scale, *i.e.*

$$D_p = \overline{\dot{p}^2}\mathcal{T} \tag{4.70}$$

which is analogous to the translational dispersion coefficient given in Equation 4.64. The rotational velocity, $\dot{p}$, is calculated assuming the fluctuating fluid velocity is constant over the length of the fibre. This is true as fibre length becomes small with respect to the

smallest eddies in the flow. Taking a Taylor series expansion of the local fluid velocity, the fibre's rotational velocity, given by Equation 4.35, becomes

$$\dot{p} = \frac{12}{L^3} \int_{-L/2}^{L/2} l \left(u(0) + \left. \frac{du}{dl} \right|_{l=0} l + \frac{1}{2} \left. \frac{d^2u}{dl^2} \right|_{l=0} l^2 + ... \right) dl \tag{4.71}$$

Taking the limit as L goes to zero of Equation 4.71, we see that the fibre's rotational velocity is equal to the local fluid velocity gradient, *i.e.*

$$\dot{p} = \frac{du}{dl} \tag{4.72}$$

The average square rotational velocity is then given by

$$\overline{\dot{p}^2} = \overline{\left(\frac{du}{dl} \right)^2} \tag{4.73}$$

where [74]

$$\overline{\left(\frac{du}{dl} \right)^2} = \frac{2\overline{u^2}}{\lambda^2} \tag{4.74}$$

Substituting this result into Equation 4.70 yields exactly the same rotational dispersion coefficient as in Equation 4.69.

We can also show that the rotational dispersion of fibres, given by Equation 4.69, is the same as that given by the dimensional analysis of Krushkal and Gallily [94] (Eq. 2.8). The total kinetic energy dissipation is given by

$$\epsilon = 15\nu \frac{\overline{u^2}}{\lambda^2} \tag{4.75}$$

or

$$\frac{\epsilon}{\nu} \propto \frac{\overline{u^2}}{\lambda^2} \tag{4.76}$$

where ν is the kinematic viscosity. Assuming that

$$\mathcal{T} \propto \frac{\lambda}{\sqrt{\overline{u^2}}} \tag{4.77}$$

and substituting Equations 4.76 and 4.77 into the expression for the rotational dispersion coefficient, Equation 4.69, yields

$$D_p \propto (\epsilon/\nu)^{1/2} \tag{4.78}$$

which is identical to the result obtained by Krushkal and Gallily (Equation 2.8).

Longer fibre dispersion

As fibre length increases, the velocity fluctuations and dispersion are diminished. To illustrate the effect of fibre length on fibre dispersion an approximate equation for the velocity correlation, $\mathcal{R}(\delta, \tau)$, is substituted into Equations 4.33 and 4.47 and integrated to obtain dispersion as a function of time.

The temporal correlation is approximated by a negative exponential function which has been shown to reasonably reflect experimental data [81, 68, 74]. The spatial correlation is approximated by a Gaussian function, also used as a model velocity correlation [74]. The Gaussian function is chosen as a model over the exponential function, for the spatial correlation, because it is symmetric, with a zero first derivative at $\delta = 0$. A correlation function with a non-zero first derivative at the origin would mistakenly lead to an infinite orientation dispersion in the limit as fibre length goes to zero.

The spatial and temporal correlations are given as functions of their integral length and time scales, Λ and $\mathcal{T}$, respectively, by

$$\mathcal{R}_\delta(\delta) = \exp(\frac{-\pi\delta^2}{4\Lambda^2}) \tag{4.79}$$

and

$$\mathcal{R}_\tau(\tau) = \exp(\frac{-\tau}{\mathcal{T}}) \tag{4.80}$$

Using these model equations the translational and orientation dispersion as a function

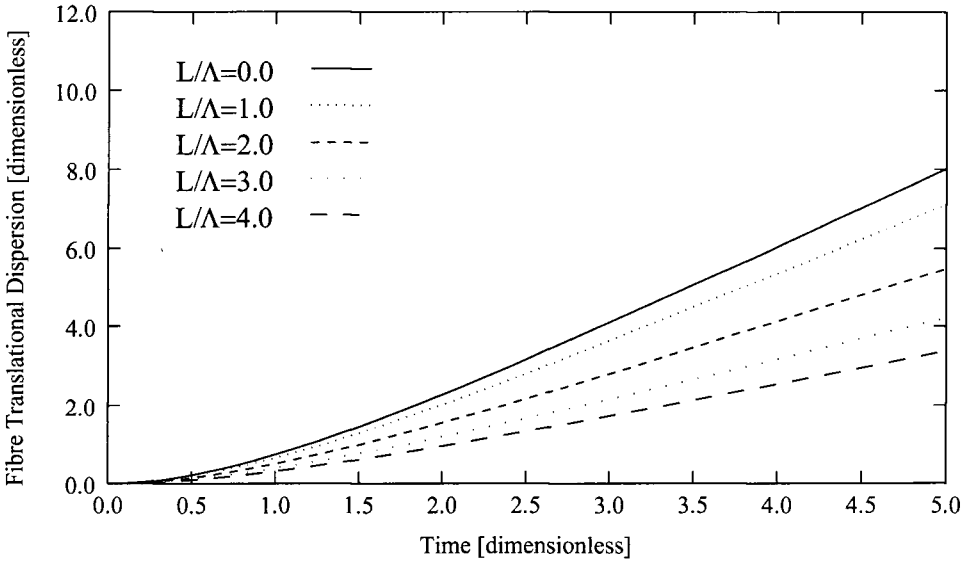

Figure 4.7: The dimensionless dispersion, $\frac{\overline{x^2}}{\overline{u^2}\mathcal{T}^2}$, plotted against dimensionless time, $t/\mathcal{T}$, for several values of dimensionless fibre length, L/Λ equal to 0, 1.0, 2.0, 3.0 and 4.0.

of length and time are given as

$$\overline{x^2} = 4\overline{u^2}\mathcal{T}^2\frac{\Lambda}{L}\left(\mathrm{erf}(\frac{\pi^{1/2}L}{2\Lambda}) + \frac{2}{\pi}\frac{\Lambda}{L}\left(e^{-\frac{\pi L^2}{4\Lambda^2}} - 1\right)\right)\left(\frac{t}{\mathcal{T}} + e^{-t/\mathcal{T}} - 1\right) \tag{4.81}$$

and

$$\overline{p^2} = 48\overline{u^2}\frac{\mathcal{T}^2}{L^2}\frac{\Lambda}{L}\left(\mathrm{erf}(\frac{\pi^{1/2}L}{2\Lambda}) + \frac{16}{\pi^2}\left(\frac{\Lambda}{L}\right)^3\left(1 - e^{-\frac{\pi L^2}{4\Lambda^2}}\right) + \frac{2}{\pi}\frac{\Lambda}{L}\left(e^{-\frac{\pi L^2}{4\Lambda^2}} - 3\right)\right)\left(\frac{t}{\mathcal{T}} + e^{-t/\mathcal{T}} - 1\right) \tag{4.82}$$

The expression for the translational dispersion (Equation 4.81) is plotted in Figure 4.7 for several values of L/Λ equal to 0.0, 1.0, 2.0, 3.0 and 4.0. From this plot, it is evident that the effect of fibre length on dispersion can be considerable.

The length dependence on dispersion is best illustrated by the the long time translation and orientation dispersion coefficients, given by

$$D_t = 2\overline{u^2}\mathcal{T}\frac{\Lambda}{L}\left(\mathrm{erf}(\frac{\pi^{1/2}L}{2\Lambda}) + \frac{2}{\pi}\frac{\Lambda}{L}\left(e^{-\frac{\pi L^2}{4\Lambda^2}} - 1\right)\right) \tag{4.83}$$

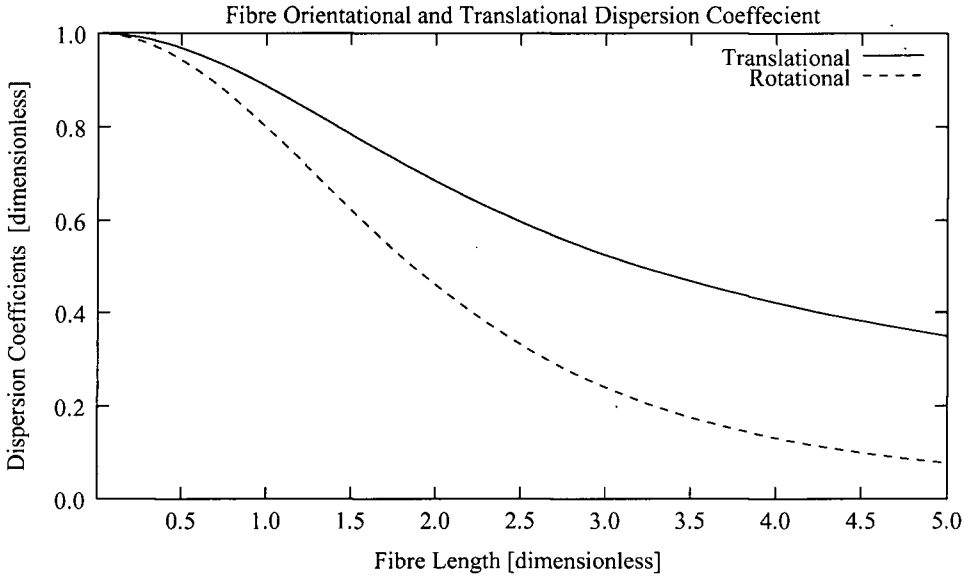

Figure 4.8: The dimensionless dispersion coefficients, $D_x(L)/D_x(0)$, as a function of fibre length normalized by the integral length scale, L/Λ.

and

$$D_p = 24\overline{u^2}\frac{\mathcal{T}}{L^2}\frac{\Lambda}{L}\left(\mathrm{erf}(\frac{\pi^{1/2}L}{2\Lambda}) + \frac{16}{\pi^2}\left(\frac{\Lambda}{L}\right)^3\left(1 - e^{-\frac{\pi L^2}{4\Lambda^2}}\right) + \frac{2}{\pi}\frac{\Lambda}{L}\left(e^{-\frac{\pi L^2}{4\Lambda^2}} - 3\right)\right) \qquad (4.84)$$

The dispersion coefficients are normalized by the dispersion of a zero length fibre and plotted as a function of L/Λ in Figure 4.8. From this figure it is evident that fibre dispersion is dramatically damped as fibre length increases beyond the integral length scale of the turbulence. The effect of length is more pronounced for rotational dispersion, with the long time dispersion coefficient reduced to less than 10% of a zero length fibre, at $L = 5\Lambda$.

The dissipation scale, λ, of the model spatial correlation function used to calculate the long time dispersion coefficients is related to the integral length scale by $\lambda = 2\Lambda/\sqrt{\pi}$. This is unusual, in that, the dissipation scale is greater than the integral length scale. This is not the case, and is an artifact of the model correlation function. A smaller dissipation scale with respect to the integral length scale would result in a greater dampening of the

orientation dispersion coefficient, relative to the translational dispersion coefficient, than is indicated in Figure 4.8.

4.4 Summary

In this chapter, we have theoretically investigated the behavior of fibres in turbulent flow. The effect of fibre length on the mean and fluctuating equations of motion of a fibre flowing in a turbulent fluid was derived. The derivation assumed that the fibres are straight, rigid, inertialess and have infinetesimal diameters. We also assumed that the force on the fibre is proportional to the relative motion between the fibre and fluid (*i.e.* a Stokes drag force). The equations of turbulent dispersion were expressed in terms of the fibre's Lagrangian velocity correlation, assuming the rotational and translational fibre motions to be independent and the longitudinal and transverse fluid velocity correlations to be equivalent.

These assumptions result in simple compact expressions for the mean motion, (Equations 4.19 and 4.20) and the fluctuating motion (Equations 4.34 and 4.46) of the fibre. For the simplifications used the mean fibre velocity was the average of the mean fluid velocity field taken over the length of the fibre. The fibre's mean rotational velocity was, similarly, the first moment of the mean fluid velocity taken over the length of the fibre. In the limit, as fibre length goes to zero, the translational dispersion was equivalent to that derived by Taylor [68] and the orientational dispersion coefficient is equivalent to that derived by dimensional analysis. We also derived expressions for fibre dispersion coefficients as a function of the ratio of fibre length to the fluid's integral length scale and demonstrated how fibre fluctuations, leading to dispersion, are significantly damped for $L/\Lambda > 1$.

This fundamental analysis provides a conceptual framework for investigating the motion of fibres in a turbulent fluid, and forms the basis for the trajectory calculations for fibres approaching an aperture entry given in the next chapter.

4.5 Nomenclature

Table 4.3: The following nomenclature was used in this section.

$\vec{f}$	Force per unit length along fibre.
Re	Reynolds number based on fibre diameter.
D	Stokes drag tensor.
$\vec{U}$, U_i	Fluid velocity, $\vec{U} = \bar{\vec{U}} + \vec{u}$.
$\bar{\vec{U}}$, $\bar{U}_i$	Mean component of fluid velocity.
$\vec{u}$, u_i	Fluctuating component of fluid velocity.
$\vec{\mathbf{V}}$	Velocity of a point along fibre length, $\vec{\mathbf{V}} = \vec{V} + l\dot{\vec{\mathbf{p}}}$.
$\vec{V}$, V_i	Velocity of fibre centre, $V_i = \bar{V}_i + v_i$.
$\bar{\vec{V}}$, $\bar{V}_i$	Mean velocity of fibre centre.
$\vec{v}$, v_i, v	Fluctuating component of fibre centre velocity.
l, l', δ	Position along the fibre's major axis.
$\vec{\mathbf{p}}$	Fibre orientation vector; a unit vector parallel to fibre's major axis. $\vec{\mathbf{p}} = \bar{\vec{p}} + \vec{p}$.
$\bar{\vec{p}}$, $\bar{p}_i$	Mean fibre orientation vector.
$\vec{p}$, p_i	Fluctuating component of fibre orientation vector.
$\dot{\vec{\mathbf{p}}}$	Fibre rotational vector; time derivative of the fibre orientation vector, $\dot{\vec{\mathbf{p}}} = \dot{\bar{\vec{p}}} + \dot{\vec{p}}$.
$\dot{\bar{\vec{p}}}$, $\dot{\bar{p}}_i$	Mean fibre rotational vector.
$\dot{\vec{p}}$, $\dot{p}_i$	Fluctuating component of rotational vector.
L	Fibre length.
$\vec{F}$	Net external force on the fibre.
$\vec{M}$	Net external moment on the fibre.
t, t', τ	Time.
$\mathcal{R}$, $\mathcal{R}_{ij}$	Lagrangian particle spatial and temporal velocity correlation.
$\mathcal{R}_\delta$	Lagrangian particle spatial velocity correlation.
$\mathcal{R}_\tau$	Lagrangian particle temporal velocity correlation.
x_i, x	Position of fibre centre.
ξ, ξ_1, ξ_2	Cartesian coordinates.

C	Concentration of fibre centres.
$\bar{C}$	Mean concentration of fibre centres.
c	Fluctuating component of fibre center concentration.
$\mathcal{F}$	Fibre centre concentration flux.
D_t	Fibre translational dispersion coefficient.
D_p	Fibre orientational dispersion coefficient.
D_x	Translational or rotational dispersion coefficient.
α	Aspect ratio of particle.
θ	Angle of the major axis of the fibre with respect to the ξ_1 axis.
$\mathcal{T}$	Lagrangian particle integral time scale.
Λ	Lagrangian particle Taylor micro length scale.
λ	Lagrangian particle integral length scale.
ϵ	Turbulent kinetic energy dissipation.
ν	Kinematic viscosity.

Chapter 5

THEORETICAL PREDICTIONS OF FIBRE PASSAGE

5.1 Introduction

The probability of a fibre passing through an aperture is dependent on the fibre's initial position and orientation, and on the resulting trajectory during flow near the aperture. However, fibre trajectories near a narrow aperture are complex. The flow field surrounding the aperture is a turbulent bifurcating flow. The fibres passing through the aperture are long with respect to the scale of the flow; therefore, the fluid velocity can change significantly over the length of the fibre. As well, fibres can impact in a complicated manner on the edges of the aperture during their movement near the aperture.

Some of the mechanisms governing fibre passage through this complicated system have been demonstrated through high speed cinematographic studies by Gooding and Kerekes [7, 43] and by Yu [41]. These studies have provided some insight into the mechanisms of fibre passage, but have been limited to long, shive-like fibres in the case of Gooding, and to only a few trajectories in the case of Yu. From these studies, it is postulated that one mechanism of fibre separation at a narrow aperture is a "turning effect" [7], in which fibre rotation to enter an aperture from an orientation parallel to the plane containing the aperture plays a role in fibre passage through the aperture. Tangsaghasaksri [35], studied fibre trajectories approaching an aperture using computational fluid dynamics and the same mean equations of fibre motion derived in Chapter 4. However, the trajectories were only calculated to the point of impact, and not used to determine whether passage

took place.

In this chapter we develop a numerical model which predicts the trajectory of a fibre in the entry flow of an aperture. The model accounts for impacts with the walls of the channel and aperture and is able to predict passage through the aperture. The model uses the equations of mean fibre motion developed in Chapter 4 and similarly derived equations to account for fibre impacts with the wall. The equations are integrated numerically through a computationally-derived flow field. If, during a trajectory, a fibre impact occurs with a solid surface, the reaction force of the wall is considered in the force balance. This allows the complete fibre trajectory during passage to be calculated. From this simulation, we estimate the probability of passage function.

5.2 Equations of Fibre Motion

During passage, fibres come into contact with the walls of the aperture. The resulting reaction force must be modeled in the force balance. However, to completely model all aspects of the motion of flexible fibres in a turbulent fluid during passage with wall contacts is extremely complex, and beyond the scope of this work. For this reason our approach requires a number of necessary simplifications, based on the following assumptions:

- The computational fluid dynamic (CFD) solution of the flow field accurately represents the actual velocity field.
- The fibres are sufficiently rigid to not bend during their trajectories and impacts with the slot.
- The fibres are inertialess (fibre density is approximately the same as water).
- The force on the fibre depends linearly on the relative velocity between the fibre and the fluid, and the drag tensor, D, is approximately equal to Cox's [61] first

order approximation, *i.e.* $D = \vec{\mathbf{p}}\vec{\mathbf{p}} - 2I$.

- The fibre's motion is predominantly planar (two-dimensional).
- The friction force at a fibre-wall contact is proportional to the normal force.
- The presence of the fibre does not influence the fluid flow field.
- Fibre concentrations are sufficiently dilute that there are no fibre-fibre interactions.

We first examine the effect of fluid turbulent velocity on fibre motion. In turbulent pipe flow the turbulent velocity fluctuations range from approximately 4-8% of the local mean flow near the pipe wall [74]. The turbulent integral length scale is assumed to be proportional to the distance away from the wall, *i.e.* $\Lambda \approx \kappa y$, until becoming constant at 10-15% of the channel width for the transverse integral length scale, and up to 40% of the channel width for the longitudinal integral length scale [74]. The turbulence in this region is not isotropic, with eddies extending in the direction of flow. In this application the channel width is approximately 20mm; thus, in the core flow the smallest integral length scale is approximately 2mm, which is the average fibre length used in this study.

From the theory presented in Chapter 4, the approximate contribution of the turbulence on the mean fibre motion can be estimated. The mean velocity of the fibre (Equation 4.19) is equal to the mean fluid velocity averaged over the length of the fibre. Therefore, the mean fibre velocity is approximately the same as the mean fluid velocity. The additional velocity due to the turbulence is approximately given by

$$(\overline{v^2})^{1/2} = \left(\frac{2\overline{u^2}}{L} \int_0^L (1 - \delta/L)\mathcal{R}(\delta) d\delta \right)^{\frac{1}{2}} \tag{5.85}$$

Assuming for turbulent duct flow $(\overline{u^2})^{1/2}$ is approximately 5% of the local mean fluid velocity, $\mathcal{R}(\delta) \approx e^{\delta/\Lambda}$ and the integral length scale, Λ, is approximately equal to fibre length, L, results in $(\overline{v^2})^{1/2} \approx 0.0425$ of the mean fluid velocity. Thus, during a single

eddy interaction, the fibre velocity will only deviate from the mean fibre velocity by approximately 4.25%. Therefore we may neglect the influence of fluctuating turbulent components of fluid velocity on the fibre trajectory in this case.

Using these simplifications, the equations of fibre motion in a free flow and during impact with the aperture wall were derived.

5.2.1 Fibre Motion in a Free Flow

Making the same assumptions used in Chapter 4 the net external force on a fibre is written as

$$\vec{F} = \int_{-\frac{L}{2}}^{\frac{L}{2}} D[\vec{u_f}(l) - (\vec{u}_{cm} + l\dot{\vec{\mathbf{p}}})]dl \tag{5.86}$$

and the net external moment is

$$\vec{M} = \int_{-\frac{L}{2}}^{\frac{L}{2}} l\vec{\mathbf{p}} \times D[\vec{u}_f(l) - (\vec{u}_{cm} + l\dot{\vec{\mathbf{p}}})]dl \tag{5.87}$$

Assuming an inertialess, rigid fibre, the above two equations can be re-written as

$$\vec{u}_{cm} = \frac{1}{L}\int_{-\frac{L}{2}}^{\frac{L}{2}} \vec{u_f}(l)dl \tag{5.88}$$

and

$$\dot{\vec{\mathbf{p}}} = \frac{12}{L^3}\int_{-\frac{L}{2}}^{\frac{L}{2}} l\vec{u}_f(l)dl \tag{5.89}$$

Simplifying the notation for motion in a two-dimensional plane we let U and V represent the x and y components of the fluid velocity and let $\dot{x}_{cm}$ and $\dot{y}_{cm}$ be the x and y components of the fibre centre velocity. The rotational velocity of the fibre is denoted by $\dot{\theta}$. Using this notation the above equations can be re-written as

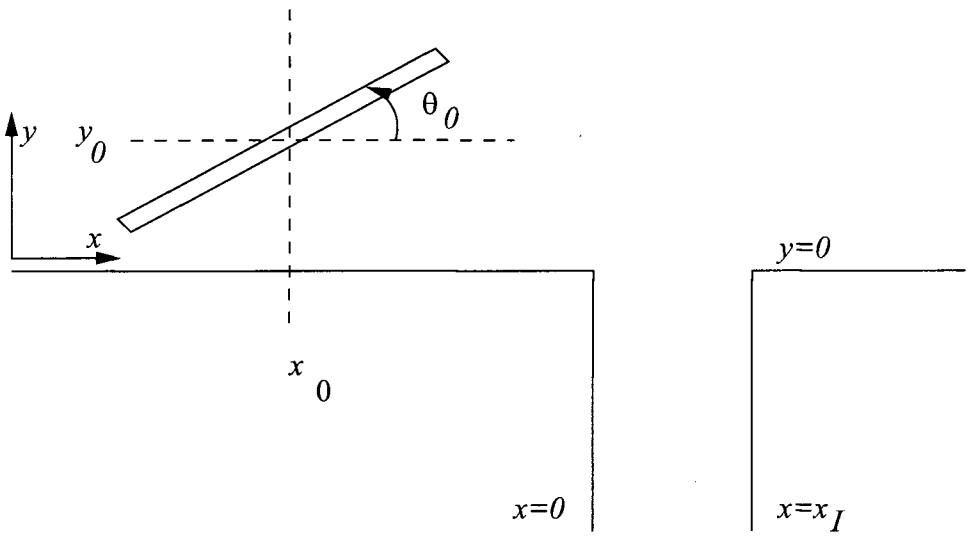

Figure 5.9: A fibre in two dimensions. Initial conditions indicated by x_0, y_0 and θ_0

$$\dot{x}_{cm} = \frac{1}{L}\int_{-\frac{L}{2}}^{\frac{L}{2}} U(l)dl \tag{5.90}$$

$$\dot{y}_{cm} = \frac{1}{L}\int_{-\frac{L}{2}}^{\frac{L}{2}} V(l)dl \tag{5.91}$$

and

$$\dot{\theta} = \frac{12}{L^3}\int_{-\frac{L}{2}}^{\frac{L}{2}} (-U(l)\sin(\theta) + (V(l)\cos(\theta))ldl \tag{5.92}$$

These are the equations of motion for a fibre in the flow field in the absence of contacts with the aperture wall.

5.2.2 Fibre Motion During Contact With the Wall

When a fibre contacts the wall a reaction force is exerted on the fibre. Since the wall is solid we know that the fibre will not pass through the wall. This results in an additional force in the force balance. To account for the reaction force imposed on the fibre by the wall we make two further assumptions. The first is related to the form but not the

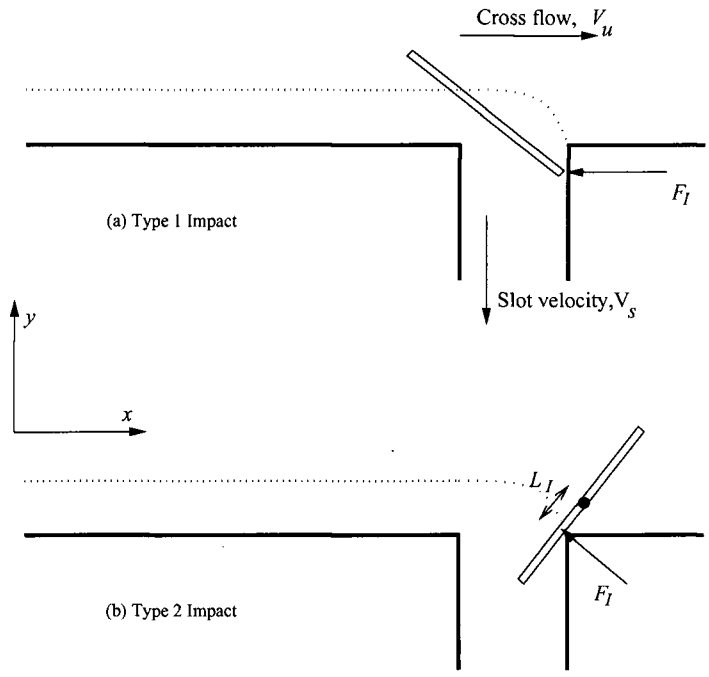

Figure 5.10: Schematic diagram depicting the two types of impacts: a type one impact (a) and a type two impact (b)

magnitude of the drag tensor. The second is that the friction force is proportional to the normal force on the fibre.

Two types of fibre-wall interactions may occur. The first type occurs when one end of a fibre contacts a wall (Figure 5.10a). The second type occurs when the fibre impacts the edge of the aperture somewhere along the length of the fibre (Figure 5.10b). In the first case, in the absence of friction, the wall force is perpendicular to the wall. In the second case, the force is perpendicular to the fibre. In both cases, we call this force $\vec{F}_I$.

The equation of motion is solved by balancing all of the forces on the fibre, subject to the constraint that the fibre is prevented from passing through the wall. During contact, the force and moment equations become

$$\vec{F} = \int_{-\frac{L}{2}}^{\frac{L}{2}} D[\vec{u_f}(l) - (\vec{u}_{cm} + l\dot{\vec{\mathbf{p}}})]dl + \vec{F}_I \tag{5.93}$$

and

$$\vec{M} = \int_{-\frac{L}{2}}^{\frac{L}{2}} l\vec{\mathbf{p}} \times D[\vec{u}_f(l) - (\vec{u}_{cm} + l\dot{\vec{\mathbf{p}}})]dl + L_I\vec{\mathbf{p}} \times \vec{F}_I \tag{5.94}$$

where L_I is the distance from the centre of the fibre to the point of impact. As before, assuming the inertial forces on the fibre are small, these equations are easily re-written in vector form as

$$\vec{u}_{cm} = \frac{1}{L}\left[\int_{-\frac{L}{2}}^{\frac{L}{2}} \vec{u_f}(l)dl + D^{-1}\vec{F}_I\right] \tag{5.95}$$

and

$$\dot{\vec{\mathbf{p}}} = \frac{12}{L^3}\left[\int_{-\frac{L}{2}}^{\frac{L}{2}} l\vec{u}_f(l)dl + D^{-1}L_I\vec{F}_I\right] \tag{5.96}$$

Fibre End Impact (Type 1)

For the type of impact depicted in Fig. 5.10a the point force, $\vec{F}_I$, has two components, a normal force, F_N, perpendicular to the aperture wall and a friction force, μF_N. This allows us to write the $\vec{F}_I$ as the product of an unknown magnitude, F, and a vector given by

$$\vec{F}_I = F\begin{bmatrix} 1 \\ \mu \end{bmatrix} \tag{5.97}$$

To simplify calculations and the resulting equations of motion, we introduce some newly defined variables $\vec{C}$, I_x, I_y and I_m (the letter I refers to integral and should not be confused with moments of inertia). The variable $\vec{C}$ is defined as

$$D^{-1}\vec{F}_I = \begin{bmatrix} C_x \\ C_y \end{bmatrix} F \tag{5.98}$$

where the ratio of C_x to C_y is independent of the magnitude of the drag tensor and is

given by

$$\frac{C_x}{C_y} = \frac{1 + \cos^2(\theta) + \mu\cos(\theta)\sin(\theta)}{\cos(\theta)\sin(\theta) - \mu(\cos^2(\theta) - 2)} \tag{5.99}$$

Also, we define I_x, I_y and I_m as

$$I_x = \int_{-\frac{L}{2}}^{\frac{L}{2}} U(l)dl \tag{5.100}$$

$$I_y = \int_{-\frac{L}{2}}^{\frac{L}{2}} V(l)dl \tag{5.101}$$

and

$$I_m = \int_{-\frac{L}{2}}^{\frac{L}{2}} (-U(l)\sin(\theta) + (V(l)\cos(\theta))ldl \tag{5.102}$$

where U and V are the x and y components of the two dimensional velocity vector, $\vec{u}_f(l)$.

The equations of motion for a fibre during an impact, depicted in Figure 5.10a, are given by

$$\dot{x}_{cm} = \frac{1}{L}(I_x + C_x F) \tag{5.103}$$

$$\dot{y}_{cm} = \frac{1}{L}(I_y + C_y F) \tag{5.104}$$

and

$$\dot{\theta} = \frac{12}{L^3}\left(I_m + L_I(-C_x F\sin(\theta) + C_y F\cos(\theta))\right) \tag{5.105}$$

However, these equations are functions of the unknown magnitude of the wall reaction force, F. To solve for F, we require one more equation. The tip of the fibre does not penetrate into the wall during an impact (Figure 5.10a). This means that the only x-component of velocity of the fibre is that due to rotation about the end of the fibre in contact with the wall. This gives a simple constraint on the equation of motion:

$$\dot{x}_{cm} = L_I\dot{\theta}\sin(\theta) \tag{5.106}$$

where L_I is the distance from the point of impact to the centre of the fibre, which in this case is $\pm L/2$ depending on which end of the fibre impacts with the wall.

The equations of motion, Equations 5.103, 5.104 and 5.105 along with the constraint equation (Equation 5.106) form a readily solvable system of algebraic equations. Solving these for F gives

$$C_x F = \frac{-I_x + \frac{6L_I}{L^2} I_m \sin(\theta)}{1 - 3\sin^2(\theta) + \frac{C_y}{C_x} 3\cos(\theta)\sin(\theta)} \tag{5.107}$$

and $C_y F$ is simply calculated using Equation 5.99.

Fibre Side Impact (Type 2)

The equations of motion during the impact depicted in Figure 5.10b, in which the side of the fibre impacts with the aperture wall, is derived in exactly the same manner as the previous case. All that changes in the analysis is the constraint equation. The form of the contact force and the distance between the point of impact and the fibre centre is given by L_I (see Figure 5.10b). The constraint equation is

$$\dot{y}_{cm} = \dot{x}_{cm}\tan(\theta) + \dot{\theta}(x_{cm} - x_I)(1 + \tan^2(\theta)) \tag{5.108}$$

The equations of motion given by Equations 5.103, 5.104 and 5.105 are still valid and the distance from the centre of the fibre to the point of impact is given by

$$L_I = (x_I - x_{cm})\cos(\theta) + (y_I - y_{cm})\sin(\theta) \tag{5.109}$$

where x_I and y_I are the x and y components of the impact point or slot edge coordinates.

The point force vector is now given as

$$\vec{F}_I = \left(\begin{bmatrix} -\sin(\theta) \\ \cos(\theta) \end{bmatrix} + \mu \begin{bmatrix} \cos(\theta) \\ \sin(\theta) \end{bmatrix} \right) F \tag{5.110}$$

from which we can calculate C_x/C_y, as before, to obtain

$$\frac{C_x}{C_y} = \frac{-\sin(\theta) + 2\mu\cos(\theta)}{\cos(\theta) + 2\mu\sin(\theta)} \tag{5.111}$$

C_yF is now given by

$$C_yF = \frac{I_x\tan(\theta) - I_y + \frac{12I_m(x_{cm}-x_I)(1+\tan^2(\theta))}{L^2}}{(1-\frac{C_x}{C_y}\tan(\theta) - (x_{cm}-x_I)(1+\tan^2(\theta))\frac{12}{L^2}L_I(-\frac{C_x}{C_y}\sin(\theta)+\cos(\theta))} \tag{5.112}$$

C_xF is easy to determine from C_yF using Equation 5.111.

5.3 Application of the Equations of Motion

The motion of individual fibres can be determined by integrating the differential equations of motion through a defined flow field. This was carried out for fibres near apertures, assuming the fibre to be initially free flowing (not impacting with the walls) and with its trajectory governed by Equations 5.90, 5.91 and 5.92. The differential equations were solved using a Runge-Kutta-Fehlberg adaptive integration routine for time, and an adaptive Simpson algorithm [103] was used to determine the spatial integrals along the fibre length. At each time step, it was necessary to determine if the fibre impacts with the boundary and what type of impact occurs. If an impact did occur, the algorithm automatically switched to integrating the equations of motion for an impact (given by Equations 5.103, 5.104 and 5.105).

The numerical computations were solved using a computer program written in C and designed to accept different analytical or computationally generated flow fields.

5.3.1 Impact Types and Impact Switching

At each step of its computed trajectory, the position of a fibre was examined to determine if a fibre has crossed the boundary of the channel or slot. If an impact occurred, then

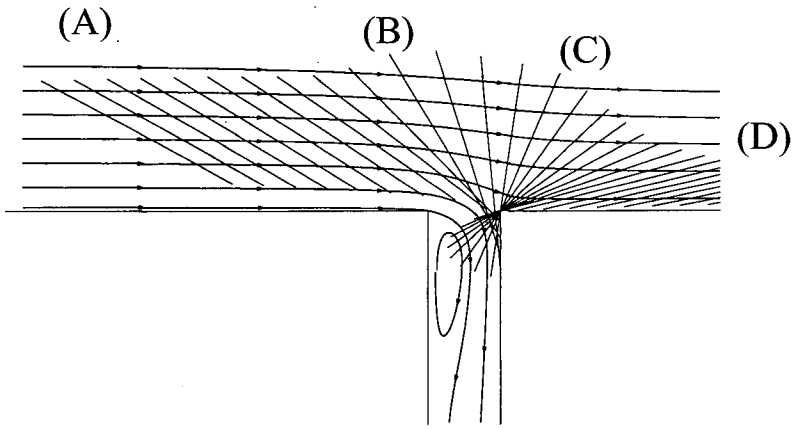

Figure 5.11: Computed trajectory of a fibre with $L/W = 3$, demonstrating how several types of impacts occur during a single trajectory ($V_s = 3.04$m/s). The figure shows the fibre at equal time steps along its trajectory. Initially the fibre is free floating (A), then impacts the downstream edge of the slot on one end (B), then rotates onto the side of the fibre (C) and is subsequently pulled out of the slot to become free floating again (D).

the appropriate contact force was included in the equations of motion.

During a trajectory, a fibre may change its type of wall impact. For example, a fibre end may impact with the downstream edge of the slot, and then be swept downstream by the main channel flow until the fibre impacted the slot edge at some point along its length. The fibre may then be pulled free of the slot (free fibre) and continue moving down the channel (see Figure 5.11).

5.3.2 Stapling

In some cases, fibres become immobilized by wall contact in the slot entry. We defined this as "stapling" of several types:

vertical stapling: Fibre pivots on downstream edge of slot and is held in place by a balance of hydrodynamic forces (see Fig. 5.12).

horizontal stapling: Fibre lies over entry of slot, supported on both ends by the aperture opening (see Fig. 5.13).

wedge stapling: Fibre pivots on downstream edge of slot, held in place by a balance of hydrodynamic forces and force from contact with upstream wall (see Fig. 5.14).

In the program for integrating the trajectories, when horizontal or wedge stapling occurred the simulation simply ended and the result of a stapled fibre was reported. However, vertical stapling was a more complicated case. During vertical stapling, the friction force on the fibre opposed the direction of motion. If this friction force immobilizes the fibre, the fibre rotated around the point of contact. The equation of motion for this case is defined by a simple force balance:

$$\dot{\theta} = \frac{12}{L^3 + 12LL_I^2} \int_{-(\frac{L}{2}+L_I)}^{\frac{L}{2}-L_I} (V\cos(\theta) - U\sin(\theta))l dl \tag{5.113}$$

from which we can calculate the translation of the centre of the particle as $\dot{x}_{cm} = \dot{\theta}L_I sin(\theta)$ and $\dot{y}_{cm} = -\dot{\theta}L_I cos(\theta)$. Vertical trapping of the fibre occurs when the above equation for angular rotation equals zero.

5.3.3 Fluid Velocity Field

To estimate the flow field at the entry of the aperture, a commercial k-ϵ turbulent fluid simulation package, Inca from Amtec [104], was employed. Gooding [105] obtained and partially verified these flow field solutions in a previous study of pressure drop through the same narrow aperture considered here. For more details of the calculation and solution, in particular the turbulent and pressure components of the solution, see Gooding [105].

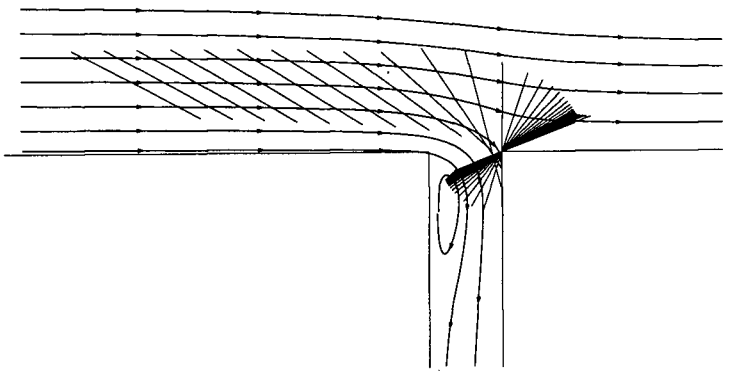

Figure 5.12: An example of a vertically trapped fibre ($L/W = 2$, $V_s = 4.11\text{m/s}$).

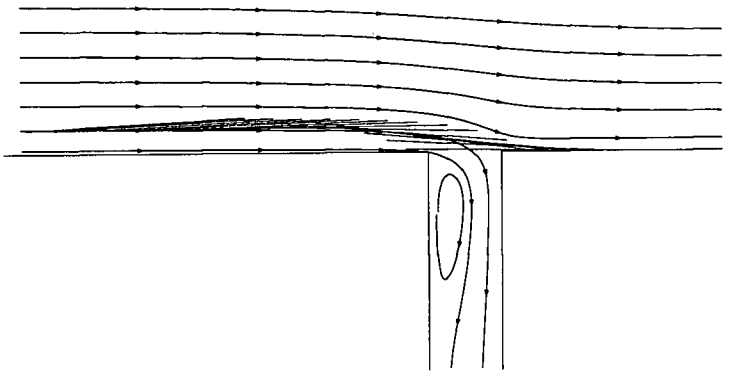

Figure 5.13: An example of a horizontally trapped fibre ($L/W = 3$, $V_s = 3.04\text{m/s}$).

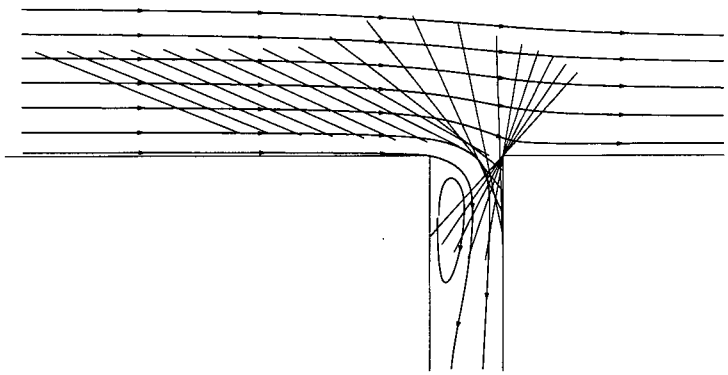

Figure 5.14: An example of a fibre wedged into the slot. ($L/W = 3$, $V_s = 3.04$m/s).

The flow field was calculated for a single geometry: a slot of width (W) of 0.5mm, a channel width of 19mm and a single average channel velocity, V_u, of approximately 7.5 m/s (see Fig. 2.2). The average slot velocity, V_s, was varied from approximately 1.5m/s to 7.1m/s, which gave a range of V_s/V_u similar to that studied experimentally by Kumar [44].

The fluid streamlines of the solutions used in this study are given in Figure 5.15. The prominent feature of the flows is the presence of fluid separation and recirculation on the upstream wall of the slot. This recirculation zone greatly increases the fluid velocity near the downstream side of the slot.

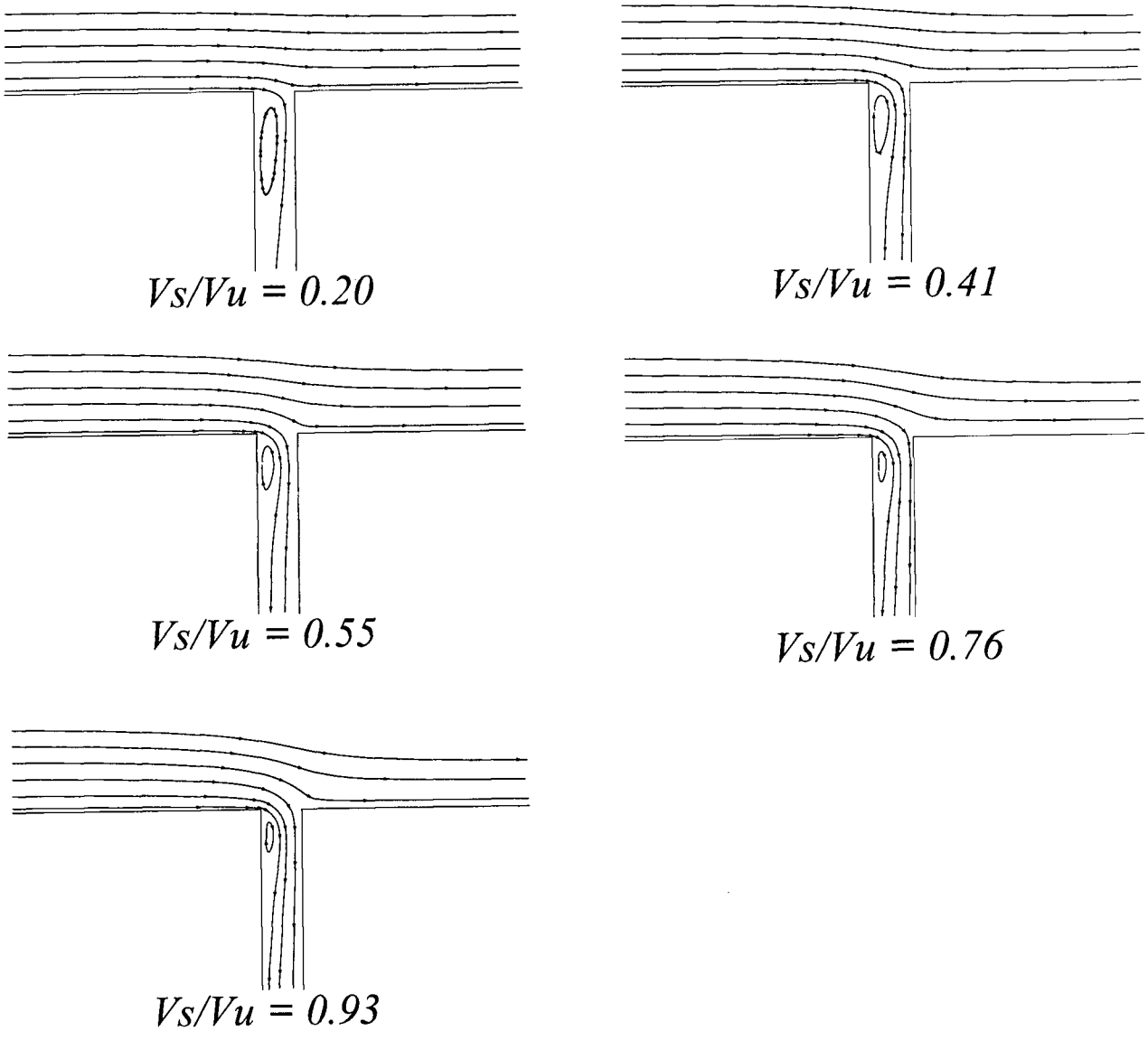

Figure 5.15: stream lines calculated from the CFD solutions of the mean flow field in the neighborhood of a single aperture. The slot width is 0.5mm, average channel velocity 7.5m/s.

5.4 Results

From given initial positions and orientations, fibre trajectories through the flow field were computed for both the free flowing and impact cases. Fibres met one of three possible fates: (1) they passed through the aperture, (2) they continued down the channel, or (3) they stapled in the slot in one of the modes described earlier.

The effect of initial orientation and height above the channel wall for a single flow field and fibre length on the probability of passage was examined by keeping the initial upstream position (x_0) constant at 2mm from the upstream slot edge, and varying the initial fibre orientation (θ_0) and height (y_0). The resultant trajectories for a single slot fluid velocity can be summarized by a "fate plot", as shown in Figure 5.16. This shows the result of the fibre trajectory as function of initial height (y_0), and orientation (θ_0), at a slot velocity of $V_s = 3.04$m/s. Each symbol on the graph represents a single trajectory for the initial orientation and height above the wall. The type of symbol represents the result of the trajectory, either stapled, accepted into the slot, or continued down the channel. See Table 5.4 for a summary of result and corresponding symbols. Four trajectories are also shown to demonstrate the possible results of the initial conditions.

Similar "fate plots" can be made for all of the numerically calculated flow fields for a single fibre length. From this series of plots, the effect of slot velocity on the passage of fibres can be determined. This was carried out for fibre length, L, to slot width, W, ratios of $L/W = 0.5$, 1, 2, 3, 4.

From these fate plots we can determine probabilities of passage and hence probability plots as a function of distance from the wall, assuming fibre orientation is uniformly distributed. The probability of passage at a given height, y_0, is calculated as the number of trajectories passing through aperture divided by the total number of trajectories simulated at that height. In addition to passing fibres (*e.g.* Figure 5.16 B), fibres stapled

Table 5.4: The symbols used by the "fate plots" to represent the possible outcomes of the simulation.

Symbol	Color	Result
$\times$	Blue	Passed into the slot
$+$	Green	Continued down channel
$\square$ (solid)	Light blue	Wedged into slot
$\square$ (hollow)	Purple	Horizontally stapled
$*$	Red	Vertically stapled

in the slot were assumed to pass into the slot (Figure 5.16 A and D). This assumption is supported by the high speed cinematography studies of Gooding [7], who observed that fibre accumulations on the slot eventually reach a plateau, after which, stapled fibres are continuously pulled into the slot.

5.4.1 $L/W = 0$

If the fibres are assumed to be inertialess, then a fibre of zero length would act as a point particle and follow the fluid streamlines. Under these circumstances, the initial height of the fibre, y_0, is the sole factor affecting whether it passes through aperture or not. If the initial height of the fibre's midpoint, y_0, is below the height of the exit layer, H, $(y_0 < H)$, then the fibre passes through the aperture. Thus, the probability of passage is given by

$$p = \begin{cases} 1 & \text{if } y_0/H < 1 \\ 0 & \text{if } y_0/H \geq 1 \end{cases} \tag{5.114}$$

5.4.2 $L/W = 0.5$

Trajectories were calculated for all initial values of height, y_0, and orientation, θ_0, and all slot velocities, V_s, for which CFD solutions of the flow field are available (see Figure

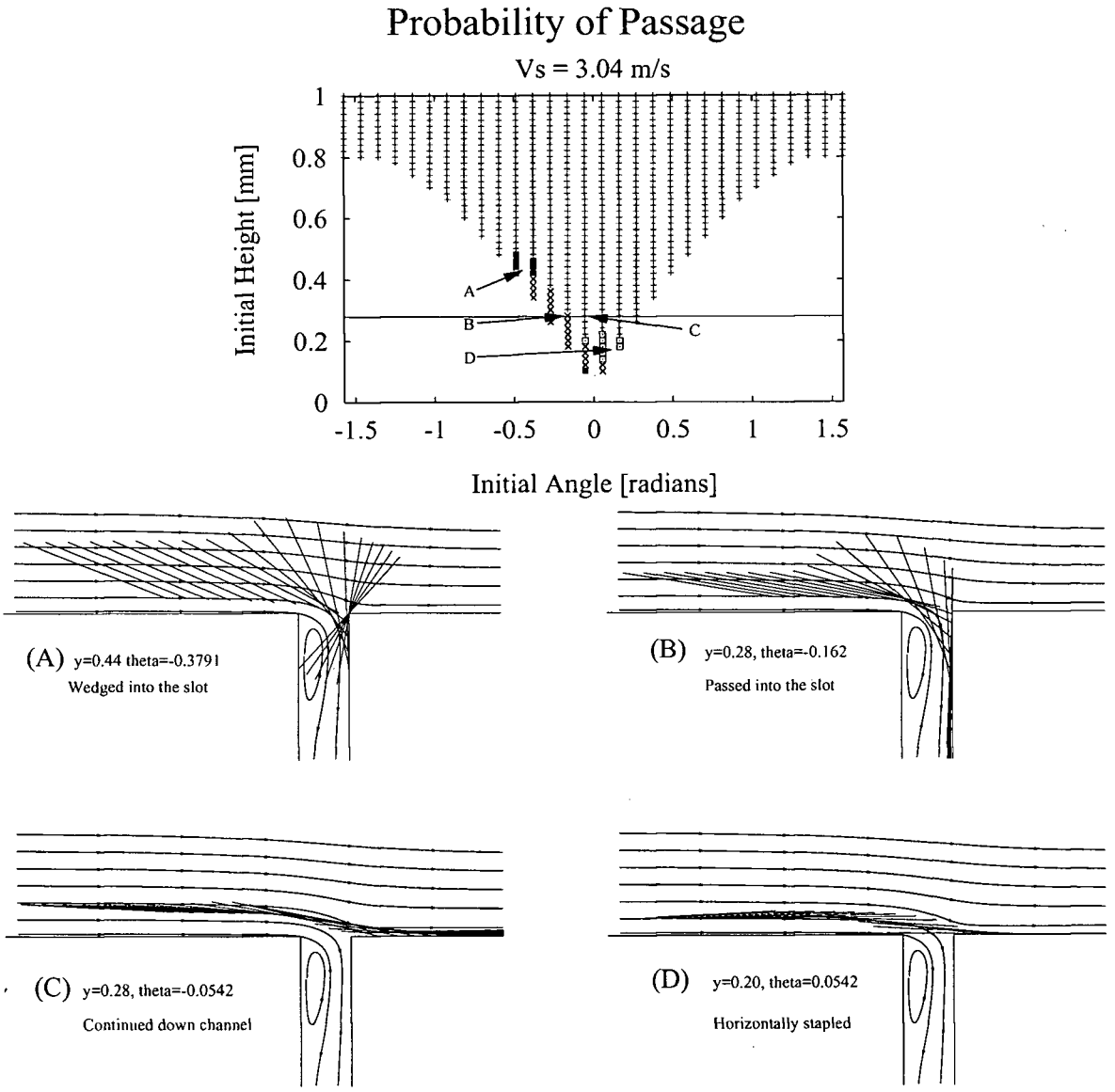

Figure 5.16: A "fate plot" showing the results of a fibre trajectory as a function of initial position and orientation. Each point represents the initial height and orientation of a fibre. The symbol represents the results of the fibre's trajectory. Four trajectories are shown demonstrating different possible outcomes. The horizontal line marks the exit layer height of the fluid (L/W=3, V_s = 3.04m/s).

5.15). For each slot velocity, V_s, a "fate plot", similar to Figure 5.16 was produced. The fate plots for fibres with length to width ratios of L/W = 0.5 are given in Figure 5.17. From these fate plots, it is evident that fibres in this length range acted similarly to tracer particles. Fibres passed into the slot if they originated within the exit layer. Fibres that originated close to the exit layer ($y_0 \approx H$) in some cases stapled on the edge of the slot.

Figure 5.18 shows the calculated probability of passage as a function of initial particle distance above the wall, y_0, normalized by the exit layer height, H. The error bars in the probability function plots represent the grid coarseness. As expected, the calculated probability is nearly identical to that of a tracer particle given by Equation 5.114.

5.4.3 $L/W = 1$

A similar series of fate plots for $L/W = 1.0$ is given in Figure 5.19. From this figure, we see that the probability of passage is still well described by Equation 5.114. However, the effect of orientation on passage is increasingly prominent as $L/W \geq 1$. Fibres having their leading tip pointed towards the slot entry (*i.e.* $\theta < 0$) are increasingly likely to enter the slot even if the fibre centre originates beyond the exit layer ($y_0 > H$). Similarly, if the fibre has a small positive orientation ($\theta_0 > 0$), the fibre may be rejected from the slot even if it originates within the exit layer. Again, fibres that originate at the streamline defining the exit layer height ($y_0 \approx H$) tend to staple on the downstream edge of the slot.

Assuming a uniform orientation distribution at each height, the probability of passage as a function of height is plotted in Figure 5.20. From this figure, we see that probability functions are centred on the exit layer, but are slightly skewed, showing the small effect of fibre orientation. However, the position of the fibre with respect to the height of the exit layer remains the predominant factor affecting fibre passage.

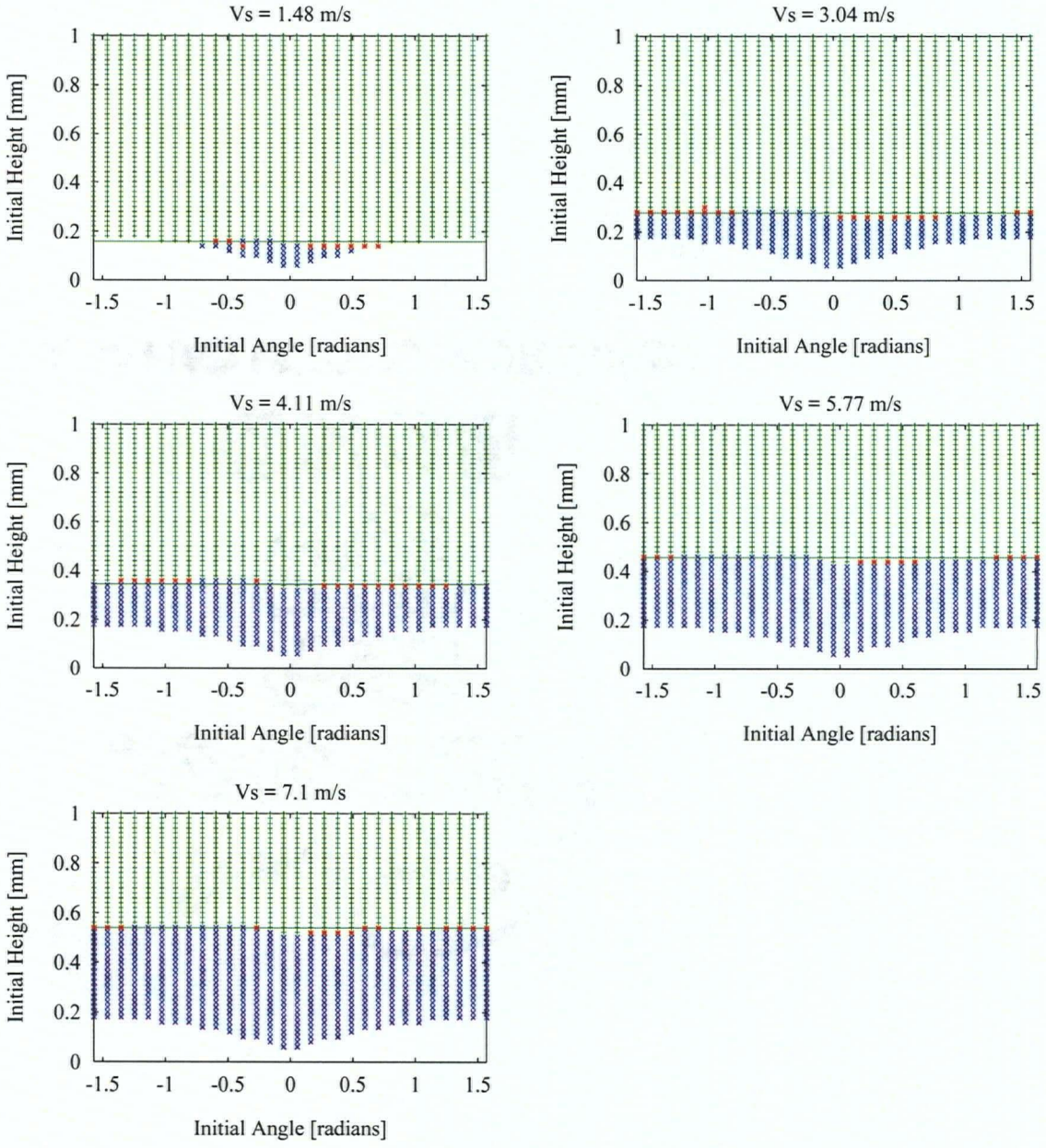

Figure 5.17: The effect of initial height and orientation on passage for fibre with $L/W = 0.5$ and V_s/V_u of 0.2, 0.41, 0.55, 0.76, 0.93

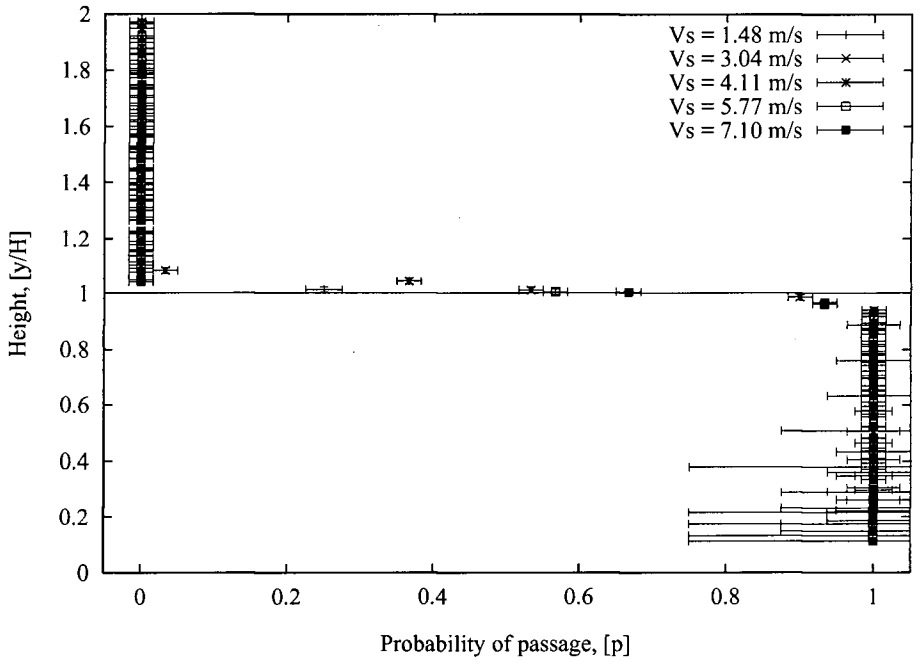

Figure 5.18: The probability of passage as a function of height above the wall normalized by exit layer height for $L/W = 0.5$ and all slot velocities.

5.4.4 $L/W = 2$

From the fate plots given in Figure 5.21 for fibres with $L/W = 2.0$, we see that as L/W increases, so does the effect of orientation. Fibres with an initial negative orientation ($\theta_0 < 0$) are drawn from a region beyond the exit layer. Fibres with a positive orientation ($\theta_0 > 0$) become horizontally stapled on the top of the slot. At a low slot velocity, there are few vertical staples, but their number increases dramatically as slot velocity approaches the cross flow velocity (*i.e.* $V_s/V_u \rightarrow 1$). This occurs because for a fibre impacting on the edge of the slot, the moment from the cross flow is more likely to balance the moment from the slot flow.

Interestingly, the increased passage of fibres with a negative orientation is nearly equal to the decreased passage of fibres with a positive orientation. On average, the number of fibres accepted into the slot is similar to that for point particles ($L = 0$), which have

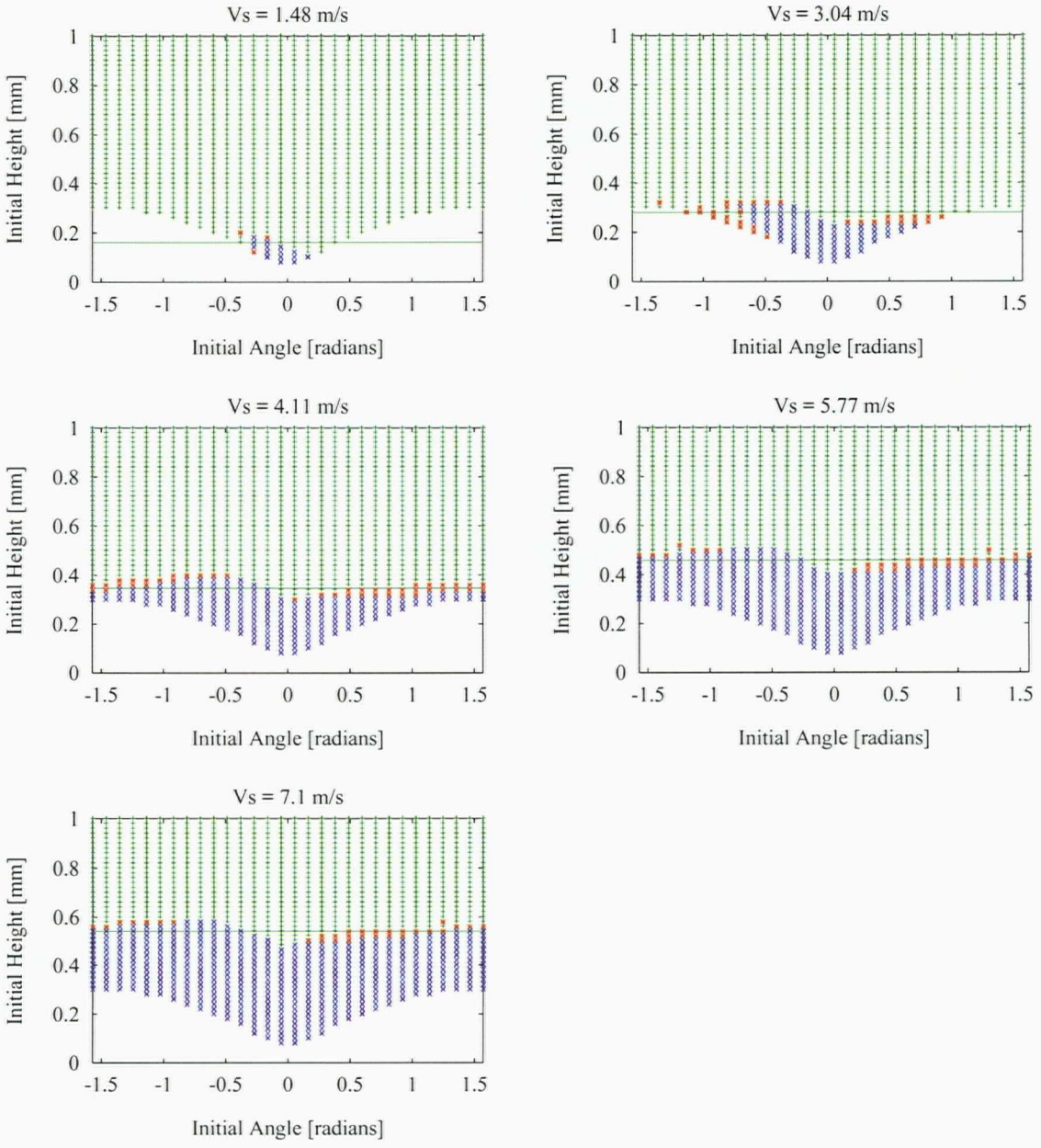

Figure 5.19: The effect of initial height and orientation on passage for fibre with L/W=1.0 and V_s/V_u of 0.2, 0.41, 0.55, 0.76, 0.93

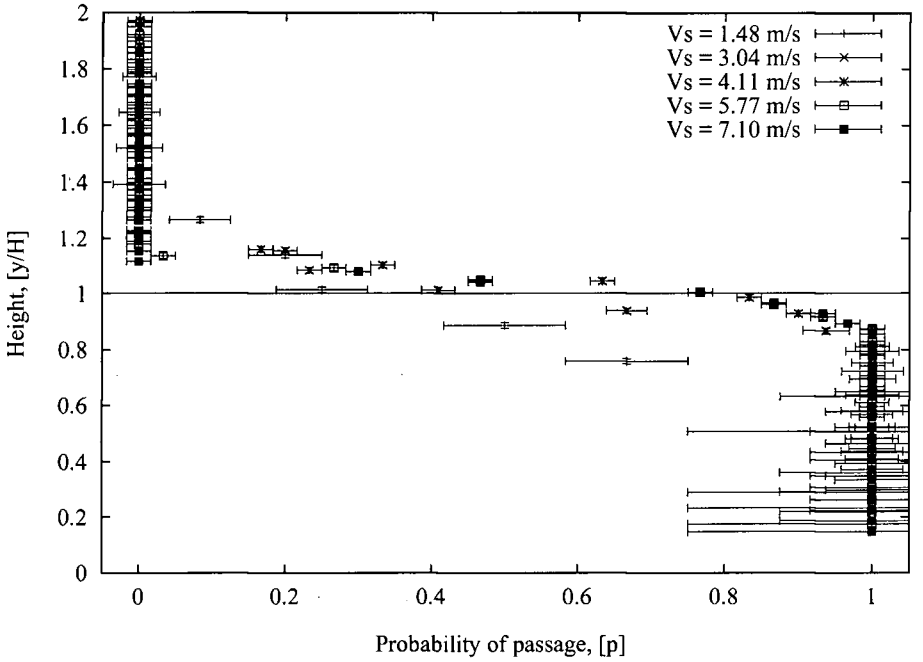

Figure 5.20: The probability of passage as a function of height above the wall normalized by exit layer height for L/W=1.0 and all slot velocities.

a probability of passage given by Equation 5.114.

The probability of passage as a function of height is calculated and shown in Figure 5.22. Again, the probability of passage function is determined largely by the exit layer height. When $\theta_0 > 0$, the effect of orientation gives an increased probability of being rejected if the fibre originates within the exit layer. When $\theta_0 < 0$, there is an increased probability of being accepted.

5.4.5 $L/W = 3, 4$

As fibre length continues to increase, the effect of orientation on passage continues to become more pronounced. This can be seen in the two series of fate plots for $L/W = 3$ and 4 given in Figures 5.23 and 5.24, respectively. Fibres no longer vertically staple on the down stream edge of the slot. Fibres that impact on the downstream wall of the slot

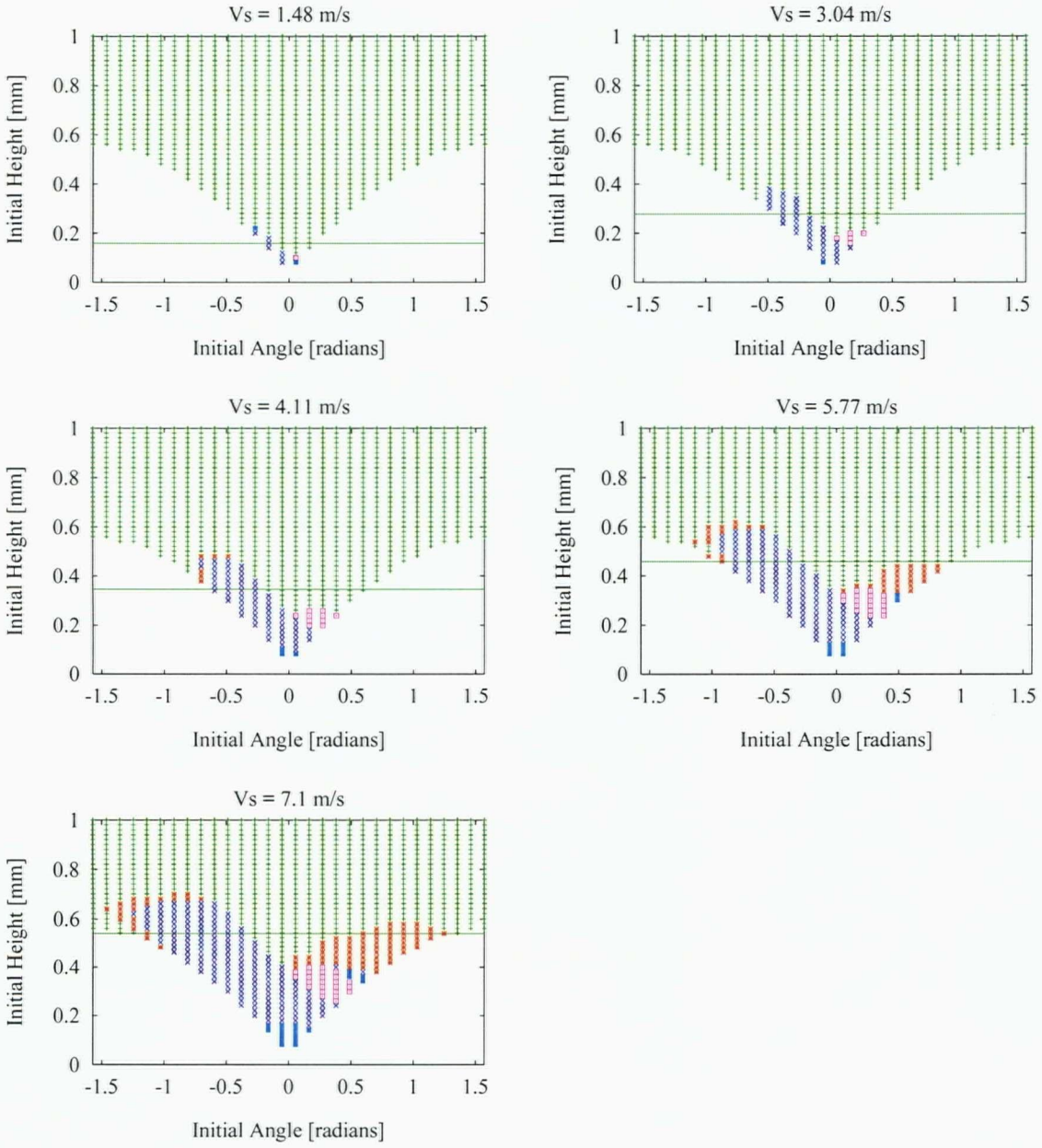

Figure 5.21: The effect of initial height and orientation on passage for fibre with L/W=2.0 and V_s/V_u of 0.2, 0.41, 0.55, 0.76, 0.93

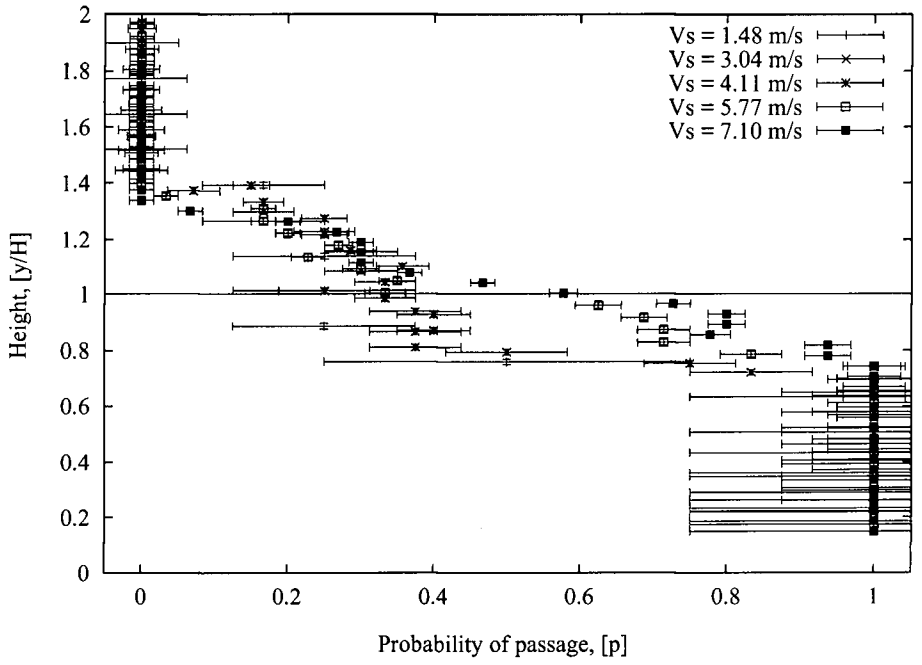

Figure 5.22: The probability of passage as a function of height above the wall normalized by exit layer height for L/W=2.0 and all slot velocities.

rotate on the aperture edge causing the leading tip of the fibre to contact the upstream wall of the slot. The force from this wall causes the fibre to lock at this position. This condition was referred to as a "wedge staple". It was observed by Kumar [44] for stiff fibres having $L/W > 2$, and was thought to account for the observed S-shaped passage ratio curves.

From the fate plots for $L/W = 3$ and 4, the probability of passage is calculated and given as Figures 5.25 and 5.26, respectively. These figures show that, even with fibre lengths considerably longer than the slot, the average passage is primarily governed by the exit layer height, H.

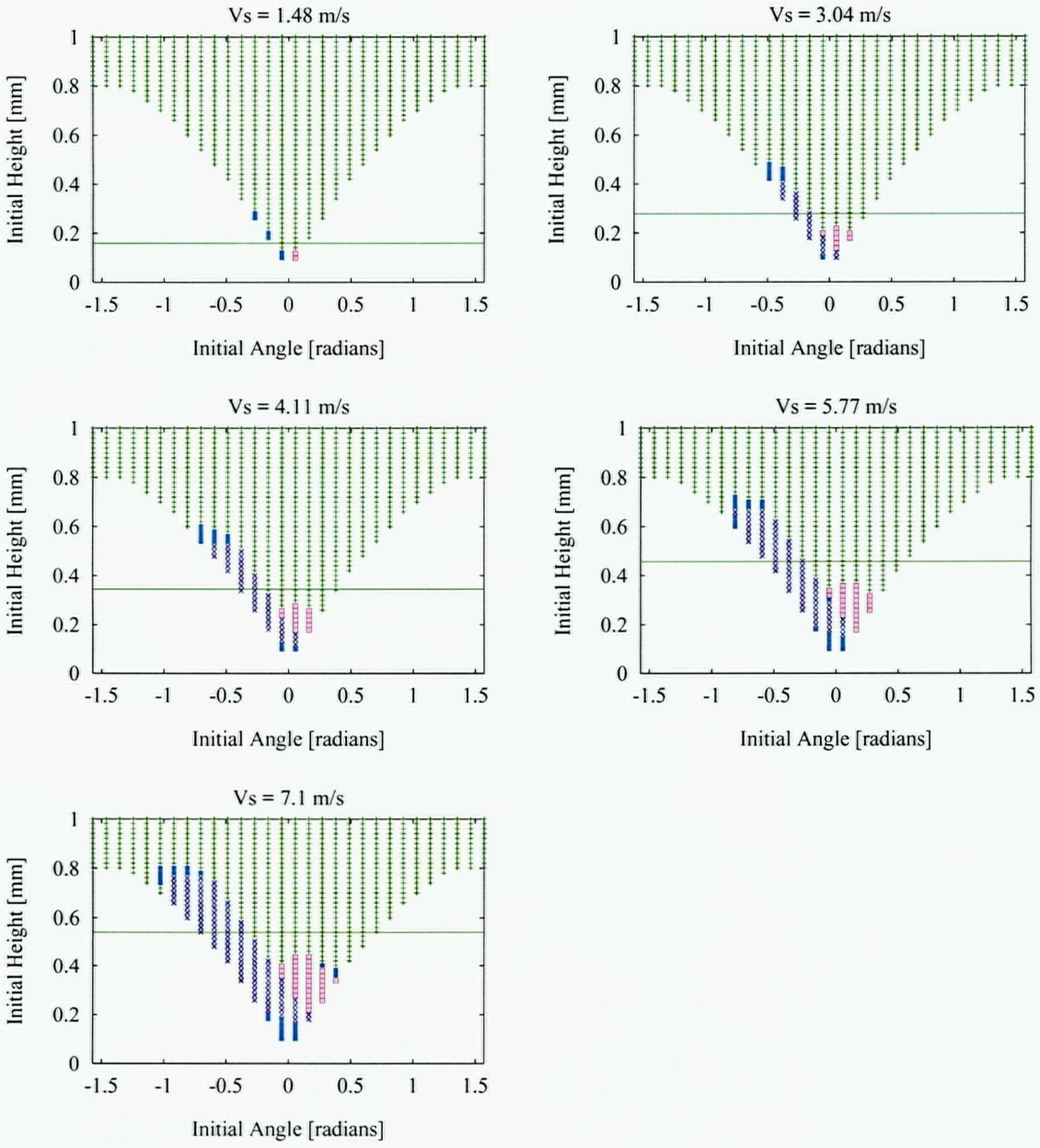

Figure 5.23: The effect of initial height and orientation on passage for fibre with $L/W = 3.0$ and V_s/V_u of 0.2, 0.41, 0.55, 0.76, 0.93

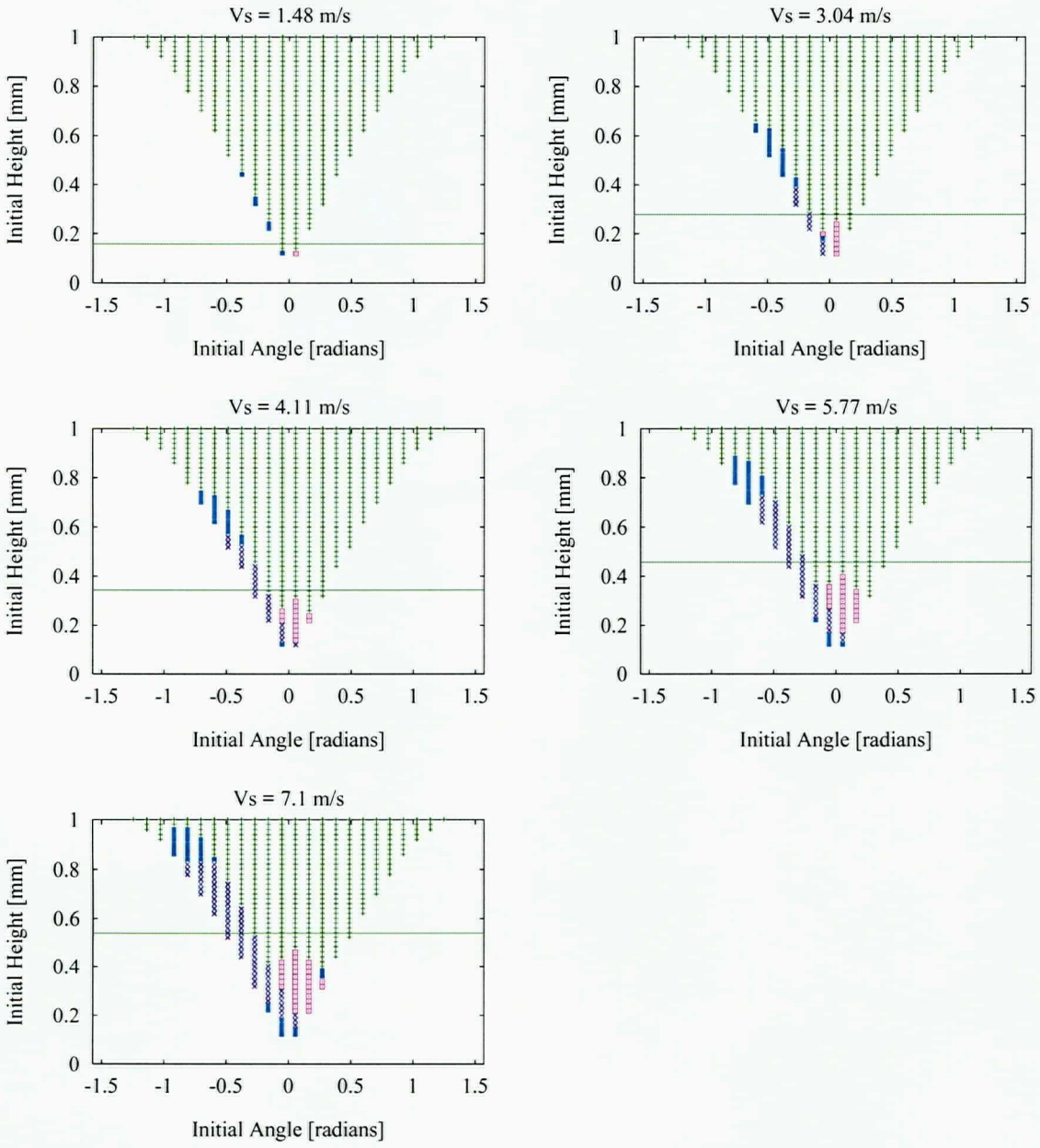

Figure 5.24: The effect of initial height and orientation on passage for fibre with $L/W = 4.0$ and V_s/V_u of 0.2, 0.41, 0.55, 0.76, 0.93

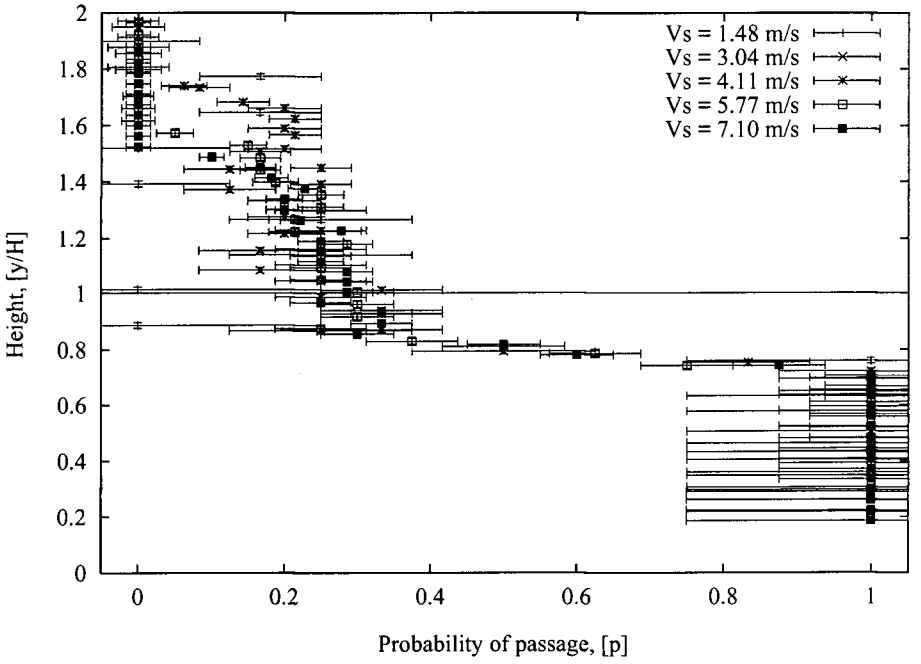

Figure 5.25: The probability of passage as a function of height above the wall normalized by exit layer height for $L/W = 3.0$ and all slot velocities.

5.5 Discussion

The simulations presented here demonstrate the complexity of fibre passage through a narrow aperture and the difficulties of accurately modeling the trajectories. Despite these difficulties, however, a model was developed to predict the effect of initial orientation (θ_0) and height above the duct wall (y_0) on fibre passage, rejection, or stapling at the slot. It has also been demonstrated that passage is affected by fibre contact with the aperture walls.

The result has shown that, for fibres with $L/W \leq 2$, fibre passage is primarily a function of the exit layer height, H. For longer fibres ($L/W > 2$) the mean fibre passage remains primarily overned by the initial height with respect to the exit layer height, because rejection of fibres with a positive orientation from the exit layer is partially

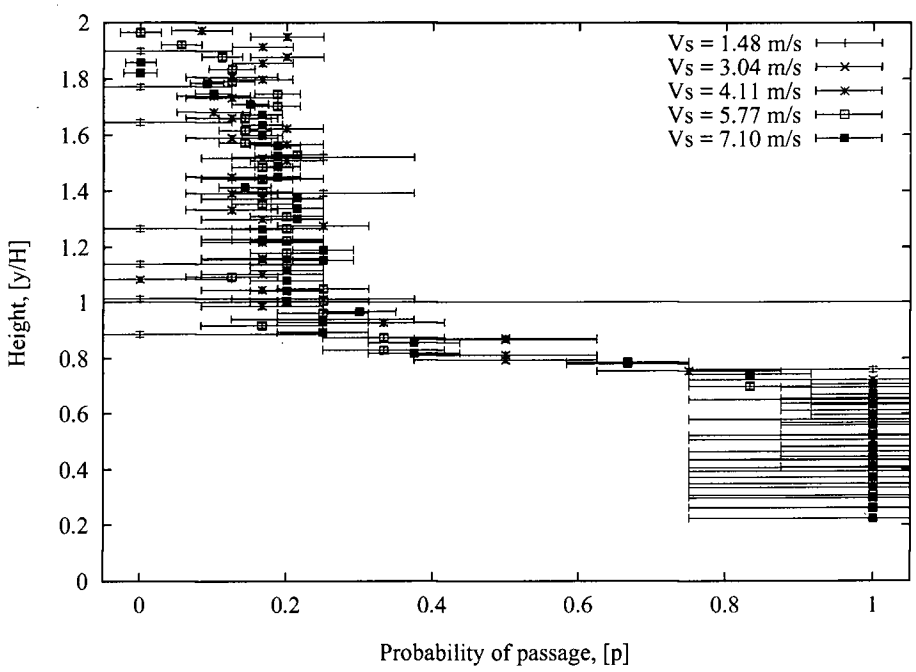

Figure 5.26: The probability of passage as a function of height above the wall normalized by exit layer height for $L/W = 4.0$ and all slot velocities.

balanced by the increased passage of fibres with a negative orientation. As a first order approximation, passage is well described by Equation 5.114.

By observing the simulated trajectories, the majority of fibre rejections from the slot occurs when the leading tip of the fibre does not enter the aperture. A combination of orientation and position of the centre with respect to exit layer height affects the fibre trajectory into the aperture. If the initial orientation is not sufficiently negative, for passage to occur, the fibre must be closer to the wall. Similarly, if the angle is sufficiently negative, the fibre can enter the aperture from a position beyond the exit layer.

The simplifying assumptions for this model limit its usefulness for obtaining quantitative estimates of pulp fibre passage. Nevertheless, the model indicates the likely effect of key variables on passage. Real fibres are flexible. Fibre bending should increase the ability of the fibre to follow the fluid streamlines, increasing the probability of passage

of long fibres originating within the exit layer. Bending could also lead to a significant increase in vertical stapling because of the increased stability of the bent fibre on the downstream aperture edge. From the work of Gooding [43], on long fibres, this additional stapling leads to an increased passage ratio.

In 3-dimensional flow, some fibres are oriented perpendicular to the flow and therefore act as a point in the plane modeled here. In this case, as described earlier, passage is governed solely by the position of the fibre (y_0) in the upstream flow. Thus the "wall effect" governs. The "turning effect" is of no consequence.

The force balance in the simulation used a coefficient of friction of 0.3; however, a range of other values were explored. The results were nearly identical except for a small increase in the probability of vertical stapling on the slot edge at higher friction coefficient. At a friction coefficient of zero, there was almost no vertical stapling.

5.6 Summary

To estimate the probability of passage, we developed a simple numerical model which estimates fibre trajectories in the entry flow of a single aperture. Equations of motion were derived for fibres in free flow and for fibres in contact with the aperture walls. The model made a number of simplifying assumptions: the fibres were rigid and inertialess, motion was in two dimensions (planar) and the drag force was Stokesian (*i.e.* proportional to the difference between fibre and fluid velocity). The trajectories were calculated by integrating the equations of motion through a computationally-derived fluid flow field near the aperture entry. The model demonstrated the complex interactions between the fibres and the slot during passage, and the challenges involved in modeling this phenomena.

The model was used to predict the effect of fibre length, slot velocity, initial fibre

position and orientation on passage. From the calculated trajectories, it was shown that fibres passed through the slot only if their leading tip entered the slot. This resulted in passage of some fibres with a negative orientation ($\theta_0 < 0$) even if they originated outside the exit layer ($y_0 > H$). Also, some fibres with a positive orientation ($\theta_0 > 0$) were rejected even if they originated within the exit layer ($y_0 < H$). The number of fibres accepted from beyond the exit layer was approximately the same as that rejected from within the exit layer. The net effect of these two factors was that the number of fibres passing through the aperture was approximately equal to the number of fibres that originated within the exit layer, assuming fibres to be uniformly distributed in the allowable orientations and positions in the flow.

By calculating trajectories for all possible initial conditions the probability of passage was estimated as a function of fibre length and slot velocity. As a first order approximation, if fibres originated within the exit layer, they passed through the slot, and if fibres originated outside the exit layer, they did not. Orientation effects were secondary. Thus, as a first order approximation the probability of passage is given by

$$p = \begin{cases} 1 & \text{if } y/H < 1 \\ 0 & \text{if } y/H \geq 1 \end{cases} \tag{5.115}$$

These finding imply that, for the fibres tested here, the position of the fibre near the wall upstream of the slot dominates fibre passage through an aperture. The "turning effect" suggested by Gooding [7, 43] has a secondary effect.

5.7 Nomenclature

Table 5.5: The following nomenclature was used in this section.

$\vec{C}$, C_x, C_y	Simplifying variables.
D	Stokes drag tensor.
$\vec{F}_I$	Force on fibre due to impact with the boundary.
F	Magnitude of impact force vector (approximately).
$\vec{F}$	Net external force on the fibre.
H	Exit layer height.
I	Identity matrix.
I_x, I_y, I_m	Simplifying variables; each represents an integral.
L	Fibre length.
l	Position along the fibre's major axis.
L_I	Position along fibre of impact with boundary.
Λ	Integral length scale.
$\vec{M}$	Net external moment on the fibre.
p	Probability of passage.
$\vec{\mathbf{p}}$	Fibre orientation vector; a unit vector parallel to fibre's major axis.
$\dot{\vec{\mathbf{p}}}$	Fibre rotational vector; time derivative of the orientation vector.
$\mathcal{R}$	Lagrangian particle spatial velocity correlation.
θ	Angle of the major axis of the fibre with respect to the x axis.
θ_0	Initial trajectory orientation of fibre centre.
u	Fluctuating component of fluid velocity.
v	Fluctuating component of fibre centre velocity.
U, V	x and y components of fluid velocity.
$\vec{u}_{cm}$	Particle centre velocity.
V_s	Average slot fluid velocity.
V_u	Average upstream channel fluid velocity.
W	Slot width.
x_{cm}, y_{cm}	x and y components of particle centre velocity.
x, y	Cartesian coordinates.
y	Distance from the channel wall; Cartesian co-ordinate.
y_0	Initial trajectory height of fibre centre.

Chapter 6

EXPERIMENTAL MEASUREMENT OF FIBRE CONCENTRATION

6.1 Introduction

From the simple analysis presented in Chapter 3, we showed that the fibre passage ratio is a function of the probability of fibre passage and the upstream fibre concentration profile. The probability of passage was examined in Chapter 5. Here we examine the contribution of the fibre centre concentration profile.

In earlier work, using high speed cinematography of fibres passing through an aperture, it was determined that the concentration of 3mm fibres in the exit layer ($H \approx 0.5mm$) was approximately 0.3 of the mean fibre concentration in the channel [7, 43]. The lower concentration near the wall was called the "wall effect". The concentration profiles determined in this earlier work were for a single fibre length, and determined at only five heights from the wall. Unfortunately, the effect of fibre length on the concentration profile was not determined. Neither was the detail of the concentration profile determined to sufficient accuracy to calculate its effect on the passage ratio.

The aim of this study is to experimentally determine the detailed distribution of fibre concentration and orientation upstream of the slot entry for a range of fibre lengths. From the experimentally measured concentration profiles, the contribution of the wall effect on the passage ratio can be determined.

6.2 Experimental Apparatus and Procedure

Fibre concentrations and orientations were measured by imaging fibres in flow approaching a single slot in a rectangular plexiglass test section of a flow loop.

The flow loop consists of a large reservoir, piping, and a variable speed pump. The suspension flows through a 36mm diameter round pipe, flow meter, through a 20mm square plexiglass channel, and then back to the reservoir [105]. At the downstream end of the plexiglass channel, a removable test section containing a slot in one wall can be inserted to study the passage of fibres through apertures.

Fibres at a location 30cm downstream from the test section entry were observed by video imaging. An electronically shuttered, CCD camera was mounted transverse to the flow direction. The camera captured images at $1/30s$ with a shutter speed of $1/30000s$. This high shutter speed is used for stop-motion photography. The test section was illuminated by a 30 watt halogen lamp mounted on the opposite side of the test section (see Figure 6.27).

The camera was equipped with a long working distance macro lens and a small aperture setting to ensure that fibres were sharply imaged over the entire depth of the channel. This enabled accurate determination of the fibre concentration throughout the channel. For each experimental condition, 1800 images at 256hx240v resolution and a magnification of 0.0383 mm/pixel were acquired, electronically stored and analyzed manually.

A typical fibre image is shown in Fig. 6.28. From the acquired images, the height of the fibre centre above the wall, y, the orientation, θ, and the projected length, L_p, of each fibre is recorded (see Figure 6.29). Fibres within 50 pixels (approximately 2mm) of the image edges were not used to avoid length biases, from fibres partially lying outside the image.

The channel velocity for all experiments was 7.1 m/s, a representative velocity in

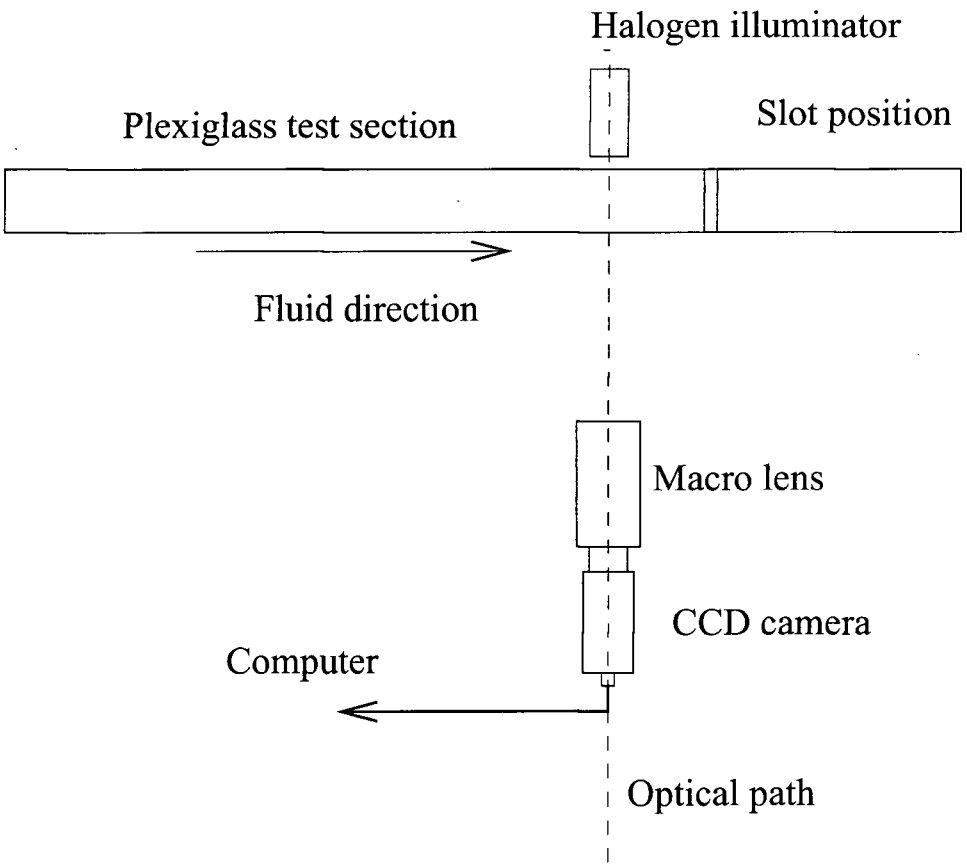

Figure 6.27: A schematic of the experimental apparatus, including the camera, square transparent channel, and halogen illumination.

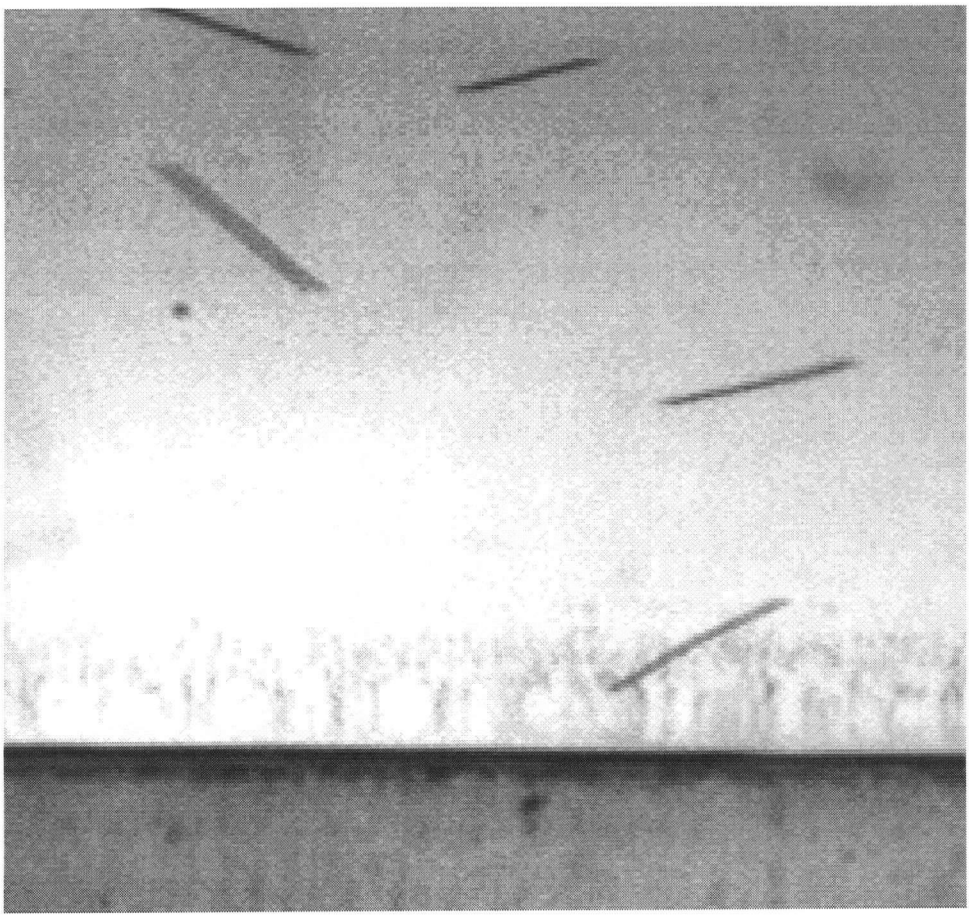

Figure 6.28: A typical image of the blue dyed, 2mm long nylon fibres, flowing near the plexiglass channel wall.

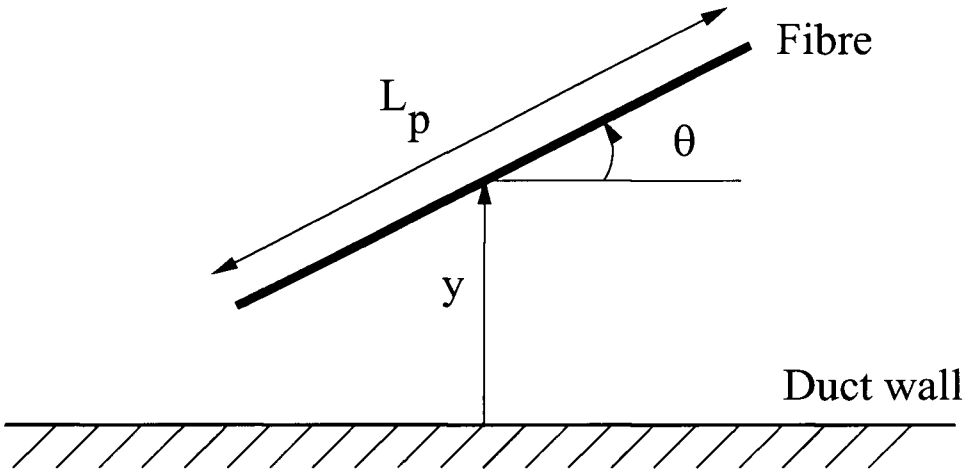

Figure 6.29: A schematic diagram of a fibre near the wall, depicting the variables measured for each fibre.

a industrial pressure screen, and one similar to the test conditions used previously for fibre passage measurements [7, 43, 44]. The channel Reynolds number is approximately 1.4×10^5, ensuring fully turbulent flow. Dyed nylon fibres of lengths of 1.1, 2.0 and 3.1 mm were used. All had a denier[1] of 18.0 and a relative density of 1.13, which corresponds to a fibre diameter of approximately 40 microns. The fibre concentration is less than 5000 fibres/litre, ensuring a low crowding factor ($N \leq 0.1$) and therefore negligible interactions between fibres [106, 44].

6.3 Results

From the analyzed fibre images, the location of fibre centres, angle of orientation to the wall, and projected fibre lengths were calculated for 1mm, 2mm and 3mm long fibres.

[1] 1 denier = 9000m/g

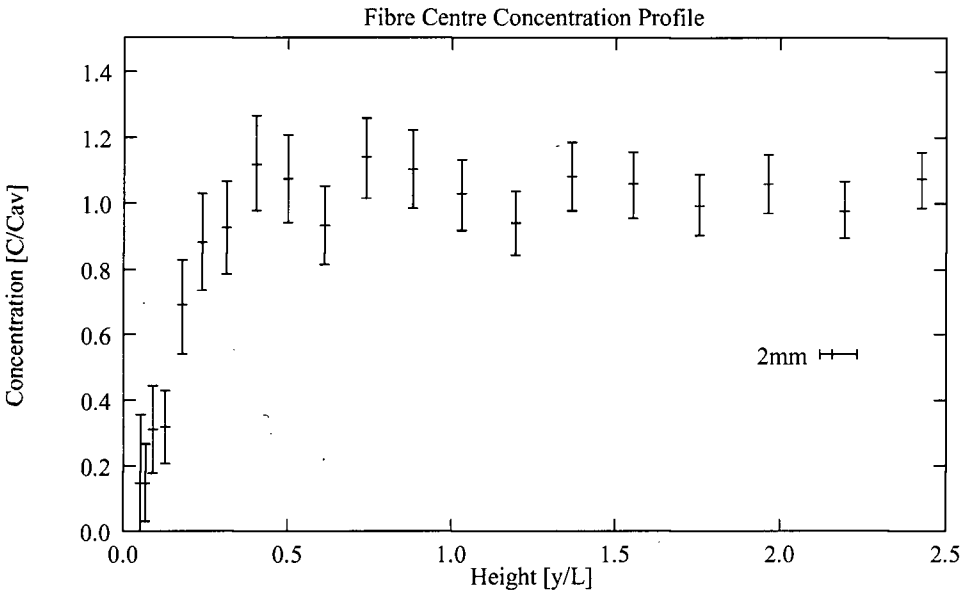

Figure 6.30: Fibre concentration normalized by the mean channel concentration as a function of height above the wall normalized by the fibre length for 2mm nylon fibres.

6.3.1 Concentration Distribution of Fibres

Fibre concentration profiles as a function of distance from the wall were determined from the total number of fibre centres within an interval (Δy), divided by total volume of water within the interval. The total volume analyzed in each interval is calculated by multiplying together the number of images analyzed, the width of the analyzed image, the depth of the channel and the interval height. Error bars representing 95% confidence intervals on the measured concentration were determined, assuming that the arrival rate of fibres in the measurement volume followed a Poisson distribution.

Figure 6.30 shows a typical concentration profile, plotted as local concentration, C, normalized by the average channel concentration, C_{av}. The distance from the wall was normalized by fibre length, y/L, where L is fibre length.

As shown in Fig. 6.30, fibre concentration near the wall ($y/L \approx 0$) is approximately zero ($C \approx 0$). It increases linearly to a distance approximately $L/3$, where it reaches the

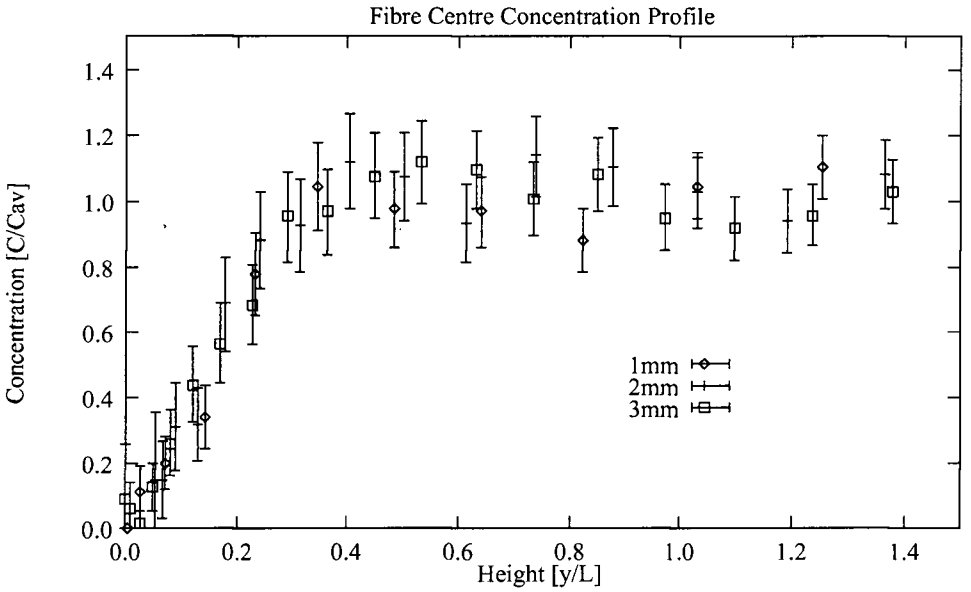

Figure 6.31: Fibre Concentration normalized by the mean channel concentration as a function of height above the wall normalized fibre length for 1mm ($\diamond$), 2mm ($+$), and 3mm ($\square$) nylon fibres.

mean concentration, and remains relatively constant beyond this point, *i.e.*

$$\frac{C}{C_{\text{av}}} \approx \begin{cases} my/L & \text{if } y/L < 1/m \\ 1 & \text{if } y/L \geq 1/m \end{cases} \tag{6.116}$$

For the data plotted in Figure 6.31, the fitted value for m is 3.22. Figure 6.31 shows that differing fibre lengths yielded a concentration profile similar to that in Fig. 6.30. Thus, the concentration profile can be described by a single dimensionless function, dependent only on y/L.

6.3.2 Orientation Distribution of Fibres

The angle of fibre orientation relative to the channel wall and the height above the channel wall were simultaneously determined. From the height and orientation of each fibre analyzed, a probability histogram was generated by sorting the fibres into 15 angle

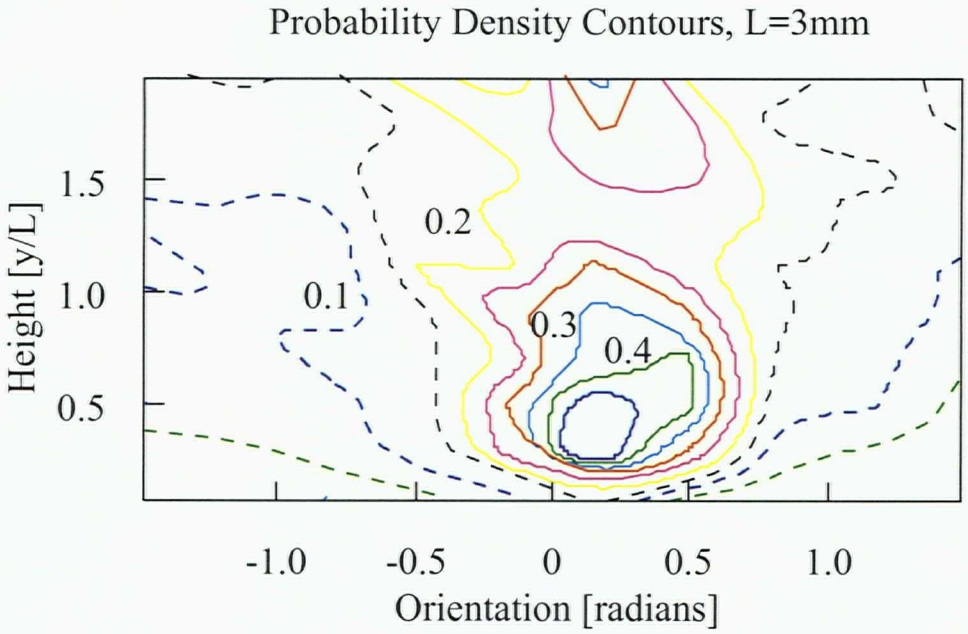

Figure 6.32: Probability density contours for height, y/L, and orientation, θ, for 3mm fibres.

bins ranging from $-\pi/2$ to $\pi/2$ and 15 height bins over the range 0 to 2.0 L.

Figures 6.32, 6.33, and 6.34 show the contour plots of the probability histograms for fibre orientation and height for fibres of length 3mm, 2mm and 1mm, respectively. These figures show that in the range $0.25L < y/L < 0.7L$, the fibres are preferentially positively oriented, that is, the downstream end of fibres preferentially point away from the wall. In this region, the probability of being positively oriented is nearly twice the probability of being negatively oriented. The data of Gooding and Kerekes [43] show a similar result. As fibre length decreases the preferred orientation becomes less distinct.

6.3.3 Projected Fibre Length Distribution

The projected length of the fibre, L_p, was also measured for each imaged fibre. This projected length is an indication of the out-of-plane orientation of the fibre.

Figure 6.35 shows the average normalized projected fibre length, L_p/L, as a function

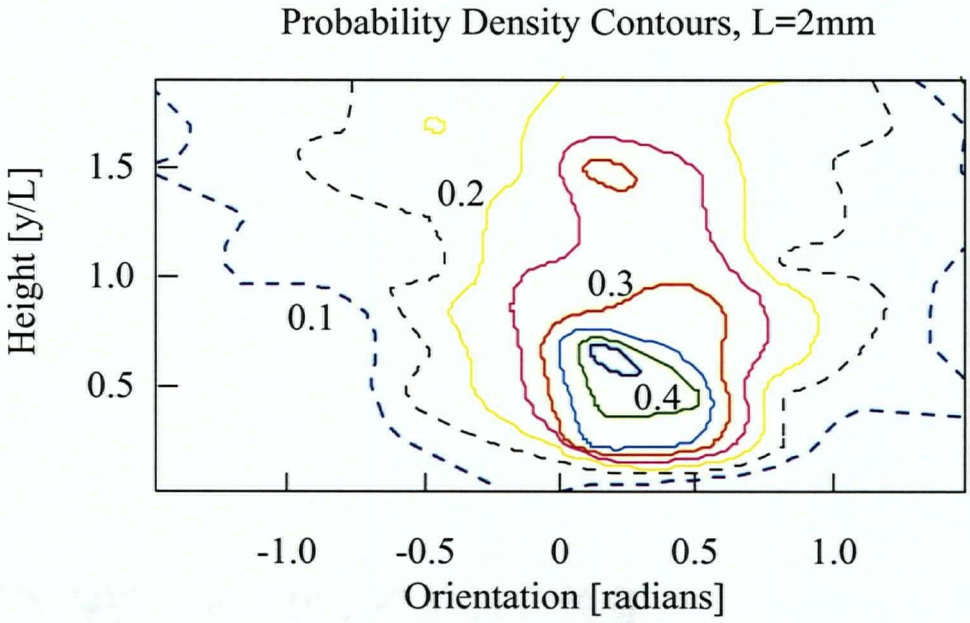

Figure 6.33: Probability density contours for height, y/L, and orientation, θ, for 2mm fibres.

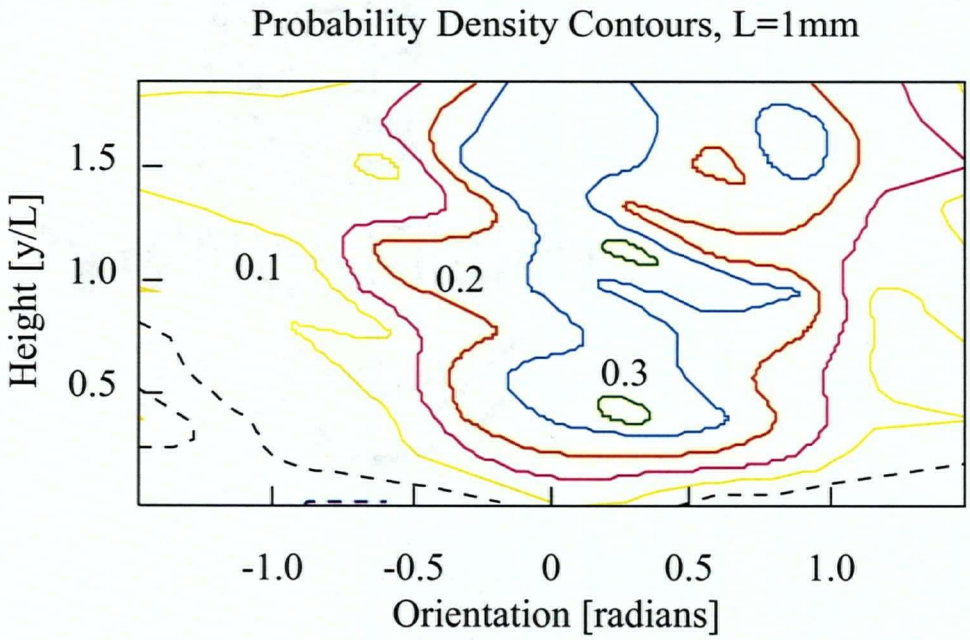

Figure 6.34: Probability density contours for height, y/L, and orientation, θ, for 1mm fibres.

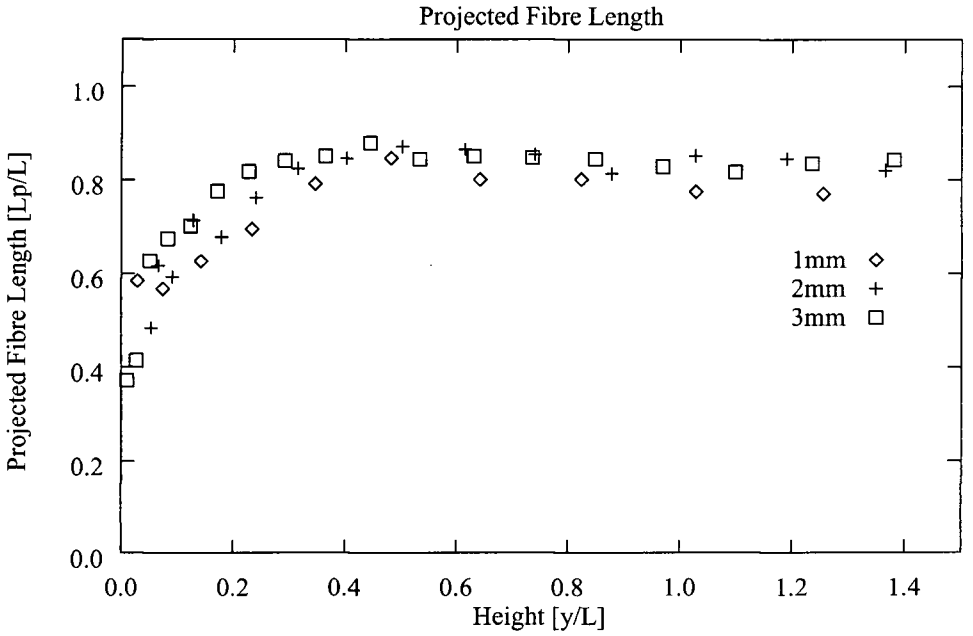

Figure 6.35: The average projected fibre length as a function of height away from the wall, y/L, for 1mm, 2mm and 3mm fibres.

of height above the channel wall. Very close to the wall, $L_p/L \approx 0.5$, but this increased to $L_p/L \approx 0.8$ at $y/L = 0.3$.

6.4 Discussion

These experimental results demonstrate that the wall has a profound effect on fibre motion and the resulting concentration and orientation distributions. From the theory presented in Chapter 4, a simple expression for the rotation of a fibre in a constant velocity gradient was derived. It demonstrated that fibres rotate near the duct wall due to the velocity gradient. The mechanism of fibre transport away from the wall by impaction with the wall during rotation is discussed below.

The equation of motion of a fibre in an arbitrary flow field is given by Equations 4.19 and 4.20. In two dimensions, planar rotation, $\dot{\theta}$, is given by

$$\dot{\theta} = \frac{12}{L^3} \int_{-\frac{L}{2}}^{\frac{L}{2}} (-U(l)\sin(\theta) + (V(l)\cos(\theta))ldl \tag{6.117}$$

in terms of the fluids x and y components of velocity, U and V. This integral equation can be simplified by approximating the velocity gradient as a constant over the length of the fibre. This results in

$$\dot{\theta} = \frac{1}{2}\sin(2\theta)(\frac{\partial V}{\partial y} - \frac{\partial U}{\partial x}) + \cos^2(\theta)\frac{\partial V}{\partial x} - \sin^2(\theta))\frac{\partial U}{\partial y} \tag{6.118}$$

For the case of interest here, rotation in a plane and flow near the wall, the only non-zero velocity gradient is $\partial U/\partial y \approx v^*/\kappa y$ (log law of the wall, see Chapter 7). This yields a simple approximate equation for the fibre rotation, given by

$$\dot{\theta} = -\sin^2(\theta))\frac{\partial U}{\partial y} \tag{6.119}$$

Equation 6.119 shows that when $\theta \neq 0$, fibres rotate with a negative angular velocity ($\dot{\theta} < 0$). When the fibre is parallel with the streamlines ($\theta = 0$) its angular velocity is zero, meaning the fibre does not rotate. However, this condition is unstable, any perturbation towards $\theta < 0$ causes the fibre to continue its rotation with a negative angular velocity. From Equation 6.119 we see that the fibre's angular velocity is proportional to the fluid's velocity gradient. Since the fluid velocity gradient is strongest near the wall, fibres closer to the wall rotate more quickly than fibres farther from the wall.

In the presence of the wall, fibres with a height of $y < L/2$ will rotate with a negative angular velocity ($\dot{\theta} < 0$). This rotation leads to an impact between the fibre's end and the wall (Fig. 6.36a). As the fibre continues to rotate, the centre of the stiff fibre must move away from the wall (Fig. 6.36b). This transport mechanism creates the observed concentration gradient.

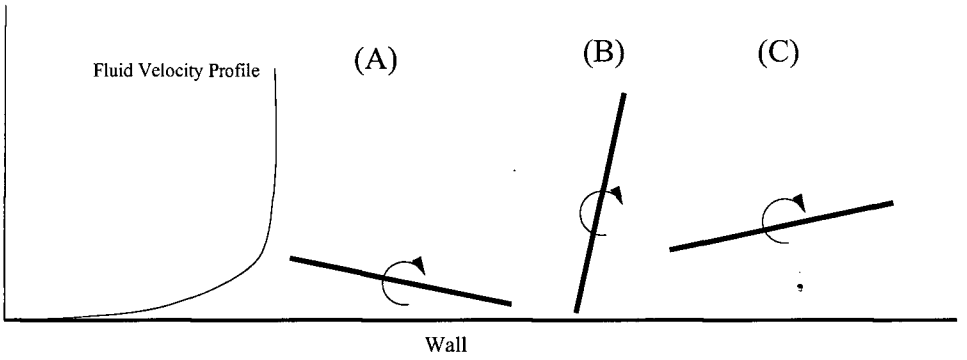

Figure 6.36: A schematic of a fibre rotating near the wall ($y < L/2$), impacting the wall (A) and being transported away (B). The fibre then rotates more slowly resulting in a preferred positive orientation (C).

After being forced away from the wall, the fibre begins to rotate freely, with its orientation starting at $\theta = \pi/2$ (fibre orientation is determined as $-\pi/2 < \theta < \pi/2$). The fibre centre is now now farther from the wall. Assuming a log-law fluid velocity profile, which has a strong velocity gradient near the wall that quickly diminishes as a function of distance from the wall, the fibre will rotate relatively more slowly at this new height. Because fibres transported from the wall have a slightly positive orientation, and they rotate slowly before being transported away by turbulent fluctuations, the observed preferred positive fibre orientation results (Figure 6.36c). After the fibre moves away from the wall and is left in a positive orientation, it can be further transported away from the wall by the turbulent fluctuations. This results in the persistence of the preferred positive orientation above $y = L/2$. Fibres transported back toward the wall undergo the same rotation and transport process.

To illustrate some of the mechanisms of fibre transport and rotation discussed in this chapter, high speed video imaging was used to capture the motion of fibres in turbulent flow, near the wall[2]. Because of the limited frame rate of the the camera (1000 frames

[2]Some of this footage is available as MPEG animations from the author.

per second), the mean channel velocity was slowed down to 2 m/s. At this bulk velocity, the Reynolds number of the flow is above the turbulent threshold, with a value of approximately 4×10^4. Figure 6.37 shows a single 2mm long fibre rotating in the velocity gradient near the wall (Frames 544-545) and impacting against the wall during this rotation (Frame 546). The fibre centre is subsequently transported away from the wall (Frame 547-550) and persists at the new height and positive orientation (Frames 550-553).

6.5 Summary

Near-wall concentrations, orientations and projected lengths of nylon fibres in turbulent duct flow were experimentally measured for fibre lengths of 1mm, 2mm, and 3mm. The concentration of fibre centres was found to be nearly zero at the duct wall and to increase linearly until it reached the average channel concentration at approximately $L/3$ away from the wall. Beyond this point the concentration is relatively constant. Thus the concentration gradient can be expressed as:

$$\frac{C}{C_{\text{av}}} \approx \begin{cases} my/L & \text{if } y/L < 1/m \\ 1 & \text{if } y/L \geq 1/m \end{cases} \tag{6.120}$$

where m is approximately 3.22.

The orientation near the wall was found to be predominantly positive at a distance $L/3$ away from the wall, for all three fibre lengths. The projected length of the fibres was shown to be approximately $L/2$ at $y \approx 0$, becoming $0.8L$ at $y \approx L/3$ from the wall. The normalized concentration, orientation, and projected length profiles were similar for all three fibre lengths when expressed in terms of a non-dimensional distance from the wall (distance divided by fibre length).

The diminished fibre concentration near the wall can be explained by considering a

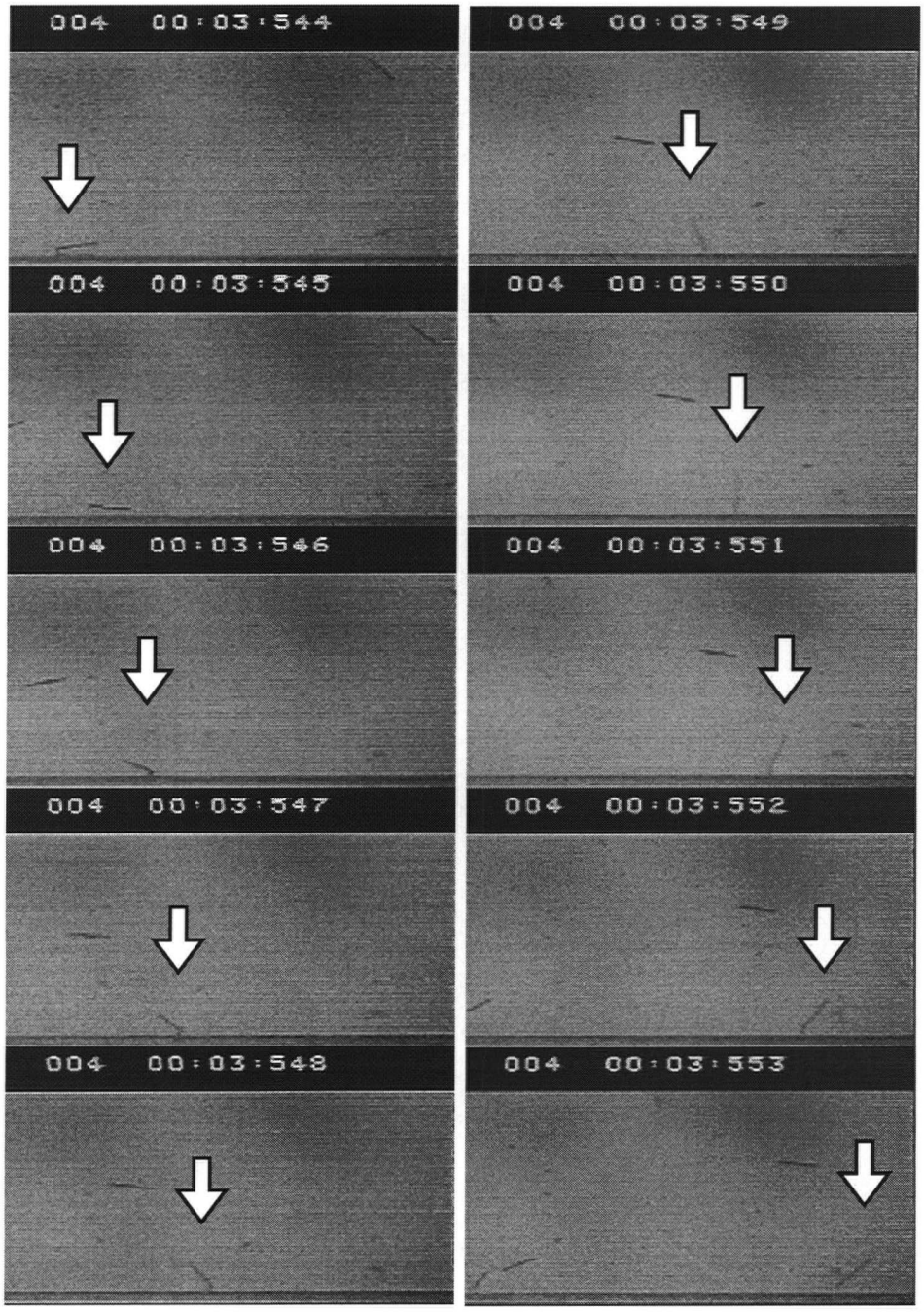

Figure 6.37: High speed video images of a single fibre rotating near the wall. Each frame is time indexed in milliseconds, starting at 544 ms.

single fibre rotating in the velocity gradient near the duct wall and impacting with it during rotation. The impact and rotation transports the fibre centre away from the wall. In this zone the fibre rotates more slowly, because the velocity gradient is less. As a result, the fibre assumes a preferred positive orientation near the wall.

6.6 Nomenclature

Table 6.6: The following nomenclature was used in this section.

C	Local fibre centre concentration profile.
C_{av}	Average fibre concentration in channel.
H	Exit layer height.
κ	Von Kármán constant.
l	Position along the fibre's major axis.
L	Fibre Length.
L_p	Projected fibre length.
N	Crowding factor.
m	Fitted constant in empirical fibre centre concentration equation.
θ	Angle of the major axis of the fibre with respect to the x axis.
U, V	x, y components of fluid velocity.
v^*	Wall-friction velocity (see Chapter 7).
y	Distance (of fibre centre) above channel wall.
x, y	Cartesian coordinates.

Chapter 7

PASSAGE RATIO: COMPARISON WITH EXPERIMENT

7.1 Introduction

Separation at a single aperture can be quantified by a passage ratio. Gooding and Kerekes [43] showed how passage ratio is related to the performance of an entire screen. To understand the factors affecting fibre passage through a single aperture, several investigators have measured it experimentally.

Kumar [44] made the most extensive investigation. He experimentally determined the effect of fibre length, slot width, as well as, channel and slot fluid velocities on passage ratio, and correlated his findings to a dimensionless penetration number, P_e, where $P_e = \frac{V_s W}{V_u L}$, (see Equation 3.12). Kumar derived this penetration number by considering two mechanisms. First, he showed that it represented the fibre length fraction that could penetrate into the slot if the fibre travelled a distance W (the slot width) over the face of the slot at a velocity V_u, (the channel velocity) and simultaneously travelled into the slot by the slot velocity, V_s. By a simple momentum balance, he also reasoned that the same parameter would determine penetration due to turning from forces acting on a fibre stapled on the downstream aperture edge. Because the penetration number was theoretically related to both turning and rotation, it was impossible to determine the relative contribution of each.

Gooding [7] also measured passage ratio as a function of fibre length and slot velocity, and studied fibre motion during passage using high speed cinematography. From

this investigation, he showed that the concentration of long fibres in the exit layer was approximately 1/3 the concentration of the bulk flow. He also showed that fibres pass through the aperture from only certain initial positions and heights. However, because only one fibre length was used, and because too few fibres were examined to accurately estimate fibre concentration, the contribution of each mechanism was again difficult to determine.

Tangsaghasaksri [35] measured passage ratios for much higher fibre length to slot width ratios (L/W). He correlated his findings to a semi-empirical model that considered a simple fibre trajectory and moment balance on the slot edge.

From the simple analysis presented in Chapter 3 (Equation 3.11), we showed that passage ratio is dependent on two functions: the probability of passage function and the fibre concentration profile. In Chapter 5 we made theoretical estimates of the probability of passage function and found that the primary factor affecting passage was the height of the fibre centre, y, with respect to the height of the exit layer, H. Other factors, such as fibre length and orientation, are secondary. In Chapter 6 the concentration profile near the wall was experimentally measured. The concentration of fibre centres was found to be nearly zero near the channel wall, to have a nearly linear gradient near the wall, reaching the average channel concentration at approximately $L/3$ above the wall, and to be constant beyond this point.

In this chapter, we compare passage ratios predicted from our analysis to the experimentally measured passage ratios of Gooding [7], Kumar [44] and Tangsaghasaksri [35]. From this comparison, we estimate the contribution of the wall effect on passage ratio.

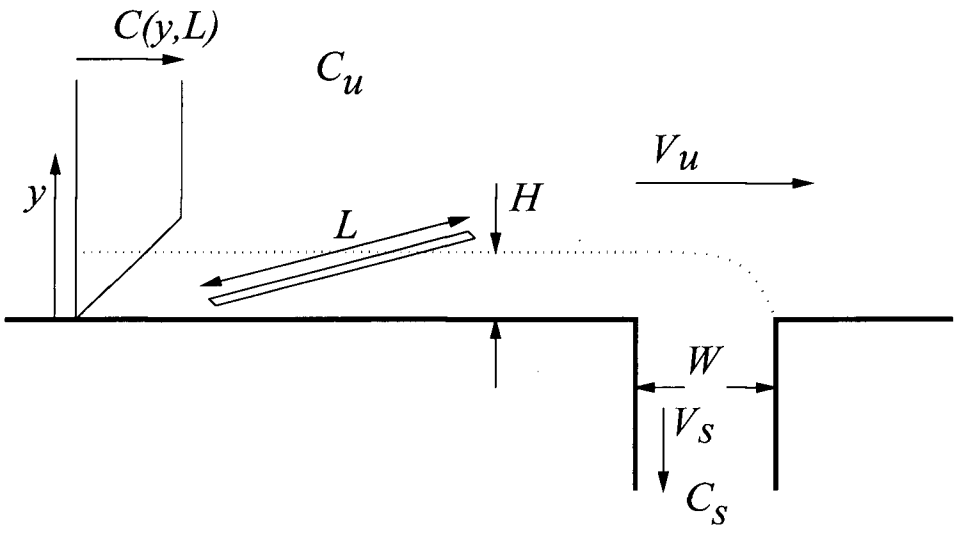

Figure 7.38: Schematic diagram of the fibre concentration profile, channel, exit layer and slot.

7.2 Analysis

From the experimentally measured fibre concentration profile and the first order approximation for the probability of passage function, we calculate passage ratios and compare them with experimentally measured passage ratios (see figure 7.38). The Passage ratio is calculated using Equation 3.11, which was presented in Chapter 3 and is expressed again below as

$$P = \frac{1}{P_e}\int_0^\infty \frac{v(y)}{V_u}\frac{C(y)}{C_{\text{av}}}p(y)\frac{dy}{L} \tag{7.121}$$

Thus, to calculate passage ratio, we require:

- $v(y)$, the fluid velocity profile near the wall, assuming that the particle velocity and fluid velocity are the same.
- $C(y)$, the concentration profile of fibres of length, L.
- $p(y)$, the probability of fibre passage function.

In Chapter 5 (Equation 5.115), we showed that the probability of passage function is, as a first order approximation, given by

$$p(y) = \begin{cases} 1 & \text{if } y/H < 1 \\ 0 & \text{if } y/H \geq 1 \end{cases} \tag{7.122}$$

In Chapter 6 (Equation 6.116) we experimentally showed that the fibre concentration profile is given by

$$\frac{C(y/L)}{C_{\text{av}}} \approx \begin{cases} my/L & \text{if } y/L < 1/m \\ 1 & \text{if } y/L \geq 1/m \end{cases} \tag{7.123}$$

where m is approximately 3.22. The velocity distribution near the wall, assumed to be a log-law velocity distribution, is given by

$$v(y) = \frac{v^*}{k} \ln\left(y\frac{v^*}{\nu}\right) + Bv^* \tag{7.124}$$

where ν is the kinematic viscosity of water, $k = 0.4$ is the Von Kármán constant, and $B = 5.5$, assuming smooth walls. The value of v^* is calculated from the following expression:

$$v^* = \left(\frac{\tau_w}{\rho}\right)^{1/2} \tag{7.125}$$

where ρ is the density of water. The shear stress near the wall, τ_w, is calculated as

$$\tau_w = \frac{C_f \rho V_u^2}{2} \tag{7.126}$$

From pipe theory, the coefficient of friction is then approximated as

$$C_f = 0.0791 {R_e}^{-1/4} \tag{7.127}$$

and the Reynolds number for the duct flow is

$$R_e = \frac{V_u D_h}{\nu} \tag{7.128}$$

where D_h is the channel hydraulic diameter. The log-law velocity profile is in agreement with the experimental fluid velocity measured by Gooding [7] for this duct geometry.

With the velocity profile near the wall expressed in terms of the mean channel velocity, a mass balance around the slot yields the following equation for the exit layer height,

$$\int_0^H v(y)dy = WV_s \tag{7.129}$$

substituting Equation 7.124 into the above and integrating results in the following:

$$Hv^* \frac{\ln \frac{Hv^*}{\nu} + Bk - 1}{k} = WV_s \tag{7.130}$$

Although this equation cannot be solved analytically for the exit layer height, H, it is readily solved numerically.

Substituting all of the above into a single expression for passage ratio yields

$$P = \frac{1}{P_e} \int_0^{H/L} \frac{\left(\frac{v^*}{k} \ln\left(y\frac{v^*}{\nu}\right) + Bv^*\right)}{V_u} \frac{C(y/L)}{C_{\text{av}}} dy/L \tag{7.131}$$

The resulting equation for passage ratio may be integrated numerically and results compared with experimental values of passage ratio.

7.3 Comparison with Data in the Literature

Predictions of passage ratio from Equation 7.131 are compared to the experimental values of passage ratio reported by Gooding [7], Kumar [44] and Tangsaghasaksri [35].

7.3.1 Comparison with Kumar (1991)

The predictions of Equation 7.131 are compared with the experimental passage ratios measured by Kumar [44] in Figure 7.39 and 7.40. Figure 7.39 shows that for small fibre length, to slot width, ratios ($L/W = 1$) the observed passage ratios are in good agreement

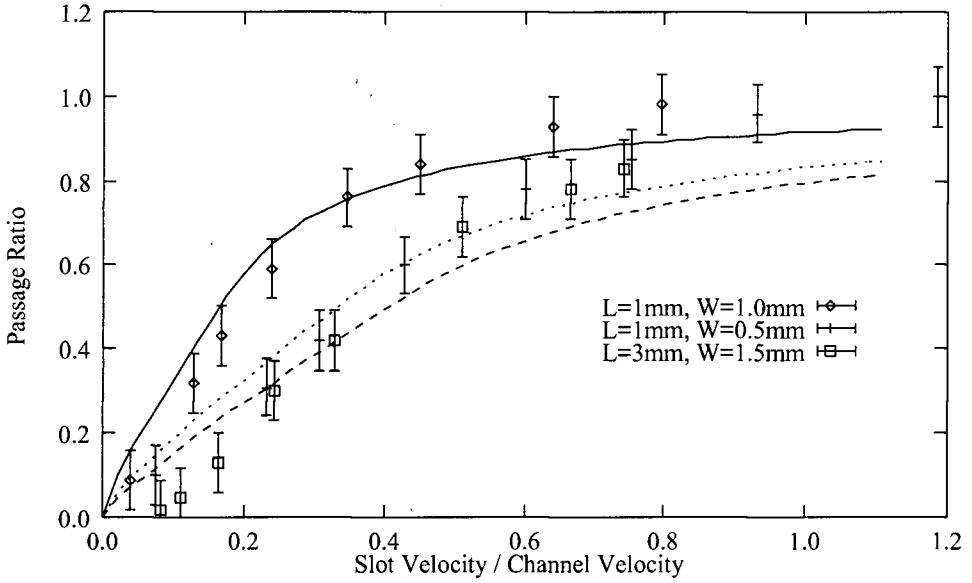

Figure 7.39: The calculated and experimentally determined passage ratios for fibres with a L/W ratio of 1 (L=1mm, W=1mm: Solid Line, $\diamond$) and 2 (L=1mm, W=0.5mm: Dotted Line, $+$, and L=3mm, W=1.5mm: Dashed Line, $\square$).

with the predicted passage ratios. This agreement between calculated and experimental passage ratios suggests that short fibre passage is only dependent on the height of the fibre away from the wall upstream of the aperture. It also shows that for fibres approximately the same length as the slot width, the probability of passage function is well described by Equation 7.122. For fibre lengths twice the slot width ($L/W = 2$), the predicted passage ratio is still in good agreement with the experimental passage ratios. However, at low slot velocities ($V_s/V_u < 0.3$) the experimental passage is slightly less than the predicted passage ratio. At high slot velocities ($V_s/V_u > 0.7$) the experimental passage ratio is slightly higher than the predicted passage ratio.

Figure 7.40 compares the predicted passage ratios with Kumar's experimentally determined passage ratio for $L/W = 3$ and 6. This figure shows that the theoretical predictions straddle the experimental data: for small V_s/V_u the experimental fibre passage ratio is lower than the calculated passage ratio, but as V_s/V_u, increases the passage

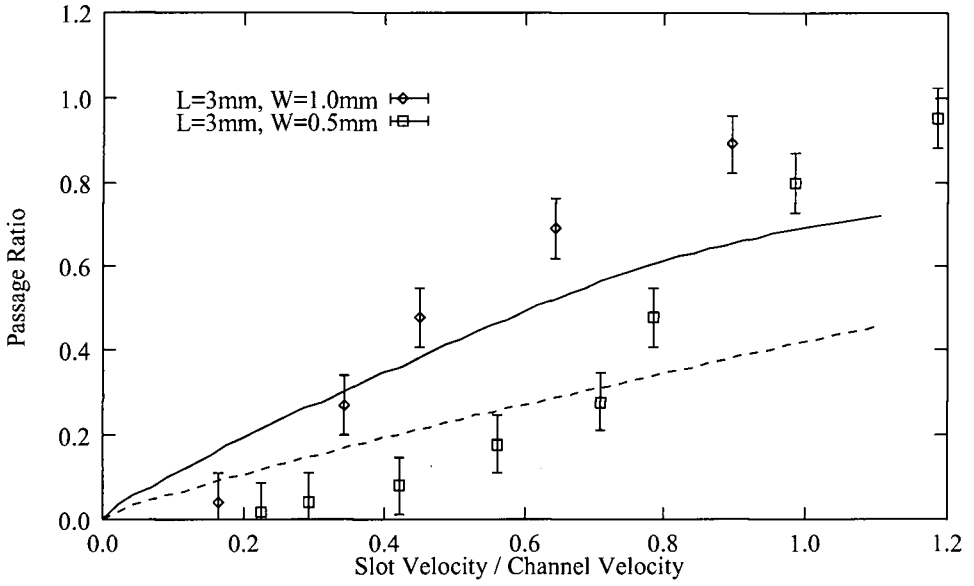

Figure 7.40: The calculated and experimentally determined passage ratios for fibres with a L/W ratio of 3 (L=3mm, W=1mm: Solid Line, $\diamond$) and 6 (L=3mm, W=0.5mm: Dashed Line, $\square$).

ratio becomes higher than predicted by the wall effect alone. Kumar postulated that this "S" shaped curve, which occurred for fibres with $L/W > 2$, is due to fibre stapling from contact with the upstream wall of the slot. At high V_s/V_u, the hydrodynamic force imposed on such fibres, overcomes the moment from the channel flow and the fibres are pulled into the slot. At this V_s/V_u, there is a sharp increase in passage ratio.

Gooding and Kerekes (1989) observed the trajectories of 3mm fibres passing through a 0.5mm slot at a $V_s/V_u \approx 1.0$ using high speed cinematography. The conditions of the tests correspond to Kumar's data shown in Figure 7.40, for $L/W = 6$. They observed that fibres are pulled from beyond the exit layer at high V_s/V_u but always stapled on the downstream edge. They also observed that at high V_s/V_u the stapled fibres built up on the slot edge until they reached a plateau, after which fibres are intermittently pulled into the slot at the same rate as they accumulate.

When the slot entry was "contoured" so that fibres did not staple on the downstream

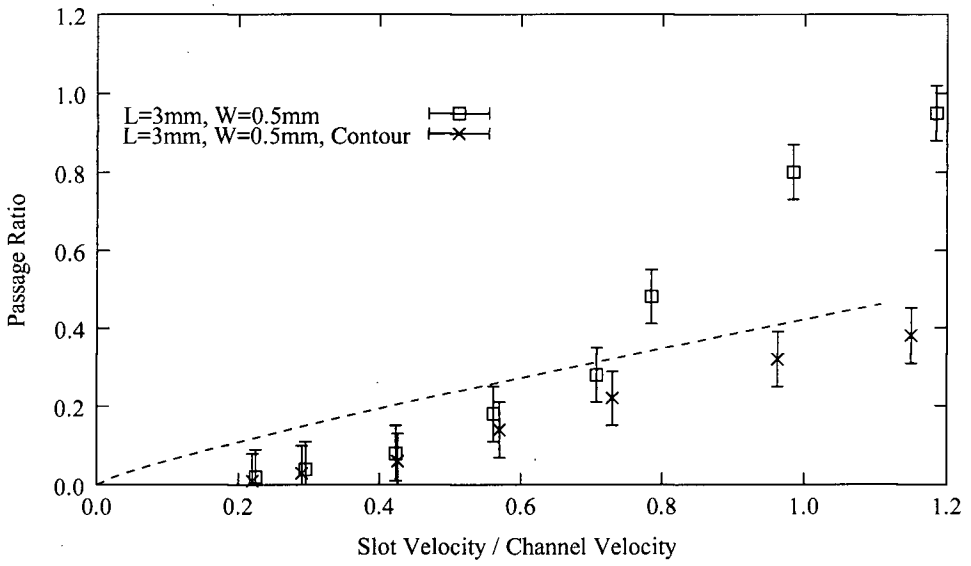

Figure 7.41: The calculated and experimentally determined passage ratios for stiff fibres with a L/W ratio of 6, passing through a contoured (*) and uncontoured (□) aperture.

edge of the slot, the passage ratio no longer increased beyond the predicted passage ratio. Figure 7.41 compares the experimentally determined passage ratios for fibres of $L/W = 6$ passing through a contoured and uncontoured slot [44] with the passage ratio predicted from the wall effect. The experimentally determined fibre passage ratio through the contoured aperture increased with slot velocity at approximately the same rate as that predicted by the wall effect. This further supports the hypothesis that fibre passage is enhanced by conditions that produce stapling on the downstream edge of the slot.

7.3.2 Comparison with Gooding (1986)

Using the same apparatus as Kumar, Gooding [7] also measured the passage ratio of fibres passing through a slot aperture. The experiments differed from Kumar's in that the dilute fibre slurry contained a distribution of fibre lengths and the passage ratios were determined using automated fibre analysis (Kajaani FS-100). Three fibre types were used: nylon fibres, kraft pulp fibres and mechanical pulp (CTMP) fibres, representing a range

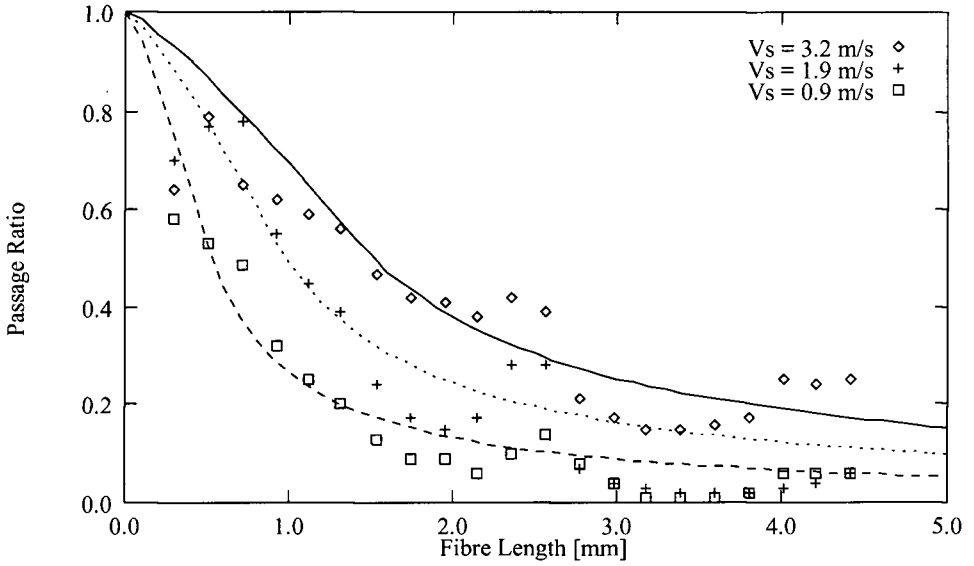

Figure 7.42: The calculated and experimentally determined passage ratios for a distribution of stiff nylon fibres as determined by Gooding (1986), for three slot velocities. The channel velocity is 6.4m/s and the slot width is 0.5mm. (Solid Line V_s=3.2m/s, Dotted Line V_s=1.9m/s, Dashed Line V_s=0.9m/s)

of fibre stiffnesses. The slot width used in these experiments was 0.5mm and the average channel velocity was 6.4m/s

Figure 7.42 shows measured and predicted passage ratios as a function of fibre length for three slot velocities.

The predicted and measured passage ratios show good agreement for short fibre lengths ($L/W < 2$). The lowest slot velocity shows less passage than predicted at high fibre lengths, which is similar to the comparison with Kumar. However, this graph is somewhat noisy, probably due to the limitations of the fibre analyzer which is optimized for natural cellulose fibres.

This experiment was repeated for natural cellulose fibres. Figure 7.43 shows the measured and predicted passage ratios as functions of fibre length for kraft pulp fibres. The calculated passage ratio gives good agreement over a large range of fibre lengths, at all three slot velocities. The measured passage ratio at the lowest slot velocity ($V_s = 0.9m/s$)

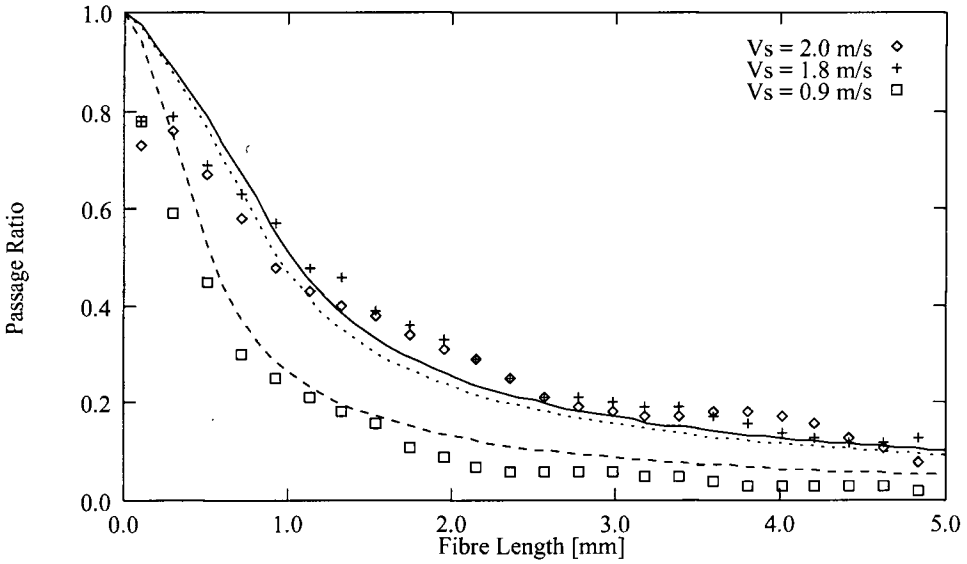

Figure 7.43: The calculated and experimentally determined passage ratios for a distribution of kraft fibres as determined by Gooding (1986), for three slot velocities. The channel velocity is 6.4m/s and the slot width is 0.5mm. (Solid Line V_s=2.0m/s, Dotted Line V_s=1.9m/s, Dashed Line V_s=0.9m/s)

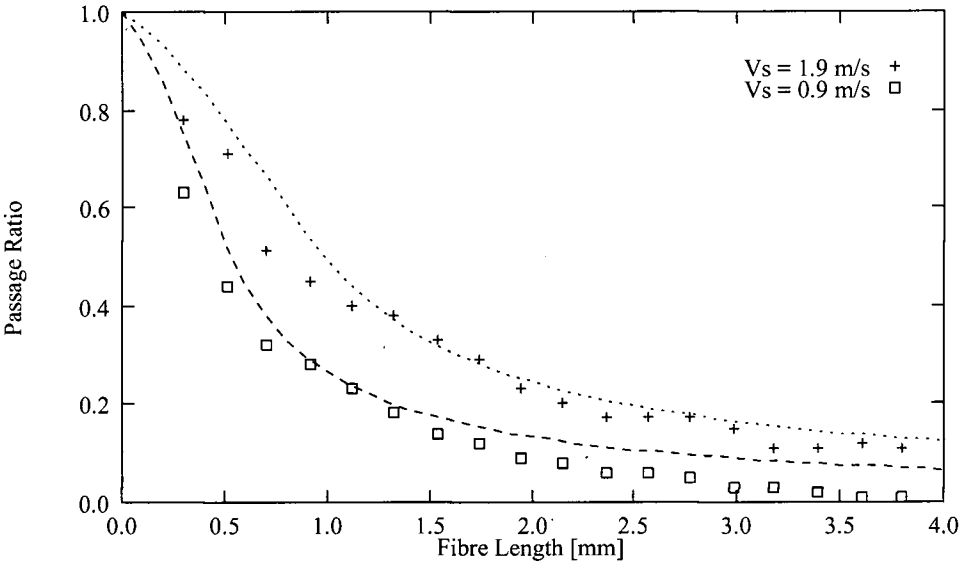

Figure 7.44: The calculated and experimentally determined passage ratios for a distribution of CTMP fibres as determined by Gooding (1986), for three slot velocities. The channel velocity is 6.4m/s and the slot width is 0.5mm. (Dotted Line V_s=1.9m/s, Dashed Line V_s=0.9m/s)

is again lower than predicted; however, there is better agreement than with nylon fibres. It is hypothesized that flexible kraft fibres are able follow the fluid streamlines better than stiff nylon fibres and this results in a diminished turning effect and better agreement with predictions from the wall effect alone.

Figure 7.44 shows a similar plot of calculated and experimentally measured passage ratios for CTMP fibres. Again, there is good agreement between the predicted and measured passage ratio for short ($L/W < 2$) fibres. For low slot velocities ($V_S = 0.9$), measured passage is lower than predicted and the difference is greater than for the kraft fibres. This is due to the increase in fibre stiffness for CTMP fibres.

All three plots show good agreement for short fibres ($L/W < 2$). At low slot velocities, the measured long fibre ($L/W > 2$) passage ratios are slightly less than the predicted values from the wall effect alone. The magnitude of the differences may be weakly dependent on fibre flexibility.

7.3.3 Comparison with Tangsaghasaksri (1994)

Recently, passage ratios for synthetic fibres on a single slot screen system, under conditions similar to that used by Gooding [7] and Kumar [44], have been experimentally measured using very narrow apertures (0.2mm) [35, 36]. Tangsaghasaksri used 1mm and 3mm fibres with two different flexibilities: The stiffness (elastic modulus times moment of inertia) of the stiff fibres was approximately. $2.0 \times 10^{-10}\text{Nm}^2$ and the stiffness of the flexible fibres was approximately $0.8 \times 10^{-8}\text{Nm}^2$. The flexibility of the fibres used by Kumar and Gooding was approximately $3 \times 10^{-10}\text{Nm}^2$. The corresponding L/W ratios were 5 and 15, which are higher than fibres used by Gooding or Kumar.

Figure 7.45 compares the measured passage ratios with the predicted passage ratios due to the wall effect alone. The poor agreement between the predictions and the measurements of Tangsaghasaksri may be due in part to experimental differences that are

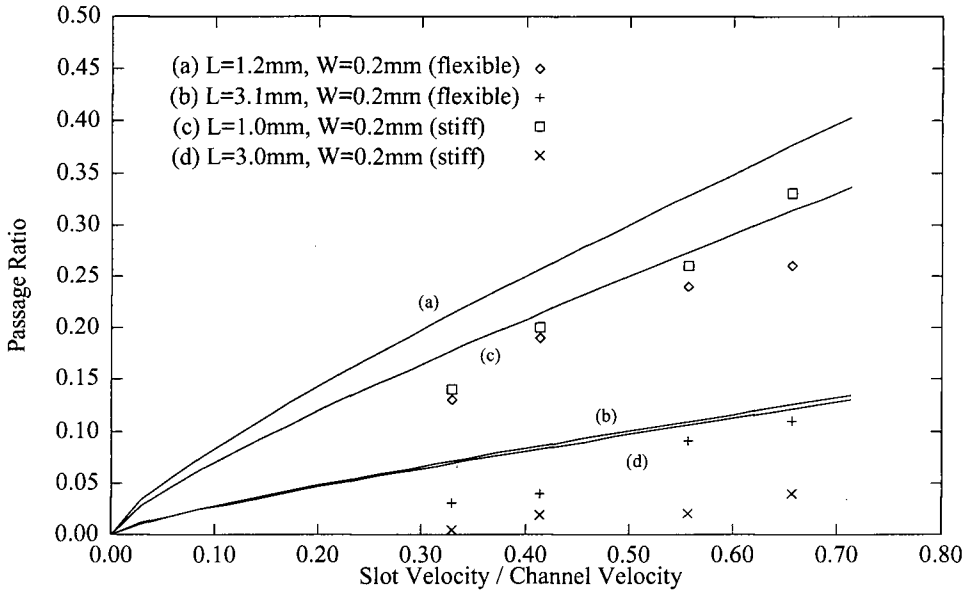

Figure 7.45: The calculated and experimentally determined passage ratios for synthetic fibres with a high L/W ratio and two different flexibilities. Tangsaghasaksri (1994)

not apparent in the published work, and to assumptions such as his fibre concentration profile being the same in this study.

For fibres with $L/W \approx 5$ and 6, Equation 7.131 overpredicts the observed passage ratios. This corresponds with the previous comparisons with experiment. The difference between the experimental passage ratios of the flexible and stiff fibres is the same magnitude as that predicted by the small difference in fibre length.

For longer fibres ($L/W \approx 15$), the calculated passage ratio is still overpredicted relative to the measured fibre passage, but the results for the flexible fibres are in better agreement than those for the stiff fibres.

7.4 Summary

We calculated passage ratios from the measured concentration profile, assuming that the probability of passage depends only on the position of the fibre centre relative to

the height of the exit layer. The predicted passage ratios were then compared with experimental values in the literature.

In the case of stiff fibres, for $L/W \leq 2$, the concentration profile is responsible for most of the observed fibre separation, over the entire slot velocity range. For longer fibres ($L/W > 2$), the passage ratio due to the concentration profile remains a large contribution to the measured passage ratio. However, at low V_s/V_u there is less passage than predicted by the concentration profile, which is attributed to the turning effect. For high V_s/V_u, the experimentally observed passage ratio is significantly greater than the predicted passage ratio. This increase is attributed to increased lodging of stiff fibres in the slot due to contact with the upstream wall and subsequently passing into the slot.

7.5 Nomenclature

Table 7.7: The following nomenclature was used in this section.

B	Empirical constant in log-law of the wall velocity profile.
$C(y)$	Fibre concentration profile in fluid upstream of the aperture.
C_f	Coefficient of pipe friction.
D_h	Hydraulic diameter.
H	Exit layer height.
κ	Von Kármán constant.
L	Fibre length.
m	Fitted constant in empirical fibre centre concentration equation.
ν	kinematic viscosity.
P	Passage ratio, $P = \frac{C_s}{C_u}$.
$p(y)$	Probability of passage function.
P_e	Penetration number, $P_e = \frac{V_s W}{V_u L}$.
R_e	Reynolds number of channel.
ρ	Density of water.
τ_w	Wall shear stress.
V_s	Average slot fluid velocity.
V_u	Average upstream channel fluid velocity.
$v(y)$	Particle velocity profile upstream of the aperture.
v^*	Wall-friction velocity.
W	Slot width.
y	Distance from the channel wall; Cartesian co-ordinate.

Chapter 8

Summary and Conclusions

8.1 General

This thesis has examined the factors affecting the passage of fibres through narrow apertures under conditions similar to pulp pressure screening. This was accomplished by developing a theoretical model of fibre passage and verifying the predictions of this model experimentally. The theoretical model is based on earlier observations of a "wall effect" and a "turning effect". These factors are represented in the model as a fibre concentration profile upstream of the aperture, and as the probability of a fibre from a given position entering the aperture.

For a given initial position and orientation of a fibre upstream of the wall, the probability of passage is modeled by theoretically determining the trajectories of individual fibres in the entry flow of the aperture and during impacts with the aperture wall. The influence of turbulence on fibre trajectories was examined separately, and shown to be insignificant in this case.

Using the theoretically calculated probabilities of passage and the experimentally measured fibre concentration profile upstream of the aperture, passage ratios of fibres of different sizes were predicted. The predictions were compared to experimental measurements of passage ratio. The theoretical model was found to give good predictions of average passage ratio.

8.2 Specific Findings

In the course of deriving the model and carrying out the experimental work, a number of individual problems were addressed and findings attained. These are summarized below.

8.2.1 Fibre Motion in Turbulent Flow

In a general analysis extending previous work on point particles to fibres (points in space to line elements), simple expressions were derived to predict the mean and the turbulent motion of fibres in a turbulent flow. The equations of mean motion were derived assuming an inertialess, rigid fibre, and a Stokesian drag force. The turbulent equations of motion were given as functions of the Lagrangian velocity correlation assuming a homogeneous, isotropic turbulence, with identical longitudinal and perpendicular velocity correlations. This analysis showed that:

1. The mean fibre translation is given by the average fluid velocity over the length of the fibre (Equation 4.19).

2. The mean rotation of the fibre is given as the first moment of the fluid velocity over the length of the fibre (Equation 4.20).

3. The translational and rotational velocity fluctuations of a fibre and its resulting dispersion become increasingly damped as fibre length increases, extending through the turbulence.

8.2.2 Theoretical Predictions of Fibre Passage

The mean equations of motion form the basis of a numerical model of fibre trajectory during passage, which was used to theoretically estimate the probability of passage function. The equations of motion, derived in Chapter 4, were extended to include wall reaction

forces experienced during impact with the aperture. We assumed planar fibre motion, drag and lift components to the Stokes force and a friction coefficient. Initial results of the simulation suggest the separation observed by Kumar [44] (Figure 2.4) cannot be accounted for by fibre trajectories alone. The simulations show that:

1. As a first order approximation, fibres whose centres originate in the exit layer pass through the slot; fibres whose centres originate outside the exit layer do not.

2. Long fibres can be pulled from beyond the exit layer and into the slot if their initial orientation is slightly negative, *i.e.*, the fibre's leading tip points towards the aperture entry.

3. Long fibres can be rejected from the exit layer if the initial orientation is sufficiently positive.

4. On average, the number of fibres rejected from within the exit layer balance the number of fibres accepted from beyond the exit layer.

8.2.3 Experimental Measurement of Fibre Concentration

In the experimental work of this study, it was shown for stiff fibres that:

1. The fibre concentration is zero at the wall, increases linearly with distance from the wall and becoming constant at approximately $L/3$ away from the wall (Equation 6.116).

2. Fibres have a preferred, slightly positive orientation near the wall.

3. The mean projected length of the fibres is approximately 0.5 L at the wall increasing to approximately 0.8L at L/3.

4. Both the concentration profile and positive orientation are explained assuming fibre rotation near the wall transports fibre centres away from the wall.

8.2.4 Passage Ratio: Prediction and Measurement

The theoretically predicted passage ratios were compared with experimental values. The comparison showed that:

- For $L/W \leq 2$, stiff and flexible fibres behave similarly. In both cases passage ratio is well described by the model.
- For longer fibres ($L/W > 2$), the passage ratio due to the concentration profile remained a large contribution to the measured passage ratio. However, at low V_s/V_u there is less passage than predicted by the concentration profile. For high V_s/V_u the experimentally observed passage ratio is greater than the predicted passage ratio. These differences are due attributed to aspects of real fibres not included in this analysis, such as, flexible fibre bending and stapling.

8.3 Conclusion

From these findings, the major conclusion of the thesis is that, at the conditions tested, fibre passage is primarily due to the upstream fibre concentration profile. Conversely, trajectory effects are secondary factors affecting passage.

Bibliography

[1] J.L. Brewer and J.A. Bolton. Fiber fractionation of high-yield kraft pulp. *Tappi J.*, 57(6):121–122, 1974.

[2] R.J. Dobbins. High kappa number grocery bag production by means of stock fractionation. *Tappi J.*, 61(10):90–92, 1978.

[3] H. Selder. Fractionation - The technology of the future. *Paper Technology*, pages 13–16, March 1992.

[4] M. Scott. Fractionation of secondary fibre - a review. *Progress in Paper Recycling*, pages 50–59, 1994.

[5] R. Gooding and R. Kerekes. Derivation of performance equations for solid-solid screens. *The Canadian Journal of Chemical Engineering*, 67:801–805, October 1989.

[6] R. Gooding and R. Kerekes. Consistency changes caused by pulp screening. *Tappi Journal*, pages 109–118, November 1992.

[7] R. Gooding. The passage of fibres through slots in pulp screening. Master's thesis, University of British Columbia, 1986.

[8] G.L. Nelson. The screening quotient: a better index of screen performance. *Tappi J.*, 64(5):133–135, 1981.

[9] T. Bliss. Stock preparation short course. TAPPI.

[10] A.W. Hooper. *Pulp and Paper Manufacture*, volume 5: Alkaline Pulping, chapter The screening of chemical pulp, page 318. The Joint Textbook Committee of the Paper Industry, 3 edition, 1989.

[11] A.W. Hooper. *Pulp and Paper Manufacture*, volume 2: Mechanical Pulping, chapter The screening of chemical pulp, page 181. The Joint Textbook Committee of the Paper Industry, 3 edition, 1983.

[12] W.H Siewart, H. Selder, and P.J. Flynn. Customizing fractionation performance. In *Pulping Conference, Preprints: 721-727.* Tappi, 1989.

[13] Ora and Saarinen. Development of a fractionating screening method for SC groundwood. *Papier ja Puu- paper and timber*, 75(5), 1993.

[14] Repo K. and Sunholm J. The effect of rotor speed on the separation of coarse fibers in pressure screens. In *Int. Mech. Pulping Conf., Ottawa*, pages 271–275, 1995.

[15] D.D. Goosney. Evaluation of Ahlstrom's profiled slotted screen plate. In *79th Ann. mtg. CPPA Tech Sect. Preprints: A1-A6.* CPPA, 1993.

[16] A.W. Hooper. High effeciency screening with slotted plates. In *Pulping Conference pp353-361.* TAPPI, 1987.

[17] A.W. Hooper. A comparison of slots and holes in the screening of mechanical pulp. *Pulp and Paper Canada*, 88(10), 1987.

[18] A.W. Hooper. Screening of mechanical printing papers. *Appita*, 42(5), 1989.

[19] S.F. Ali. Fibre fractionation in pulp processing. In *73rd Ann. mtg. CPPA Tech Sect. Preprints: A1-A6.* CPPA, 1987.

[20] A. Jepson. New wave screen basket upgrades existing systems. In *Preprints of the 71th Ann. CPPA Tech. Sect.*, pages B109–115, 1985.

[21] Coen B. Cleaning/screening: better system engineering is key to cleaner pulp. *Pulp and Paper*, pages 94–101, June 1983.

[22] Tantalo L. and Jackson M. The effects of screening system configuration on end use properties. In *TAPPI Proc. Pulping Conference*, pages 229–235, 1989.

[23] L. Paavilainen. The possibility of fractionating softwood sulfate pulp according to cell wall thickness. *Appita*, 45(5), 1992.

[24] G. Gavelin and J. Backman. Fractionation with hydrocyclones. *Tappi pulping conf.*, pages 753–774, 1991.

[25] T. Rehmat and R. Branion. Fibre fractionation in hydrocyclones. In *81st Ann. mtg. CPPA Tech Sect.*, 1995.

[26] J. Kubat and B. Steenberg. Screening at low particle concentrations. *Svensk Papperstidning*, 58(9):319–324, 1955.

[27] J. Kubat. Screening processes involving particle interactions. *Svensk Papperstidning*, 59(5):175–178, 1956.

[28] J. Kubat. Experimental evidence of the validity of the statistical screening theory. *Svensk Papperstidning*, 59(7):251–256, 1956.

[29] O. Andersson and W. Bartok. Application of feedback to fibre classifiers. *Svensk Papperstid.*, 58(10):367–373, 1955.

[30] A. Tirado. Theory of screening. *Tappi J.*, 41(5):237–245, May 1958.

[31] R. Estridge. The initial retention of fibres by wire grids. *Tappi J.*, 45(4):285–291, 1962.

[32] R.W. Abrams. Retention of fibres in filtration of dilute suspensions. *Tappi J.*, 47(12):773–778, February 1964.

[33] J. Riese, H. Spiegelberg, and K. Ebeling. Mechanism of screening: Dilute suspensions of stiff fibres at normal incidence. *Tappi Journal*, 52(5):895–903, 1969.

[34] H. Nasr-El-Din and C.A. Shook. Particle segregation in slurry flow through vertical tees. *Int. J. Multiphase flow*, 12(3):427–443, 1986.

[35] W. Tangsaghasaksri. *Über die Sortierung von Fasersuspensionen mittels geschlitzter Siebe.* PhD thesis, Darmstad, 1994.

[36] W. Tangsaghasaksri, M. Steuernagel, and L Göttsching. Modelling of fiber passage through slotted screens. *Papier*, 48(10):635–638, 1994.

[37] W. Tangsaghasaksri and L Göttsching. Influence of slot contours on fibre seperation-investigations with the help of a model sorter: part2. *Papier*, 48(5):235–247, 1994.

[38] W. Tangsaghasaksri, M. Steuernagel, and L Göttsching. Effect of contoured slots on fibre passage-investigations by means of a model screen:part 1. *Papier*, 48(5):172–179, 1994.

[39] W. Tangsaghasaksri and L. Göttsching. Analytical assessment of screening of fibre suspension by means of slotted screens. *Papier*, 49(5):213–218, 1995.

[40] C. Yu and R. DeFoe. Fundamental study of screening hydraulics, part 1: Flow patterns at the feed-side surface of screen baskets; mechansim of fibre-mat formation

and remixing. *TAPPI Journal*, 77(8):219–226, 1994.

[41] C. Yu and R. DeFoe. Fundamental study of screening hydraulics, part 2: Fiber orientation in the feed side of a screen basket. *TAPPI Journal*, 77(9):119–124, 1994.

[42] C. Yu, B.R. Crossley, and L. Silveri. Fundamental study of screening hydraulics, part 3: Model for calculating effective open area. *TAPPI Journal*, 77(9):124–131, 1994.

[43] R. Gooding and R. Kerekes. The motion of fibres near a screen slot. *J. Pulp Paper Sci.*, 15(2):59–62, 1989.

[44] A. Kumar. *Passage of fibres through screen apertures.* PhD thesis, University of British Columbia, 1991.

[45] G.B. Jeffery. The motion of ellipsoidal particles immersed in a viscous fluid. *Proc. Royal Soc.*, A102(161), 1922.

[46] H.L. Goldsmith and S.G. Mason. The flow of suspensions through tubes 1. single spheres, rods, and discs. *J. Colloid Sci.*, 17(5):448–476, June 1962.

[47] E. Anczurowski and S.G. Mason. The kinetics of flowing dispersions ii. Equilibrium orientation of rods and discs (theoretical). *Journal of Colloid and Interface Science*, 23:522–533, 1967.

[48] E. Anczurowski and S.G. Mason. The kinetics of flowing dispersions iii. Equilibrium orientation of rods and discs (experimental). *Journal of Colloid and Interface Science*, 23:533–546, 1967.

[49] C.E. Chaffey, M. Takano, and S.G. Mason. Particle motion in sheared suspensions xvi. Orientations of rods and disks in hyperbolic and other flows. *Canadian Journal of Physics*, 43, 1965.

[50] D.L. Stover, D.L. Koch, and C. Cohen. Observations of fibre orientation in simple shear flow of semi-dilute suspension. *Journal of Fluid Mechanics*, 238:277–296, 1992.

[51] S.R. Doshi, J.M. Dealy, and J-M Charrier. Flow induced fibre orientation in an expanding tubing die. *Polymer Engineering and Science*, 26(7):468–478, 1986.

[52] R.C. Givler, M.J. Crochet, and B.R. Pipes. Numerical prediction of fibre orientation in dilute suspensions. *J. Composite Materials*, 209:330–343, 1983.

[53] F.P. Bretherton. The motion of rigid particles in a shear flow at low Reynolds number. *J. Fluid Mech.*, 14:284–290, 1962.

[54] H. Brenner. The Stokes resistance of an arbitrary particle. *Chemical Engineering Science*, 18:1–25, 1963.

[55] H. Brenner. The Stokes resistance of an arbitrary particle-ii, an extension. *Chemical Engineering Science*, 19:599–629, 1964.

[56] H. Brenner. The Stokes resistance of an arbitrary particle-iii shear fields. *Chemical Engineering Science*, 19:631–651, 1964.

[57] H. Brenner. The Stokes resistance of an arbitrary particle-iv arbitrary flow fields. *Chemical Engineering Science*, 19:703–727, 1964.

[58] H. Brenner. The Stokes resistance of an arbitrary particle-v symbolic operator representation of intrinsic resistance. *Chemical Engineering Science*, 21:97–109,

1966.

[59] J.M. Burgers. *Second report on viscosity and plasticity.* North Holland Pub., Amsterdam, 1938.

[60] G.K. Batchelor. Slender body theory for particles of arbitrary cross-section in Stokes flow. *J. Fluid Mech.*, 44:419–440, 1970.

[61] R.G. Cox. The motion of long slender bodies in a viscous fluid. part 1. general theory. *J. Fluid Mech.*, 44(4):791–810, 1970.

[62] R.E. Johnson. An improved slender-body theory for Stokes flow. *J. Fluid Mech.*, 90(2):411–431, 1980.

[63] R.E. Khayat and R.G. Cox. Inertia effects on the motion of long slender bodies. *J. Fluid Mech.*, 209:435–462, 1989.

[64] R. Shanker, J.W. Gillespie Jr., and S.I. Guceri. Rheology of fiber suspensions in nonhomogeneous flow fields: Translation induced stresses. In *Proc. ASME, winter annual meeting, San Francisco.* ASME, 1989.

[65] R. Shanker, J.W. Gillespie Jr., and S.I. Guceri. On the effect of nonhomogeneous flow fields on the orientation distribution and rheology of fibre suspensions. *Polymer Engineering and Science*, 31(3):161–171, 1991.

[66] J.F.T Pittman and N. Kasiri. The motion of rigid rod-like particles suspended in non-homogeneous flow fields. *Int. J. Multiphase Flow*, 18(6):1077–1091, 1992.

[67] C. Zhou, S.J. Chen, and C.D. Douglas. Modeling of fibre orientation and bulk viscosity of short fiber filled polymeric fluids in Poiseuille flows. *J. of Polymer Engineering*, 209(1-2):39–53, 1988.

[68] G.I. Taylor. Diffusion by continuous movements. *Proc. London Math. Soc. Ser. 2*, 196(20):196–212, 1921.

[69] P.G. Saffman. An approximate calculation of the Lagrangian auto-correlation coefficient for stationary homogeneous turbulence. *Appli. sci. Res.*, 11(A):345–255, 1962.

[70] S. Corrsin. Progress report on some turbulent diffusion research. In *Proc. Oxford Symposium Atmospheric Diffusion and Air Pollution 162*, pages 161–164. Academic Press, 1959.

[71] R.J. Kraichnan. The structure of isotropic turbulence at very high Reynolds numbers. *J. Fluid Mechanics*, 5:497–543, 1959.

[72] G.K. Batchelor. *Theory of homogeneous flow.* Cambridge University Press, 1953.

[73] W.H. Snyder and J.L. Lumley. Some measurements of particle velocity autocorrelation functions in turbulent flow. *J. Fluid Mech*, 48:41–71, 1971.

[74] J.O. Hinze. *Turbulence.* McGraw-Hill Inc., 1975.

[75] R. Betchov. Introduction to the Kraichnan theory of turbulence. In S.I. Pai, editor, *Dynamics of Fluids and Plasmas.* Academic Press, New York, 1966.

[76] P.H. Roberts. Analytical theory of turbulent diffusion. *Journal of Fluid Mechanics*, 11(2):257–283, 1961.

[77] R.J. Kraichnan. Diffusion by random fields. *Phys. Fluids*, 13(1):22–31, 1970.

[78] R. Pythian. Dispersion by random velocity fields. *Journal of Fluid Mechanics*, 67:145–153, 1975.

[79] T.S. Lundgren and Y.B Pointin. Turbulent self-diffusion. *The physics of fluids*, 19(3):355–358, 1976.

[80] J.C.H. Fung, Hunt J.C.R., N.A. Malik, and Perkins R.J. Kinematic simulation of homogeneous turbulence by unsteady random Fourier modes. *J. Fluid Mech.*, 236:281–318, 1992.

[81] J.M. MacInnes and F.V. Bracco. Stochastic particle modelling and the tracer-particle limit. *Phys. Fluids A*, 4(12):2809–2824, 1992.

[82] G.S. Patterson and S. Corrsin. Computer experiments on random walks with both Eularian and Lagrangian statistics. In S.I. Pai, A.J. Falller, T.L. Lincoln, D.A. Tidman, G.N. Trytten, and T.D. Wilkerson, editors, *Dynamics of Fluids and Plasmas.* Academic Press, New York, 1966.

[83] M.W. Reeks. On the motion of small particles suspended in an isotropic turbulent fluid. *Journal of Fluid Mechanics*, 83(3):529–546, 1977.

[84] L.M. Pismen and A. Nir. On the motion of suspended particles in stationary homogeneous turbulence. *Journal of Fluid Mechanics*, 84(1):193–206, 1978.

[85] Q. Lu, J.R. Fontaine, and G. Aubertin. Langrangian model for solid particles in turbulent flows. *Int. J. Multiphase Flow*, 19(2):347:367, 1993.

[86] A. Ormancey and J. Martinin. Prediction of particle dispersion in turbulent flows. *PhysicoChemical Hydrodynamics*, 5(3):229–244, 1984.

[87] G.A. Kallio and M.W. Reeks. A numerical simulation of particle deposition in turbulent boundary layers. *Int. J. Multiphase Flow*, 15(3):433–446, 1989.

[88] M. Sommerfeld. Numerical simulation of the particle dispersion in turbulent flow: the importance of particle lift forces and particle/wall collison models. *ASME Fluids Engineering Division (Publication) FED*, 91:11--18, 1990.

[89] M. Sommerfeld. Particle dispersion in turbulent flow: The effect of particle size distribution. *Part. Part. Syst. Charact.*, 7:209–220, 1990.

[90] S. Pedinotti, G. Marriotti, and S. Banerjee. Direct numerical simulation of particle behaviour in the wall region of turbulent flows in horizontal channels. *International Journal of Multiphase Flow*, 18(6):927–941, 1992.

[91] B.Y. Underwood. Random-walk modeling of turbulent impaction to a smooth wall. *Int. J. Multiphase flow*, 19(3):485–500, 1993.

[92] H.-e. Cho, J.V. Iribane, and W.G. Richarg. On the orientation of ice crytals in cumulonimbus cloud. *Journal of Atmospheric science*, 38:111–113, 1981.

[93] H. Kagermann and W.E. Köhler. On the motion of nonspherical particles in a turbulent flow. *Physica*, 116A:178–198, 1984.

[94] E.M. Krushkal and Isaiah Gallily. On the orientation distribution function of non-spherical aerosol particles in a general shear flow–ii. the turbulent case. *Journal of Aerosol Science*, 19(2):197–211, 1988.

[95] H. Sanders Jr. and H. Meyer. Consistency distributions in turbulent tube flow of fiber suspensions. *Tappi J.*, 54(5):722:730, May 1971.

[96] T.Q. Li, R.L. Powell, L. Ödberg, M.J. McCarthy, and K.L. McCarthy. Velocity measurements of fibre suspensions in pipe flow by the nuclear magnetic resonance imaging method. *Tappi Journal*, 77(3):145:149, 1994.

[97] B. Asgharian and C. Yu. Deposition of inhaled fibrous particles in the human lung. *Journal of Aerosol Medicine*, 1:37–50, 1988.

[98] B. Asgharian and C. Yu. Deposition of fibres in the rat lung. *Journal of Aerosol Science*, 30:355–366, 1989.

[99] O. Bernstein and M. Shapiro. Direct determination of the orientation distribution function of cylindrical particles immersed in laminar and turbulent flow. *Journal of Aerosol Science*, 25(1):113–136, 1994.

[100] S.L. Lee and F. Durst. On the motion of particles in turbulent duct flow. *Internaional Journal of Multiphase Flow*, 8(2):125–146, 1982.

[101] J.A. Olson, A.G. Robertson, T.D. Finnigan, and R.H.H Turner. An analyzer for fibre length and shape. *Journal of Pulp and Paper Science*, 21(11):J367–J373, 1995.

[102] M. Martinez. *Forces on fibres in low consistency refining.* PhD thesis, University of British Columbia, 1995.

[103] H.R. Pruppacher, B.P. Le Clair, and A.E. Hamielec. *Numerical Recipes in C: The art of scientific computing (2nd edition).* Cambridge University Press, 1992.

[104] Amtec. *Inca Reference Mannual*, 1995.

[105] R.W. Gooding. *Hydraulic resistance of screen apertures.* PhD thesis, University of British Columbia, 1996.

[106] R.J. Kerekes and C.J. Schell. Characterization of fibre flocculation regimes by a crowding factor. *J. Pulp and Paper Sci.*, 18(1):j32–j38, January 1992.

Appendix A

Jeffery's Equation of Fibre Motion

A.1 Introduction

One of the first investigation of non-spherical particle motion was that of Jeffrey [45]. Jeffrey derived the equation of motion of an arbitrary ellipsoid moving in a Stokes flow, where the undisturbed fluid velocity varies linearly in the neighborhood of particle. Jeffrey calculated moments on the particle and assumed that the forces acting on the particle are in balance, which is the same as assuming the particle is inertialess. Jeffrey solved these equations for the example of simple shear in 2 and 3 dimensions. Here, we give a more general example of applying Jeffery's equations of motion to an arbitrary flow field. The example of general rotation in a plane is derived, and an example of an ellipsoid in extensional flow is discussed. This analysis has often been applied to fibres which are modeled as high aspect ratio ellipsoids.

A.2 Equation of Motion

A.2.1 3-Dimensions

Consider an ellipsoidal particle with dimensions a, b and c being transported by a laminar flow field $\vec{V}$. The spatial derivatives of the flow field surrounding the centre of the particle are assumed to be constant and are given by a constant matrix A':

$$A'_{ij} = \frac{\partial V_i}{\partial x_j} \tag{A.132}$$

Following Jeffrey (1922), we transform A' into a co-ordinate system rotating with the particle, using the rotation matrix R:

$$A = RA'R^T \tag{A.133}$$

where

$$R = \begin{bmatrix} \cos(\theta) & \sin(\theta)\cos(\phi) & \sin(\theta)\sin(\phi) \\ -\sin(\theta)\cos(\psi) & -\sin(\phi)\sin(\psi) + \cos(\theta)\cos(\phi)\cos(\psi) & \cos(\phi)\sin(\psi) + \cos(\theta)\sin(\phi)\cos(\psi) \\ \sin(\theta)\sin(\psi) & -\sin(\theta)\cos(\psi) - \cos(\theta)\cos(\phi)\sin(\psi) & \cos(\phi)\cos(\psi) - \cos(\theta)\sin(\phi)\sin(\psi) \end{bmatrix} \tag{A.134}$$

The Euler angles θ, ϕ and ψ give the orientation of the particles axes with respect to the fixed axes of the laboratory.

The angular velocities, ω_1, ω_2 and ω_3, of the particle's axis, are given by:

$$\omega_1 = (b^2A_{32} - c^2A_{23})/(b^2 + c^2) \tag{A.135}$$

$$\omega_2 = (c^2A_{13} - a^2A_{31})/(c^2 + a^2) \tag{A.136}$$

$$\omega_3 = (a^2A_{23} - b^2A_{32})/(a^2 + b^2) \tag{A.137}$$

where the angular velocities are defined in terms of the Euler angles as:

$$\omega_1 = \dot{\phi}\cos(\theta) + \dot{\psi} \tag{A.138}$$

$$\omega_2 = \dot{\theta}\sin(\psi) - \dot{\phi}\sin(\theta)\cos(\psi) \tag{A.139}$$

$$\omega_3 = \dot{\theta}\cos(\psi) + \dot{\phi}\sin(\theta)\cos(\psi) \tag{A.140}$$

These can be re-written to form an easily solvable (numerically) system of first order coupled initial value differential equations:

$$\begin{bmatrix} \dot{\theta} \\ \dot{\phi} \\ \dot{\psi} \end{bmatrix} = \begin{bmatrix} 0 & \sin(\psi) & \cos(\psi) \\ 0 & -\frac{\cos(\psi)}{\sin(\theta)} & \frac{\sin(\psi)}{\sin(\theta)} \\ 1 & -\frac{\cos(\psi)}{\tan(\theta)} & -\frac{\cos(\psi)}{\tan(\theta)} \end{bmatrix} \begin{bmatrix} (b^2A_{32} - c^2A_{23})/(b^2 + c^2) \\ (c^2A_{13} - a^2A_{31})/(c^2 + a^2) \\ (a^2A_{23} - b^2A_{32})/(a^2 + b^2) \end{bmatrix} \tag{A.141}$$

From this equation it is relatively straight forward to see how an initial value solver such as a Runge-Kutta-Fehlberg algorithm could be implemented.

A.2.2 2-Dimensions

In this section we simplify the general equations given above for the case of 3-dimensional ellipsoid in a 3-dimensional flow to the case of planar rotation of an axisymmetric ellipsoid in two-dimensional flow.

For a planar, two-dimensional flow field, the first angular velocity, ω_1, given above is re-expressed in terms of the angle χ, *i.e.* $\omega_1 = \dot{\chi}$, and we redefine the rotation matrix for planar rotation as:

$$R = \begin{bmatrix} 1 & 0 & 0 \\ 0 & \cos(\chi) & \sin(\chi) \\ 0 & -\sin(\chi) & cos(\chi) \end{bmatrix} \tag{A.142}$$

We now change from the three-dimensional notation to the typical two-dimensional coordinate system, where U and V are the flow velocity components with respect to the x and y axis, respectively, and θ is the angle of the particles long axis with respect to the x axis. The particle has an aspect ratio $c/b = \alpha$ greater than or equal to one. The transformation is given by $\theta = -\chi$, $A'_{22} = \partial V/\partial y$, $A'_{23} = \partial V/\partial x$, $A'_{32} = \partial U/\partial y$ and $A'_{33} = \partial U/\partial x$.

A is then calculated using the rotation matrix, as before ($A = RA'R^T$) to yield

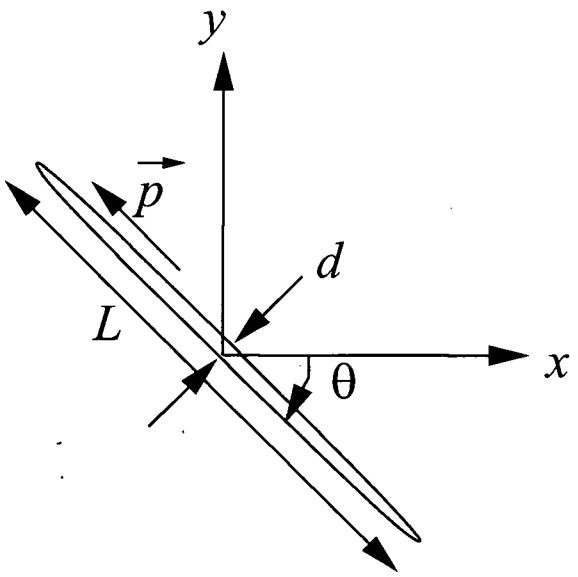

Figure A.46: An ellipsoidal particle in a uniform flow field.

$$\frac{d\theta}{dt} = \frac{\frac{1}{2}(\alpha^2 - 1)\sin(2\theta)(\frac{\partial V}{\partial y} - \frac{\partial U}{\partial x}) + (\sin^2(\theta) + \alpha^2\cos^2(\theta))\frac{\partial V}{\partial x} - (\cos^2(\theta) + \alpha^2\sin^2(\theta))\frac{\partial U}{\partial y}}{\alpha^2 + 1} \tag{A.143}$$

A.3 Analytical example

For the simple case of a 2-dimensional ellipsoidal particle in a simple extensional flow, Equation A.143 can be solved analytically. This serves as a simple example of how these differential equations can be used to predict the particle motion assuming local linearity of the velocity field in the neighborhood of the particle.

Given a 2-dimensional tapering duct (see Figure A.47) we can approximate the flow field from the overall cell geometry and continuity, as

$$U(x) = \frac{U_0}{1 - \frac{x}{L}} \tag{A.144}$$

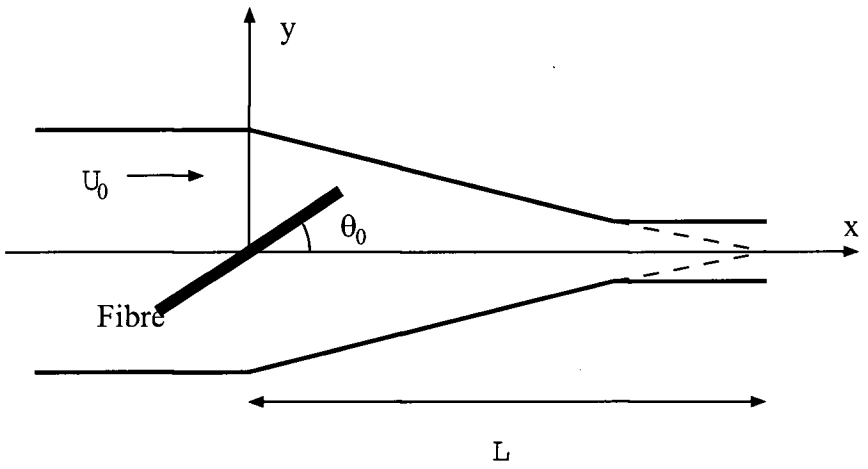

Figure A.47: Coordinates and dimension of the tapered, rectangular duct.

Differentiating with respect to x, and making use of local continuity:

$$\frac{\partial U}{\partial x} = -\frac{\partial V}{\partial y} = \frac{U_0}{L(1-\frac{x}{L})^2} \tag{A.145}$$

By assuming that the centre of the particle moves with the streamlines (in this case the ducts centreline), we integrate $U(x)$ to get the position of the particle as a function of time, t, *i.e.*

$$\frac{x(t)}{L} = 1 - (1 - \frac{2U_0 t}{L})^2 \tag{A.146}$$

We now solve the differential Equation A.143 as a function of time, with $\theta = \theta_0$ at $t = 0$ and convert this into a function of x along the tapered section of the duct.

$$\theta(x) = \arctan(\frac{sin(2\theta_0)}{\cos(2\theta_0)+1}(1 - 2\frac{x}{L} + (\frac{x}{L})^2)^{\frac{\alpha^2-1}{\alpha^2+1}}) \tag{A.147}$$

This equation gives the alignment as a function of position, x, for an arbitrary ellipsoidal particles transported by a laminar fluid through a rectangular, tapering duct. From such information we could predict the alignment in extensional flows.